博士論文
(Doctoral Thesis)

Non-reciprocity of magnon excitations in non-centrosymmetric magnets

(空間反転対称性が破れた磁性体における マグノン励起の非相反性)

井口　雄介
(Yusuke Iguchi)

Department of Basic Science,
University of Tokyo

2017

Acknowledgments

I would like to express my sincerest gratitude to Associate Professor Y. Onose for his continuous research guidance, discussion, and encouragement in the course of this work.

I would like to appreciate to the following people: Dr. Nii (valuable guidance and discussion), Dr. K. Ueno (advice about photolithography and valuable guidance), Dr. C. Hotta (valuable guidance and discussion), Prof. A. Maeda (valuable guidance), Mr. S. Uemura (experimental assistance and discussion), Dr. H. Murakawa (Crystal growth and discussion), Prof. N. Hanasaki (Crystal growth), Prof. Y. Nakamura (advice about microwave measurement and discussion), Dr. H. Toida (advice about microwave measurement and discussion), Prof. S. Murakami (discussion), Dr. S. Hirose (discussion), Dr. K. Penc (discussion), and Dr. K. Matsuba (Supply of liquid Helium and liquid Nitrogen).

I am grateful to Prof. A. Maeda, Prof. Y. Kato, Dr. C. Hotta, and Dr. Y. Takahashi for valuable comments and recommendation on this thesis. I also thank all the members of Onose group (Mr. H. Namikawa, Mr. S. Uemura, Mr. Y. Hirokane, Mr. R. Sasaki, Mr. N. Jiang, Mr. Y. Hamahara, Mr. Y. Ishii, Mr. R. Hattori, Mr. M. Ohtsu, Mr. R. Sakakibara, and Secretary Y. Furuzono), the members of Ueno group (Mr. Y. Sato, Mr. F. Kiyokawa, Mr. S. Hayashi, Mr. S. Nakazawa, and Mr. K. Otomo), and the members of Maeda group (Dr. H. Takahashi, Dr. F. Nabeshima, and Dr. T. Okada) for a lot of great help in diverse ways.

I am supported by the Grant-in-Aid for Research Fellowship for Young Scientists from the Japan Society for the Promotion of Science (No. 16J10076).

Finally, I would like to express my special gratitude to my parents and my wife for support in private life.

Contents

Chapter 1

Introduction

Macroscopic responses observed in solids have always been supported by the symmetry breaking in a state of matter. For example, piezoelectricity and natural optical activity emerge in spatial-inversion symmetry (SIS) broken materials. Time-reversal symmetry (TRS) breaking induces the Hall effect and Faraday effect. It turned out recently that there is a class of systems that require the breaking of both SIS and TRS in materials. The breakthrough is provided by the discovery of the magnetically induced ferroelectrics (multiferroics)[1, 2]. Several developments followed such as magnetoelectric effect[3], a variation of the magnetization induced by the electric field and the electric polarization controlled by the magnetic field. The breaking of both SIS and TRS also affects the dynamics of elementary excitations; the energy and decay rate of wave vector $+k$ become not equivalent to those of $-k$. This phenomenon is non-reciprocity. The non-reciprocity is nontrivial, because the origin is intrinsic interactions appearing only in both SIS and TRS broken materials such as the spin-orbit interaction. This thesis is devoted to the non-reciprocal phenomena relevant to magnon excitation.

The contents of this thesis are as follows:

In Ch. 1, we review previous studies about non-reciprocal phenomena related to magnon excitations.

In Ch. 2, we explain our experimental methods, which include the microwave measurement setup and the crystal growth.

In Ch. 3, we show the magnon non-reciprocal propagation in a chiral ferromagnet $LiFe_5O_8$. Its non-reciprocity originates from the relativistic asymmetric

magnon band.

In Ch. 4, we demonstrate the magnetoelectrical control of non-reciprocal microwave propagation in a ferroelectric helimagnet $Ba_2Mg_2Fe_{12}O_{22}$.

In Ch. 5, we show the magnon modes in a non-centrosymmetric antiferromagnet $Ba_2MnGe_2O_7$, and quantitatively explain the microwave non-reciprocity of one mode by using spin wave theory, Kubo formula, and metal-ligand hybridization mechanism.

In Ch. 6, we summarize this thesis and state prospects for the future.

1.1 Non-reciprocal phenomena

Let us consider the electron band dispersion in order to discuss the relation between the non-reciprocal phenomena and the symmetry breaking. When TRS and SIS are both preserved, the dispersion is symmetric and spin-degenerated as shown in Fig. 1.1(a). In a system with SIS but without TRS the energy splitting depending on the spin state is realized as shown in Fig. 1.1(b). In this case, the energy dispersion is symmetric with respective to k. This corresponds to the Zeeman splitting with a magnetic field. On the other hand, in a SIS-broken but TRS-preserved system, the energy dispersion is horizontally shifted depending on the spin momentum as shown in Fig. 1.1(c). The examples are the Rashba effect[4] and the Dresselhaus effect[5]. Then, in a system without TRS and SIS, the band dispersion is asymmetric regardless of spin state as shown in Fig. 1.1(d). In this case, it is expected that an electron non-reciprocally propagates. In fact, the non-reciprocal electron propagation has been reported in systems without TRS and SIS, such as a chiral material with magnetic field[6], a material with electric and magnetic fields[7], and the edge of topological insulator with magnetic field[8]. Because the relation between the symmetry and energy dispersion is applicable to the other elementary excitations such as photons and magnons, the non-reciprocity is also expected for these excitations in SIS and TRS simultaneously broken systems.

For microwave, the non-reciprocal device was designed by the asymmetric configuration of macroscopic ferromagnetic component, such as the isolator [Fig. 1.2(a) and 1.2(b)]. The non-reciprocity due to material symmetry breaking can be controlled by the external fields. This seems useful for the further functionalization of non-reciprocal microwave device.

In this thesis, we focus on the non-reciprocal phenomena relevant to magnon excitations in microwave region. Specifically, there are two topics; one is non-reciprocal microwave propagation around magnon excitations and the other is non-reciprocal magnon excitations. Following Sections 1.2 and 1.3 describe the overview of electromagnetic wave (including light and X-ray) and magnon non-reciprocities, respectively.

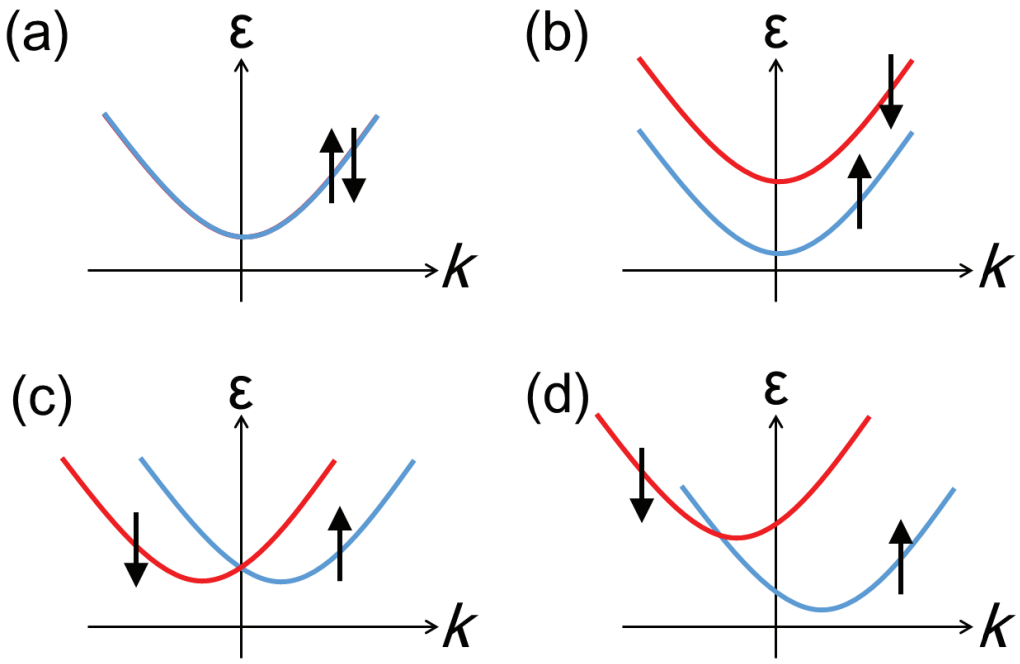

Figure 1.1: **Electron band dispersions with several symmetry breaking.** (a)-(d) Electron band dispersions (a) in a material that has TRS and SIS, (b) in a material with SIS without TRS, (c) in a material with TRS without SIS, and (d) in a material without SIS and TRS.

1.2 Non-reciprocal directional dichroism in multiferroics

Magnetochiral effect and Optical magnetoelectric effect

Electromagnetic wave propagation in symmetry-broken material has been studied for long time, since Arago discovered the optical activity in a solution of quartz[9]. Then Faraday discovered the similar rotational effect due to the magnetic field[10]. Pasteur found that the optical activity microscopically originated from the molecular structure[11]. The Faraday effect and the optical activity can be explained by the off-diagonal elements of dynamical electric susceptibility tensor $\chi^{ee}_{\alpha\beta}$ and the diagonal elements of dynamical magnetoelectric susceptibility tensors $\chi^{em}_{\alpha\alpha}$ and

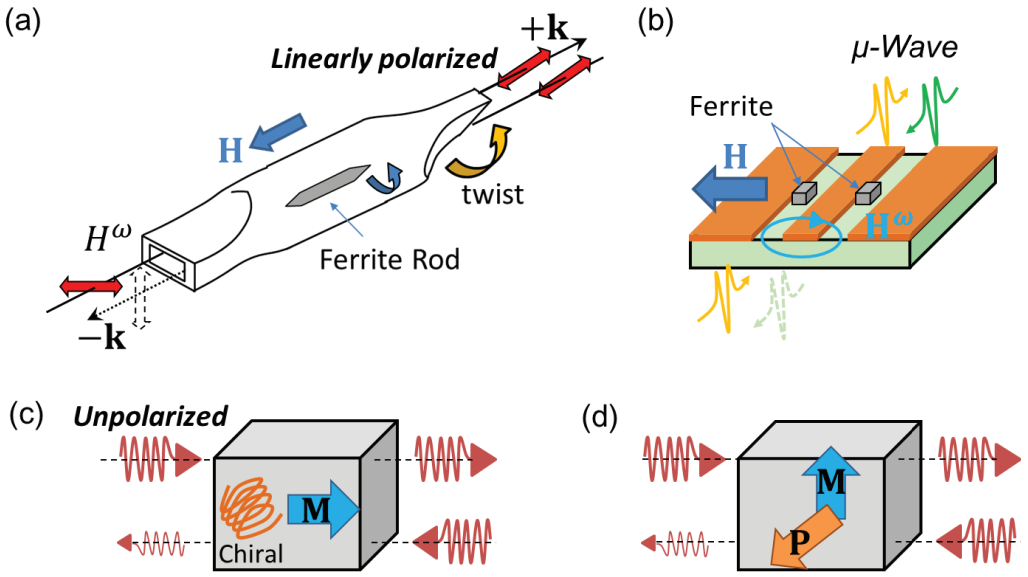

Figure 1.2: **Non-reciprocal phenomena in electromagnetic wave.** (a) The Faraday rotation in linearly polarized light is used for the isolator or circulator with a ferrite rod. (b) Microwave is non-reciprocally absorbed due to the classical non-reciprocal magnon mode on the coplanar waveguide[12]. (c)-(d), (c) The magnetochiral and (d) the optical magnetoelectric effects are non-reciprocal even in the unpolarized light.

$\chi^{me}_{\alpha\alpha}$ (for example, see [13]). Here the dynamical susceptibilities are defined as

$$\begin{aligned} \mathbf{B}^\omega &= \mu_0 \left[\hat{1} + \chi^{mm}\right] \mathbf{H}^\omega + \sqrt{\varepsilon_0 \mu_0}\chi^{me}\mathbf{E}^\omega, \\ \mathbf{D}^\omega &= \varepsilon_0 \left[\bar{1} + \chi^{ee}\right] \mathbf{E}^\omega + \sqrt{\varepsilon_0 \mu_0}\chi^{em}\mathbf{H}^\omega, \end{aligned} \tag{1.1}$$

where χ^{mm} is the dynamical magnetic susceptibility tensor, $\mathbf{B}^\omega$ and $\mathbf{D}^\omega$ are dynamical magnetic induction and dynamical electric induction, $\mathbf{E}^\omega$ and $\mathbf{H}^\omega$ are the electric and magnetic fields of a plane wave at a position $\mathbf{r}$ and time t with an angular frequency ω and a wave vector $\mathbf{k}$, $\mathbf{E}^\omega, \mathbf{H}^\omega \propto \exp(-i\omega t + i\mathbf{k}\cdot\mathbf{r})$, and μ_0 and ε_0 are the magnetic permeability and permittivity in vacuum, respectively. The Faraday effect is the non-reciprocal phenomenon of the linear polarized light, whereas the non-reciprocal phenomena of the unpolarized light was introduced as the higher order effect by Wagnière and Meire[14, 15], and Barron and Vrbancich[16]. They showed that the off-diagonal elements of the dynamical magnetoelectric susceptibility $\chi^{em}_{\alpha\beta}, \chi^{me}_{\beta\alpha}$ provided the non-reciprocal directional dichroism (NDD). For ex-

ample, in magnetoelectric media, which shows the magnetoelectric effect such as multiferroics, the Maxwell's equation are described as a function of the dynamical susceptibilities

$$\mathbf{k} \times \mathbf{E}^{\omega} = \omega \left\{ \mu_0 \left[\hat{1} + \hat{\chi}^{mm}(\omega) \right] \mathbf{H}^{\omega} + \sqrt{\varepsilon_0 \mu_0} \hat{\chi}^{me}(\omega) \mathbf{E}^{\omega} \right\}, \tag{1.2}$$

$$\mathbf{k} \times \mathbf{H}^{\omega} = -\omega \left\{ \varepsilon_0 \left[\hat{1} + \hat{\chi}^{ee}(\omega) \right] \mathbf{E}^{\omega} + \sqrt{\varepsilon_0 \mu_0} \hat{\chi}^{em}(\omega) \mathbf{H}^{\omega} \right\}. \tag{1.3}$$

For example, in a linearly polarized light, $\mathbf{k} \parallel \mathbf{x}$, $\mathbf{H}^{\omega} \parallel \mathbf{y}$ and $\mathbf{E}^{\omega} \parallel \mathbf{z}$, the complex refractive index is expressed as

$$n(k_{\pm}) = \sqrt{\frac{(\chi_{yz}^{me} - \chi_{zy}^{em})^2}{4} + (1 + \chi_{zz}^{ee})(1 + \chi_{yy}^{mm})} \mp \frac{\chi_{yz}^{me} + \chi_{zy}^{em}}{2}, \tag{1.4}$$

where k_+ and k_- are wave vectors parallel and anti-parallel to x-axis, respectively. From the above form of the complex refractive index, the difference of the absorption coefficients $\Delta\alpha$ is depending on the imaginary parts of the off-diagonal terms of the dynamical magnetoelectric susceptibilities.

$$\Delta\alpha = \omega\sqrt{\varepsilon_0\mu_0}\mathrm{Im}\left[n(k_+) - n(k_-)\right] = -\omega\varepsilon_0\mu_0\mathrm{Im}\left[\chi_{xz}^{em} + \chi_{zx}^{me}\right] \tag{1.5}$$

On the other hand, in a linearly polarized light, $\mathbf{k} \parallel \mathbf{x}, \mathbf{H}^{\omega} \parallel \mathbf{z}$ and $\mathbf{E}^{\omega} \parallel \mathbf{y}$, the difference of the absorption coefficients is also finite.

$$\Delta\alpha = \omega\varepsilon_0\mu_0\mathrm{Im}\left[\chi_{zy}^{me} + \chi_{yz}^{em}\right] \tag{1.6}$$

In this way, the absorption coefficient is depending on the direction of the wave vector even in the unpolarized light. For the unpolarized light in a chiral material that has the chiral point groups such as $222, 422, 622, 32, 23, 432, 1, 2, 3, 4$, and 6, NDD appears in the Faraday geometry where a wave vector $\mathbf{k}$ and a magnetization $\mathbf{M}$ are parallel to each other ($\mathbf{k} \parallel \mathbf{M}$), which is the magnetochiral (MCh) effect (Fig. 1.2c). In addition the similar NDD was predicted in the Voigt geometry ($\mathbf{k} \perp \mathbf{M}$) with the magnetization perpendicular to the electric polarization $\mathbf{P}$ of a polar material that has the polar point groups such as $m, mm2, 3m, 4mm, 6mm, 1, 2, 3, 4$, and 6[17], which is the optical magnetoelectric (OME) effect. The MCh effect is expressed as the change of complex refractive index $\Delta N \propto \gamma(\mathbf{k} \cdot \mathbf{M})$ and the OME effect is expressed as $\Delta N \propto \mathbf{k} \cdot (\mathbf{P} \times \mathbf{M})$, where γ symbolizes chirality. The microscopic origin of NDD is expressed as the dynamical magnetoelectric

susceptibilities introduced by the linear response theory or Kubo formula (see Appendix **??**).

$$\chi^{me}_{\beta\gamma} = \frac{NV}{\hbar}\sqrt{\frac{\mu_0}{\varepsilon_0}}\sum \frac{\langle 0\,|\Delta M_\beta|\,n\rangle\,\langle n\,|\Delta P_\gamma|\,0\rangle}{\omega-\omega_n+i\delta} \tag{1.7}$$

$$\chi^{em}_{\beta\gamma} = \frac{NV}{\hbar}\sqrt{\frac{\mu_0}{\varepsilon_0}}\sum \frac{\langle 0\,|\Delta P_\beta|\,n\rangle\,\langle n\,|\Delta M_\gamma|\,0\rangle}{\omega-\omega_n+i\delta} \tag{1.8}$$

$$\chi^{mm}_{\beta\gamma} = \frac{NV}{\hbar}\mu_0\sum \frac{\langle 0\,|\Delta M_\beta|\,n\rangle\,\langle n\,|\Delta M_\gamma|\,0\rangle}{\omega-\omega_n+i\delta} \tag{1.9}$$

$$\chi^{ee}_{\beta\gamma} = \frac{NV}{\hbar}\frac{1}{\varepsilon_0}\sum \frac{\langle 0\,|\Delta P_\beta|\,n\rangle\,\langle n\,|\Delta P_\gamma|\,0\rangle}{\omega-\omega_n+i\delta} \tag{1.10}$$

Here N is the number of unit cell, V is the volume of unit cell, $\Delta\mathbf{M}$ is the dynamical magnetization, and $\Delta\mathbf{P}$ is the dynamical electric polarization, $|0>$ is the ground state and $|n>$ is the excited state. Thus, the microscopic origin of NDD is the both finite excitations of magnetization and polarization. These excitations depend on the material properties, such as the lattice and magnetic structures. Although we can predict the possible of NDD from the material symmetry, in order to obtain the details, it is necessary to calculate χ^{em} and χ^{me} in each material.

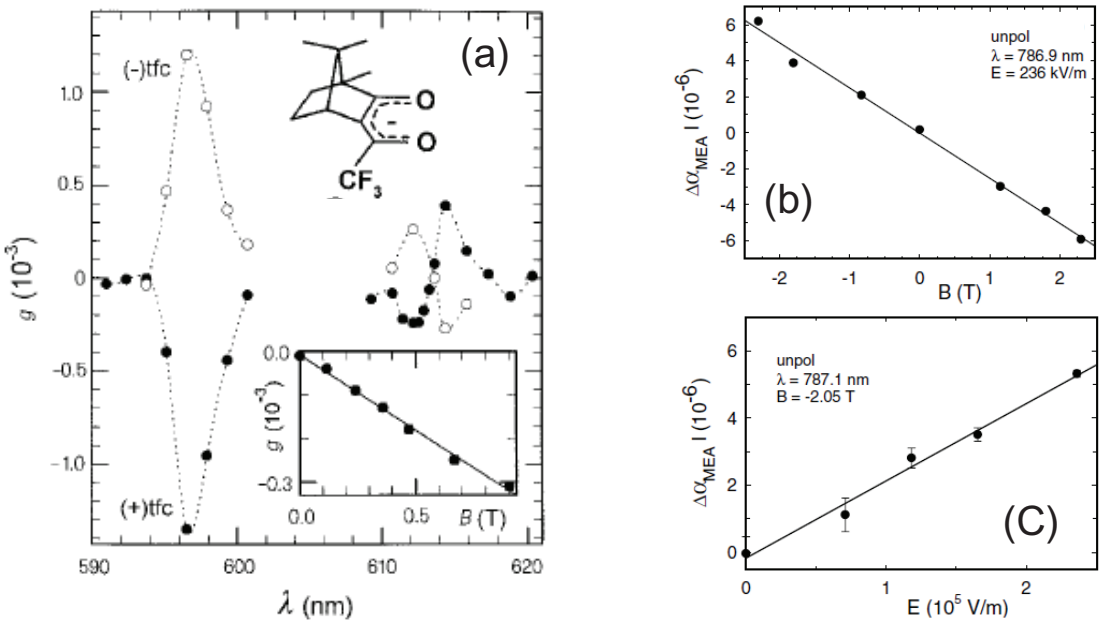

Figure 1.3: **Observation of magnetochiral effect and optical magnetoelectric effect via optical transition.** (a) Rikken *et al.* observed NDD in the chiral molecular Eu((±)tfc)$_3$ with the external magnetic field. g indicates the difference of luminescence intensity between the magnetic field parallel to the wave vector and antiparallel to the wave vector. The inset figure shows the field dependence of the magnetochiral anisotropy and the inset sketch expresses the molecular structure of Eu(tfc)$_3$. Reprinted figure from [18]. Copyright ©1997, Rights Managed by Nature Publishing Group. (b),(c) the difference of absorption coefficient in $\pm E$ was measured by the Lock-in amplifier in the AC electric field as the amplitude $\Delta\alpha_{\mathrm{MEA}}$. $\Delta\alpha_{\mathrm{MEA}}$ was plotted as a function of amplitude of (b) magnetic field B and (c) electric field E. Reprinted figure from [19]. Copyright 2002 by the American Physical Society.

NDD in optical region

After the prediction of NDD by Wagnière and Meire, and Barron and Vrbancich, NDD was first observed by Rikken *et al.* in visible region[18]. They utilized the luminescent transition in Eu((±)tfc)$_3$ and showed the magnetochiral luminescence anisotropy in unpolarized light as shown in Fig. 1.3(a). They observed the NDD depending on the sign and magnitude of magnetic field in the situation where the

wave vector was parallel to the magnetic field. Five years after the observation of the MCh effect, Rikken *et al.* also observed the OME effect[19] by using the optically isotropic cubic crystal $Er_{1.5}Y_{1.5}Al_5O_{12}$ (ErYAG) which has narrow and relatively strong optical transitions. They observed the finite difference of absorption coefficient of unpolarized light in the ErYAG crystal with the magnetic field $\mathbf{H} \perp$ the AC electric field at 1.4 kHz $\mathbf{E} \perp \mathbf{k}$ as shown in Fig. 1.3(b). Their results show that the amplitude and sign of the OME effect depend on the direction and amplitude of the electric and magnetic fields. A considerable number of studies have been conducted on NDD in a wide variety of energy regions since Rikken *et al.* observed the NDD due to the MCh and OME effects (Tables 1.1 and 1.2).

Table 1.1: Non-reciprocal directional dichroism owing to the MCh effect observed in several energy regions.

Energy	Controllable by H	Controllable by H&E
Hard X-Ray 20-100 keV (5-25 EHz)	$\{Tb[Ni(pro)_2]_6\}^{3+}$[20] $[Mn\text{-}NIT]_\infty$, $[Co\text{-}NIT]_\infty$[21]	-
UV 3.3-124 e) (0.8-4 PHz)	H4TPPS4[22]	-
Visible 1.7-3.3 eV (425-825 THz)	$Eu(tfc)_3$[18] $[N(CH_3)(n\text{-}C_3H_7)_2(s\text{-}C_4H_9)][MnCr(ox)_3]$[23] CuB_2O_4[24] H4TPPS4[22]	-
Terahertz 0.4-40 meV (0.1-10 THz)	$Ba_2CoGe_2O_7$[25, 26] $X_2CoSi_2O_7$(X=Ca,Sr)[26] $CuFe_{1-x}Ga_xO_2$[27]	-
Microwave 4-400 μeV (1-100 GHz)	metamaterial(Cu chiral wire w/ ferrite)[28] Cu_2OSeO_3[29] CuB_2O_4[30]	-

Table 1.2: Non-reciprocal directional dichroism owing to the OME effect observed in several energy regions.

Energy	Controllable by H	Controllable by H&E
X-Ray 2-20 eV (0.5-5 PHz)	-	$GaFeO_3$[31]
Visible 1.7-3.3 eV (425-825 THz)	$GaFeO_3$[32] CuB_2O_4[33, 24, 34]	-
Infrared 1.2 meV-1.7 eV (0.3-425 THz)	SL($LaMnO_3$/$SrMnO_3$/$LaAlO_3$) [35]	ErYAG[19] N_2 Gas[36]
Terahertz 0.4-40 meV (0.1-10 THz)	$Ba_2CoGe_2O_7$[37] $BiFeO_3$[38]	(Eu,Y)MnO_3[39] (Gd,Tb)MnO_3[40] $MnWO_4$[41]
Microwave 4-400 μeV (1-100 GHz)	Cu_2OSeO_3[42]	-

NDD owing to the magnon excitations in terahertz and microwave regions

NDD has been observed owing to the optical transitions in optical regions ($\sim$ eV). On the other hand, in the terahertz and microwave regions the NDD around the magnetic resonance excitations has been discerned. In particular, the electromagnon[43, 44], which is the electrically active magnon mode, shows notable NDD owing to the large electromagnetic coupling. Miyahara and Furukawa[45, 46] show that the origin of NDD in the Nambu-Goldstone magnon modes is the toroidal magnon which is the dynamical toroidal moment $\mathbf{T}^d = (\Delta\mathbf{P}^* \times \Delta\mathbf{M} - \Delta\mathbf{M}^* \times \Delta\mathbf{P})/2$, where $\Delta\mathbf{M}$ and $\Delta\mathbf{P}$ are the fluctuations of $\mathbf{M}$ and $\mathbf{P}$, respectively. It indicates that the NDD of Nambu-Goldstone mode is not directly related to the finite $\mathbf{P}\times\mathbf{M}$ but the finite $\Delta\mathbf{P} \times \Delta\mathbf{M}$ is essential for the NDD of Nambu-Goldstone mode.

In 2011, Kézsmárki *et al.*[37] and Takahashi *et al.*[39] first observed the OME effect owing to the electromagnon excitation in multiferroics with large magnetic fields in the terahertz region, respectively. Kézsmárki *et al.* studied the multiferroic antiferromagnet $Ba_2CoGe_2O_7$ which has the magnetoelectric coupling caused by the metal ligand hybridization mechanism[47] as shown in Fig. 1.4(a). Figure 1.4(a) shows that the absorption coefficients are dependent on the sign of the magnetic field. The absorption coefficients are also shown to depend on the sign of the polarization in their paper. In the magnetic field along [100], $Ba_2CoGe_2O_7$ has the chiral point group $mm'2'$. Bordács and Kézsmárki *et al.*[25] also observed the MCh effect by using $Ba_2CoGe_2O_7$ under the large magnetic field in the terahertz region [Fig. 1.4(b)]. Miyahara and Furukawa calculated the dynamical susceptibilities in $Ba_2CoGe_2O_7$, and they are consistent with the experimental results[48].

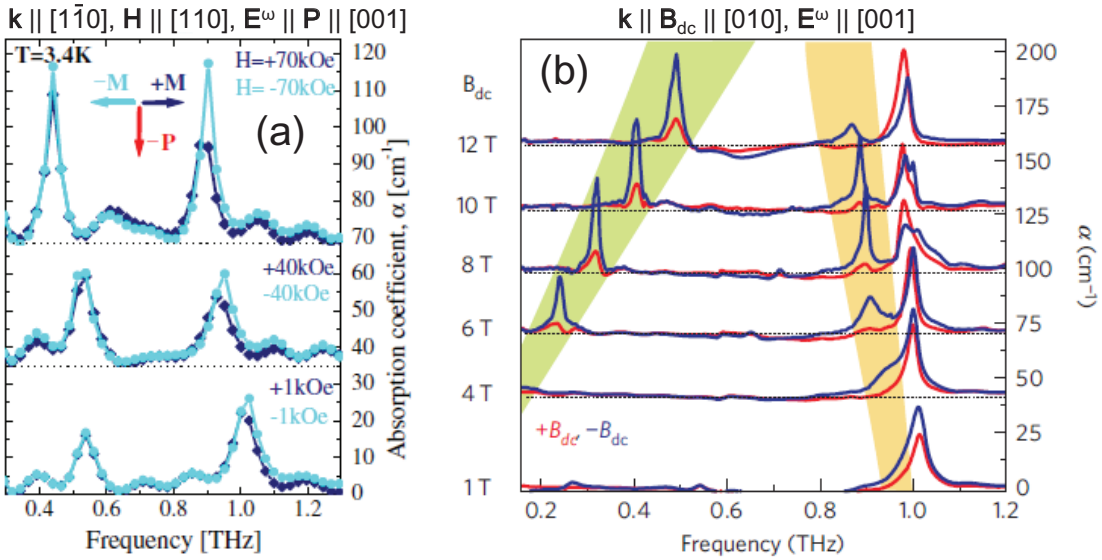

Figure 1.4: **Non-reciprocal directional dichroism owing to electromagnon in $Ba_2CoGe_2O_7$ in terahertz region.** (a),(b) The absorption coefficient of the polarized terahertz light is presented in $Ba_2CoGe_2O_7$ with (a) $\mathbf{k} \parallel \mathbf{P} \times \mathbf{H}$[37] and (b) the magnetic field $\mathbf{B}_{dc} \parallel \mathbf{k}$[25] in antiferromagnetic state. (a) Reprinted figure from [37]. Copyright 2011 by the American Physical Society. (b) Reprinted figure from [25]. Copyright ©2012, Rights Managed by Nature Publishing Group.

On the other hand, Takahashi *et al.* utilized the multiferroic helimagnet $Eu_{0.55}Y_{0.45}MnO_3$ with the polarization induced by the spiral spin structure[49]

which can be controlled by the poling electric field. Miyahara and Furukawa calculated the dynamical susceptibilities in a multiferroics with the spin current mechanism, and suggested the possibility of completely non-reciprocal (one-way) absorption of electromagnetic waves[46].

A few years after the observation of NDD in the terahertz region, NDD has been reported in the microwave region by using magnon excitations in multiferroics Cu_2OSeO_3[42, 29], CuB_2O_4[30], and the metamaterial[28]. Okamura *et al.* observed the non-reciprocal microwave absorption depending on the chirality and the sign of the magnetic field in the multiferroic helimagnet Cu_2OSeO_3 in which the magnetoelectric effect can be induced by the metal ligand hybridization mechanism as shown in Fig. 1.5(a)[42]. They obtained the NDD owing to the conical, skyrmion and ferromagnetic magnon excitations. In Voigt geometry, NDD was observed in Cu_2OSeO_3 [Fig. 1.5(b)] and they indicated that the amplitude of NDD depended on P/M as shown in Fig. 1.6. Mochizuki calculated the dynamical susceptibilities in Cu_2OSeO_3, and they are almost consistent with the experimental results[50]. Recently, Nii *et al.* reported the MCh effect owing to the paramagnetic resonance in CuB_2O_4 and they clarified the difference of the magnetic field directional dependence of NDD between the MCh effect and the classical non-reciprocal magnon mode[30]. They explained their results from the classical calculation of the dynamical magnetoelectric susceptibilities, $\chi_{zy}^{em} \propto \frac{\partial \Delta P_z}{\partial H_y^{\omega}}$, by using the Landau-Lifshitz-Gilbert equation[52].

Thus, the MCh and OME effects can be observed also in the microwave region. Nevertheless, there are still several issues to be explored for NDD in the microwave regime owing to the magnetic excitations. The magnetic excitations in the microwave region are the paramagnetic or ferromagnetic resonance. The excitations in long period magnetic structures such as the conical or skyrmion lattice are also discerned as mentioned above. The microwave NDD owing to the staggered antiferromagnetic magnon excitation has never been reported, because the antiferromagnetic magnon excitation energy tends to be so higher than the microwave region in almost antiferromagnets. Incidentally, while the magnetic control of the microwave NDD has been reported, the electrical control of the microwave NDD is not reported so far.

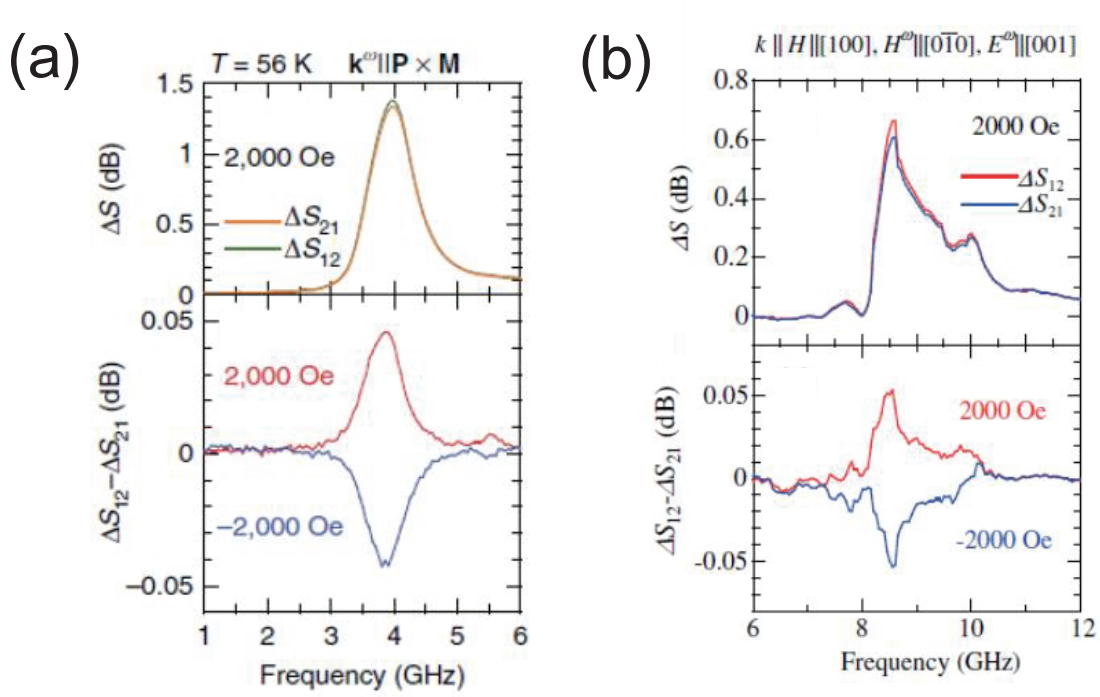

Figure 1.5: **Non-reciprocal directional dichroism in Cu_2OSeO_3 in microwave region.** (a),(b) Microwave absorption spectra ΔS are plotted as a function of frequency and the difference of microwave absorption $\Delta S_{12} - \Delta S_{21}$ which indicates NDD is also plotted in Cu_2OSeO_3 with (a) $\mathbf{k} \parallel \mathbf{P} \times \mathbf{M}$[42] and (b) $\mathbf{k} \parallel \mathbf{M}$[29] in the ferrimagnetic state. (a) Reprinted figure from [42]. Copyright ©2013, Rights Managed by Nature Publishing Group. (b) Reprinted figure from [29]. Copyright 2015, by the American Physical Society.

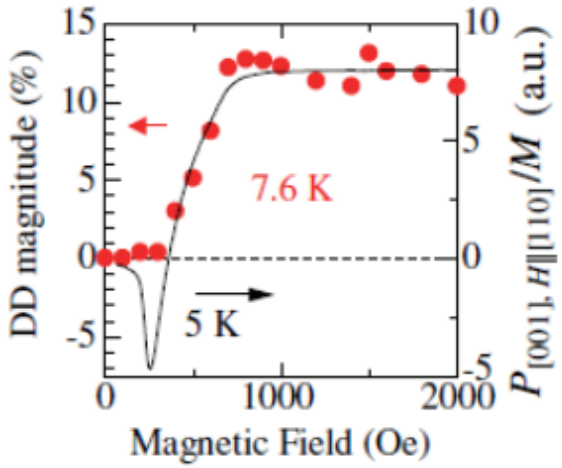

Figure 1.6: **Magnetic field dependence of NDD in Cu_2OSeO_3 in microwave region.** The amplitude of NDD $2(\Delta S_{12} - \Delta S_{21})/(\Delta S_{12} + \Delta S_{21})$ is plotted as a function of the magnetic field. The variation of P/M is also shown in the same figure for comparison. Reprinted figure from [29]. Copyright 2015, by the American Physical Society.

1.3 Non-reciprocal magnon propagation in non-centrosymmetric ferromagnets

In this section, let us consider the non-reciprocity of magnon propagations. The large difference from the non-reciprocity of electromagnetic waves is the interactions which form the waves. While electromagnetic waves are described by the Maxwell's equations, the magnon propagates via the exchange interaction, the magnetic dipole-dipole interaction and other magnetic interactions, so these two are basically different physics.

For instance, magnetostatic waves, which are the classical magnetic waves via the magnetic dipole-dipole interactions in ferromagnets (see Appendix A.2), have the non-reciprocity when they propagate on the surface of the sample. On the surface, SIS is broken and it has polar symmetry. Thus the non-reciprocity of magnetostatic waves has the same symmetry to the OME effect [Fig. 1.7(a)]. However, the magnetostatic waves are the classical waves that obey the Maxwell's equations in the magnetostatic limit, so it is reasonable to suppose that the both

non-reciprocities have the same symmetry.

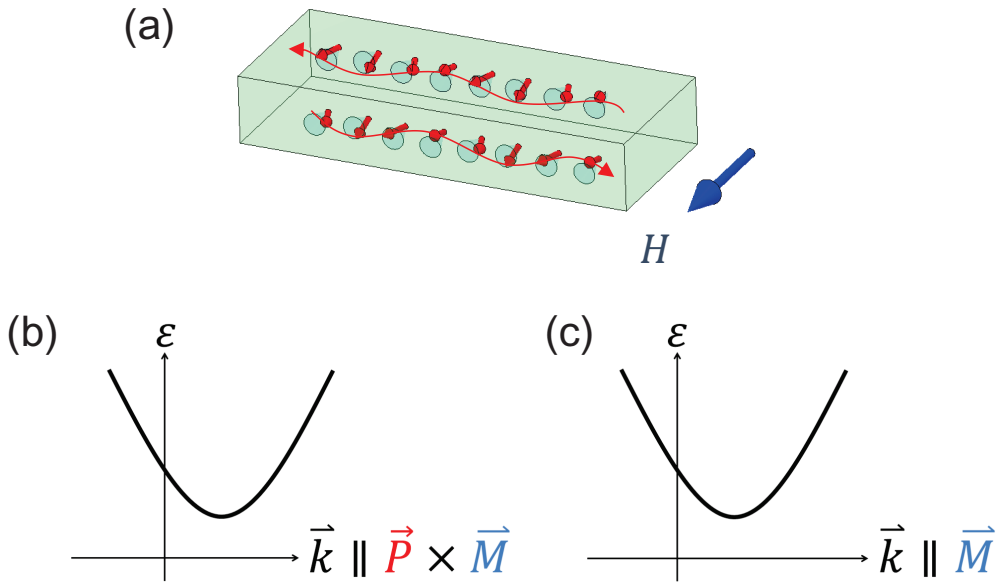

Figure 1.7: **Non-reciprocal magnon propagation modes.** (a) The surface magnetostatic wave or the Damon-Eshbach mode (DEM)[53] propagates along one direction parallel to $\mathbf{M} \times \mathbf{n}$, where $\mathbf{n}$ is the normal vector of the surface. (b),(c) The magnon excitation energy in the IFMS is plotted in the wave number space with (b) $\mathbf{k} \parallel \mathbf{P} \times \mathbf{M}$ in a polar magnet and (c) $\mathbf{k} \parallel \mathbf{M}$ in a chiral magnet.

On the other hand, both SIS and TRS breaking modifies the magnon band dispersion asymmetric[54, 55] owing to the antisymmetric exchange interactions such as the Dzyaloshinskii-Moriya (DM) interaction[56, 57]. Therefore the asymmetric magnon band dispersion may provide the non-reciprocal magnon propagation. The DM interaction originates from the relativistic spin-orbit interaction, so the magnon non-reciprocity is regarded as the relativistic band effect. Here, one question is whether the magnon modes via the quantum magnetic interactions, such as the exchange interaction and the DM interaction, have a non-reciprocal mode like the DEM. In fact, it has been theoretically predicted so far that the non-reciprocity due to the asymmetric band has been realized without TRS and SIS. Kataoka[55] introduced the asymmetric magnon band dispersion in the induced ferromagnetic state (IFMS) of a cubic and chiral helimagnet as shown in Fig. 1.7(b) by the

Hamiltonian in the form of continuum approximation

$$H = \int d\mathbf{r} \left[\frac{J}{2a} (\nabla \mathbf{S})^2 - \frac{D}{a^2} \mathbf{S} \cdot (\nabla \times \mathbf{S}) \right] + H_A + H_Z, \tag{1.11}$$

where $\mathbf{S}$ is the spatially dependent spin moment divided by $\hbar$ (Plank constant divided by 2π), J is the ferromagnetic exchange interaction, D is the DM interaction, a is the lattice constant, and H_A and H_Z are the magnetic anisotropy and Zeeman energy, respectively. From the above Hamiltonian he obtained the following magnon dispersion with $\mathbf{k} \parallel \mathbf{M}$.

$$\hbar\omega(k) \simeq Ja^2 S(k - \frac{D}{Ja})^2 + H_{ex} \tag{1.12}$$

Here H_{ex} is an external magnetic field. Why is the magnon state at finite wave number the smallest excitation energy state? This mechanism can be easily understand as the following. The DM interaction favor the right angle between the two adjoining spins. The competition of the ferromagnetic exchange interaction and the DM interaction results in the spiral spin structure as shown in Fig. 1.8(a). When the magnetic anisotropy or external magnetic field is strong enough, collinear ferromagnetic state is favored but the asymmetric magnon band is realized as a remnant of spiral structure.

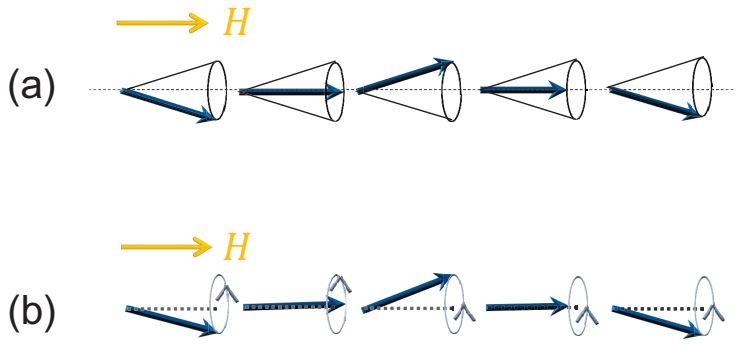

Figure 1.8: **DM interaction makes chirality in static and dynamical spin states.** (a) In the magnetic field, the conical magnetic state appears as the ground state owing to the ferromagnetic exchange interaction and the DM interaction. The pitch of spiral is depending on the ratio of D and J. (b) In the IFMS, the smallest excited state at a given moment has the similar spiral structure, the pitch of which is also dependent on the ratio of D and J.

Table 1.3: Non-reciprocal magnon propagation owing to the asymmetric band.

Method	Polar	Chiral
SPEELS	[Film] Fe/W(110)[58, 59]	-
BLS	[Film] Pt/CoFeB[60] [Film] Py/Pt[61, 62]	-
Microwave antennae	[Film] YIG/GGG[63]	-

Recently, the non-reciprocal magnon propagations in the polar magnetic monolayer or multilayer film have been reported by using the specific methods as shown in Table 1.3. Zakeri *et al.* observed the non-reciprocal magnon propagation by using the spin polarized electron energy loss spectroscopy (SPEELS) in 2 atomic-layers Fe film on W (110) substrate[58, 59] [Fig. 1.9]. SPEELS detects the magnon propagation energy ($\sim$ THz) and wave vector ($\sim$ Å^{-1}) by the interaction between the spin polarized electron and magnon. They showed that the asymmetric magnon band appeared by the interfacial DM interaction on the film [Fig. 1.9(a)] and that the magnon life time depends on the structure of the asymmetric magnon band [Fig. 1.9(b)]. The interfacial DM interaction makes the magnon band asymmetric like the DM interaction in a polar material as shown in Fig. 1.7b. After the observation by Zakeri *et al.*, many research groups started to detect the non-reciprocal magnon propagation by other methods. Half year ago of our report, three groups independently observed similar non-reciprocal propagation of magnon due to the interfacial DM interaction in magnetic multilayers by using the Brillouin light scattering (BLS) method[60, 61, 62]. Nembach *et al.* found that the difference of magnon frequencies with fixed $\mathbf{k}$ depended on the thickness of the film as shown in Fig. 1.10. Its thickness dependence indicates the amplitude of the DM interaction changes with the film thickness. On the other hand, Zhang *et al.* observed the non-reciprocal magnon propagation in the centrosymmetric ferrimagnet $Y_3Fe_5O_{12}$ (Yttrium Iron Garnet, YIG) film on the $Gd_3Ga_5O_{12}$ (Gadolinium Gallium Garnet, GGG) substrate owing to the electric field which worked as like the DM interaction in a polar material[63].

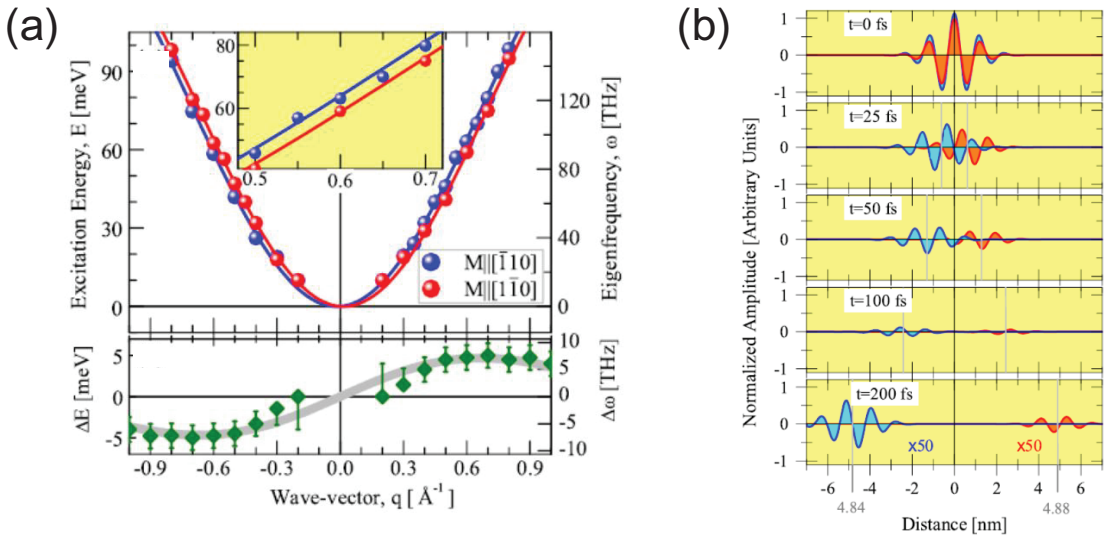

Figure 1.9: **Asymmetric magnon band dispersion obtained by SPEELS in Fe/W(110).** (a) The asymmetric magnon band dispersion obtained by SPEELS in 2 atomic-layers Fe film on W(110) substrate. (b) From the analysis of the SPEELS data the magnon damping distance is predicted. Reprinted figures from [59]. Copyright 2012, by the American Physical Society.

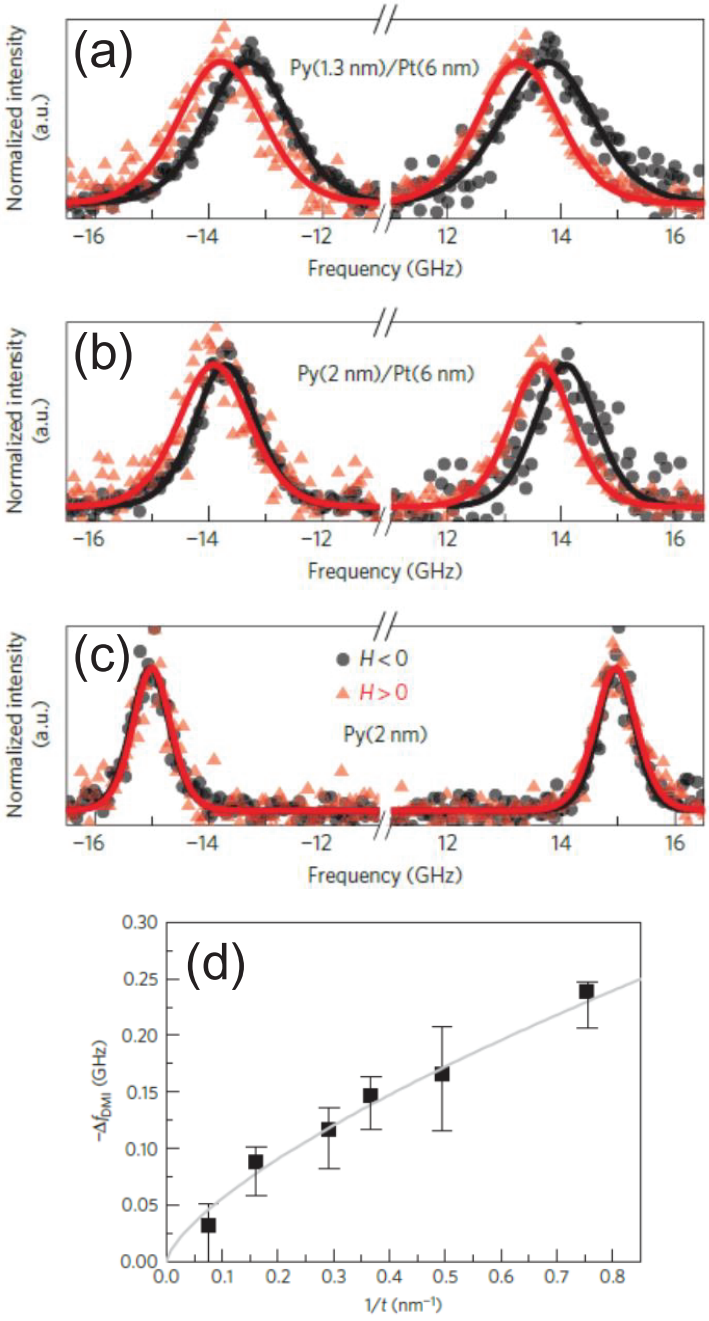

Figure 1.10: **Asymmetric magnon band dispersion obtained by BLS in Py/Pt.** (a)-(c) BLS spectra in the Py/Pt films with $|\mathbf{k}|$ =16.7 μm^{-1} are plotted as a function of frequencies of Stokes and anti-Stokes processes. (d) The thickness t dependence of the difference of peak frequencies $-\Delta f_{\mathrm{DMI}}$ obtained from the results in (a)-(c). Reprinted figures from [61]. Copyright ©2015, Rights Managed by Nature Publishing Group.

The studies of the non-reciprocal magnon propagation are far from sufficient. In particular, the non-reciprocities in a chiral material have never been reported so far. In ferromagnetic films or a polar material, it is difficult to discriminate the non-reciprocal magnon propagation due to the asymmetric band from the DEM caused by the magnetic dipole-dipole interaction. In contrast, the magnon non-reciprocity of the chiral asymmetric band could be clearly identified, because it is expected that the chiral magnon band is asymmetric along $\mathbf{k} \parallel \mathbf{M}$. Therefore the observation of the magnon non-reciprocity is anticipated by using even the chiral bulk magnet.

1.4 Purpose

As mentioned above, the non-reciprocal responses in the microwave region owing to the magnon excitation has been performed for the materials which has the strong magnetoelectric coupling such as multiferroics. Nevertheless, some problems, which are interesting basically and for application, remain unanswered. In order to resolve them, we studied the following three researches in this thesis.

1. We try to electrically control the microwave non-reciprocity by using the type-II multiferroic helimagnet $Ba_2Mg_2Fe_{12}O_{22}$, where the electric polarization is induced by the inverse DM mechanism.

2. We observe the antiferromagnetic magnon modes in the microwave region by using the multiferroic antiferromagnet $Ba_2MnGe_2O_7$ where it is expected that the exchange interaction and the magnetic anisotropy constant are weak. We demonstrate that the $Ba_2MnGe_2O_7$ provides the microwave non-reciprocity under low magnetic fields to consider the difference of the non-reciprocity in the two antiferromagnetic magnon modes. While NDD for antiferromagnetic resonance in a high magnetic field was reported in the terahertz region, our study uncovers the detail magnetic field dependence of the energy dependent NDD of the classical (textbook-type) antiferromagnetic resonance in a non-centrosymmetric antiferromagnet.

3. The magnon non-reciprocal propagation has been only reported in the film with the polar-type DM interaction. The non-reciprocal magnon propagation

due to the bulk crystal symmetry breaking and that with the chiral-type DM interaction have never been studied so far. In this thesis I observe the non-reciprocal magnon propagation by using a bulk single crystal of the chiral ferrimagnet $LiFe_5O_8$ and the micro-fabricated microwave antennae.

Chapter 2

Experimental method

2.1 Microwave measurement

2.1.1 Coplanar wave guide

The microwave electric field and magnetic field distributions of the coplanar waveguide (CPW)[12] are shown in Fig. 2.1, which is the transverse electric and magnetic (TEM) mode. The characteristic impedance of the CPW depends on the dielectric constant of the dielectric substrate and the ratio of the strip line width and the gap between the strip line and the ground plane. We calculated the characteristic impedance to set it 50 Ω by using the App CAD (Hewlett Packard).

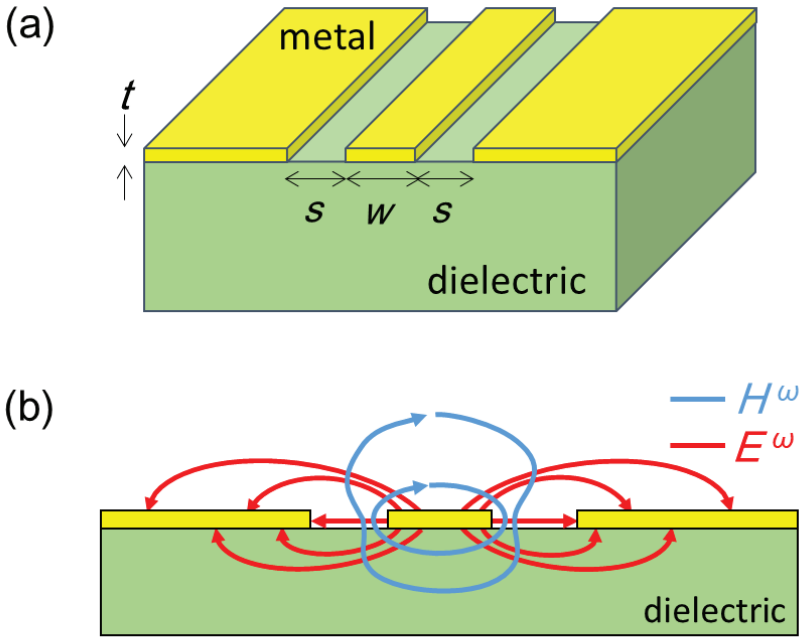

Figure 2.1: **Electromagnetic fields distribution of TEM mode in CPW.** (a) The CPW has one strip center line (width w) and two ground plane (gaps s) in the same plane (thickness t). (b) The alternating current propagates in the strip line and provides the AC magnetic field H^{ω} like the Oersted-field and the AC electric field E^{ω} perpendicular to the direction of the AC magnetic field and the alternating current.

2.1.2 Micro-fabricated microwave antenna

The Spatial distribution of the AC magnetic field in waveguides depends on the structure of waveguides. For example, if the sample on the center of the CPW is smaller than the slot line w, the sample is affected by the uniform microwave magnetic field and the uniform magnon is excited. In contrast, if the sample is larger than w, the microwave magnetic field is modulated in the sample and the excited magnon is the superposition of several magnon modes with different wave numbers. The wave number of the coupled magnon mode is analyzed by the Fourier transformation of the amplitude of the microwave electric current[64]. Figure 2.2(a) illustrates the meander-type antenna which was designed by the author to observe the non-reciprocal magnon propagation in Section 3.3. The conducting path goes upward and turns back repeatedly 20 times in the antenna. The magnetic field that the electric current along the meander-line provides is spatially oscillated. Vlaminck and Bailleul calculated the wave number dependence of the microwave magnetic field of coupled mode in the meander-type antenna by the Fourier transformation of the microwave current[64]. We follow their method and gain the wave number of the coupled mode in the simpler meander antenna designed by the author. The width and the space of the electric path in the antenna are $a = 5$ μm and the height of the antenna is $2b \simeq 1$ mm, so the wave length of meander structure is 20 μm. At the center of the antenna ($y = 0$), the electric current only flows along the y direction. The y-direction electric current is alternating along the horizontal x direction with the wave length $\lambda = 20$ μm [Fig. 2.2(b)]. The Fourier transformation of the amplitude of y-direction current shows that the y-direction electric current has the broad peak around $k = 2\pi/(20$ μm$) = 0.314$ μm^{-1} as shown in Fig. 2.2(c). Its HWHM (Half-width at half-maximum) is about 0.007 μm^{-1}. The magnetic field induced by the y-direction electric current has the x and z components, so the spatially oscillating magnetic field of the coupled mode at $y = 0$ also has the x and z components. On the other hand, at the edge of the antenna ($y = \pm b$), the x-direction electric current only flows uniformly as shown in Fig. 2.2(d). The Fourier transformation of the x-direction electric current provides a broad peak of the amplitude of the x-direction electric current around $k = 0$ as shown in Fig. 2.2(e). Its HWHM is also about 0.007 μm^{-1}. The magnetic field of coupled mode at the edge of antenna has the

y and z components. Thus this microwave antenna can couple and excite the magnon mode with wave number $k \sim 0$ and $k \sim 2\pi/\lambda$.

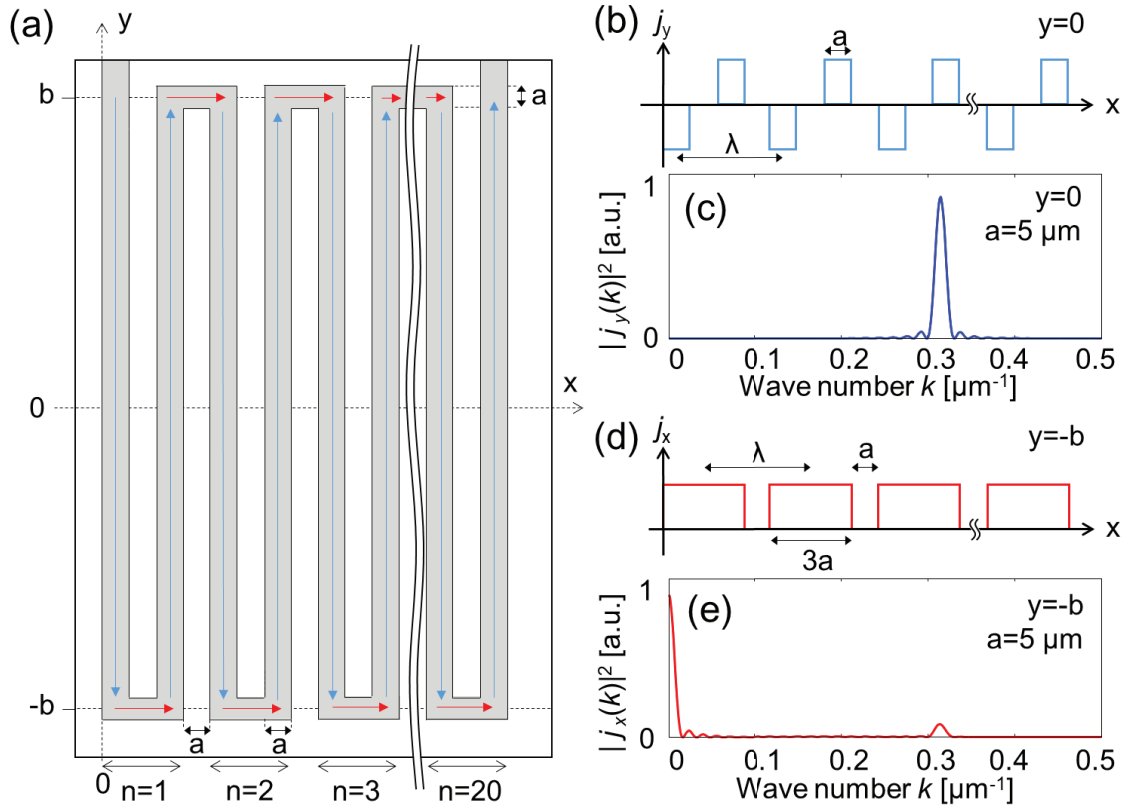

Figure 2.2: **Microwave current properties in wave number space at meander-type microwave antenna.** (a) Sketch of the meander antenna used for the experiment in Section 3. The gray thick line shows the electric path. The arrows along the electric path indicate the microwave current. (b) y-direction current j_y as a function of x at $y = 0$. (c) Square of Fourier transformed current $|j_y(k)|^2$ at $y = 0$. (d) The microwave current along x, j_x, as a function of x at $y = -b$. (e) Square of Fourier transformed current $|j_x(k)|^2$ at $y = -b$. Reprinted figures from [65]. Copyright 2015, by American Physical Society.

2.1.3 Probes of microwave measurement

We fabricated the two microwave measurement probes for the ranges DC-20 GHz (probe-I)[Fig. 2.4(c)] and DC-40 GHz (probe-II)[Fig. 2.5(b)]. The probes should be long forms, because the sample in the microwave device was measured in the

magnetic field in a wide temperature range (1.8 - 300 K) by using the He4 superconducting magnet (Split Pair Magnet) with VTI system (OXFORD INSTRUMENTS Spectromag) as shown in Fig. 2.3. I used the two types of measurement setup, which is connected to the measurement probe [Fig. 2.3]. Figure 2.3 shows the broad band ESR (electron spin resonance) system by using the Network Analyzers for 0.3 MHz-20 GHz (Agilent Technologies E5071C) and for 10 MHz-40 GHz (Agilent Technologies N5230A). In this system we can measure the reflective signals of port 1 S_{11} and of port 2 S_{22} and the transmittance signals from port 1 to port 2 S_{21} and from port 2 to port 1 S_{12}. S_{ij} is defined by

$$S_{ij}[\mathrm{dB}] = 10 \log \frac{A_{\mathrm{in,port}i}[\mathrm{W}]}{A_{\mathrm{out,port}j}[\mathrm{W}]}, \tag{2.1}$$

where $A_{\mathrm{in,port}i}$ is the amplitude of transmission wave in port i and $A_{\mathrm{out,port}j}$ is the amplitude of incident wave from port j. We utilized the semi-flexible cables for DC-20 GHz (HUBER+SUHNER SUCOFLEX 104) and for DC-40 GHz (Waka R2BKMKM) to connect the instruments and probes.

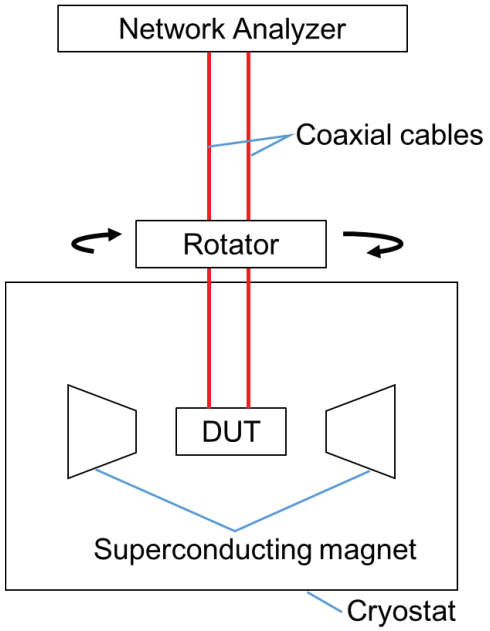

Figure 2.3: **Setup of microwave measurement in magnetic field at liquid Helium temperature.** Sketch of the measurement system that we used in this thesis. We measured the microwave response of two ports by utilizing the Network Analyzer.

Next, we introduce the details of the probes and devices. Firstly, we explain the detail of the probe-I. The probe-I has the microwave semi-rigid cable for DC-20 GHz (KEYCOM ULT-04), of which the length is about 1.2 m. It consists of the 1 m hollow pipe (SUS304), the four coaxial cables for applying the electric field and measuring the electric current, the four copper wires for the temperature control, and the sample holder. Secondly, we show the detail of the probe-II. It is formed by the 1 m hollow pipe (SUS304) with the thermal anchors, the microwave semi-rigid cable for DC-40 GHz (Waka SP-22) which is 1.3 m, the three coaxial cables for applying the electric field and measuring the electric current, the four copper wires for the temperature control, and the sample holder. The all connectors used in the interface between the cryostat and the outer space are closely sealed by a hermetic seal. The connectors on the sample holder only consist of the non-magnetic materials such as BeAu. The characteristic impedance of all the connectors and cables for microwave is 50 Ω. The both probes can be connected to the two types of sample holders for the measurement in the in-plane magnetic field [Fig. 2.4(a) and 2.4(b)] and in the magnetic field perpendicular to surface [Fig. 2.5(a)].

Finally, we show the details of microwave devices that we used in the current thesis. We designed the microwave devices to observe the amplitude of the microwave transmission or reflection through samples [Fig. 2.4(a) and 2.5(a)] and the amplitude of the magnon propagation as the microwave transmittance by using the micro-fabricated antenna [Fig. 2.4(b)]. In order to measure the simple microwave absorption due to magnon excitations, we measure the reflection signal S_{11} with the sample on the edge of the short CPW as shown in Fig. 3.4(a). The CPW patterned devices are designed by the author and made by *Kansai electronics Co., Ltd.*. It consists of the glass-epoxy substrate sandwiched between copper films (Panasonic R-5775, dielectric constant $\epsilon_r = 3.38$). In order to measure the non-reciprocal microwave propagation, we measure the transmission signals S_{21} and S_{12} along the CPW through samples as shown in Fig. 4.1(c). For the measurement of the nonreciprocal magnon propagation micro-fabricated pattern is needed as shown in Fig. 2.4(b). We patterned the meander-type antennae to the sapphire substrate (dielectric constant $\epsilon_r = 9.4$) by using the photo-lithography and the electron beam evaporation and I attached the sapphire substrate to the

glass-epoxy substrate by using the Al wire bonding. The photomask was made by *Toyo Precision Parts MFG.CO.,LTD* and designed by the author.

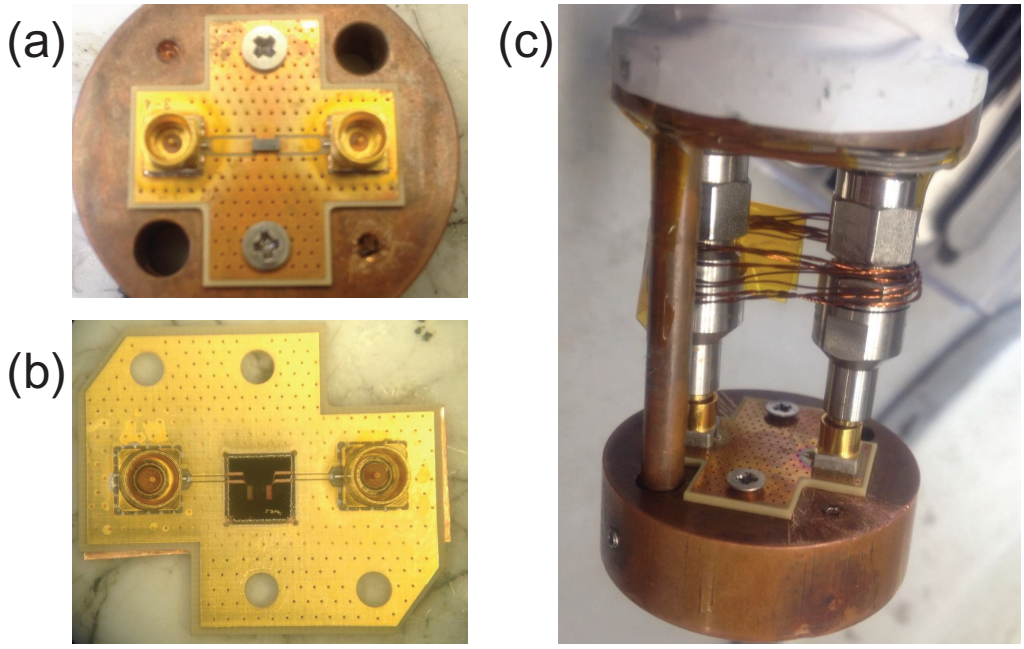

Figure 2.4: **Microwave devices for applying in-plane magnetic field and measurement probe for DC-20 GHz.** (a),(b) The CPW patterned microwave devices with microwave connectors. The distance of two connectors is 16.2 mm. One device has only the macro CPW which is the open or (a) short waveguide. In contrast (b) the other device can be attached to the other substrates with micro-fabricated patterns by the wire-bonding. (c) The sample space of the microwave measurement probe-I that we used in Chapters 3 and 4.

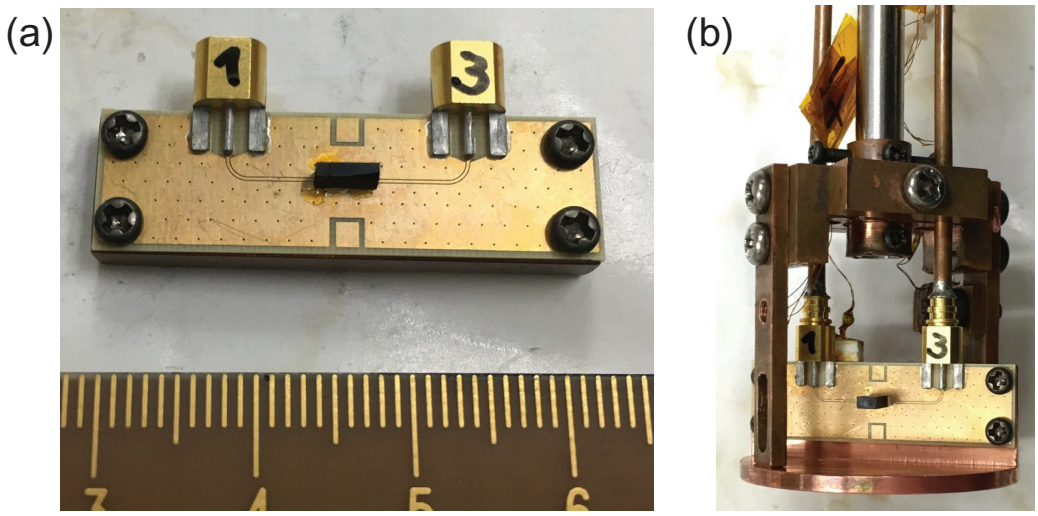

Figure 2.5: **Microwave devices for applying magnetic field perpendicular to surface and measurement probe for DC-40 GHz.** (a) The CPW patterned microwave devices with microwave connectors. (b) The sample space of the microwave measurement probe-II that we used in Chapter 5.

2.2 Preparation of single crystal samples

We prepared the single crystals, $LiFe_5O_8$, $Ba_2Mg_2Fe_{12}O_{22}$ and $Ba_2MnGe_2O_7$, for microwave measurements by using the Flux method and the Floating Zone (FZ) method. Both methods are widely used for the single crystal growth. The Flux method takes a long time ($\sim$ one month) and makes small crystals ($\sim$ mm) compared with the FZ method ($\sim$ one week, $\sim$ cm). However it provides the higher quality crystal than the FZ method. We characterized the obtained crystals by using the Laue and the Diffractometer methods of X-ray diffraction and the magnetization measurement by MPMS (Quantum Design). The crystal axis was found by the Laue method and the crystals were cut and shaped by the diamond cutter.

2.2.1 $LiFe_5O_8$

The single crystals of $LiFe_5O_8$ were prepared by the Flux method. According to the Beregi *et al.*'s paper[66], We chose the PbO-B_2O_3 flux and the Pt crucible.

The chemical formula and the mixing molar ratio that I used are the following.

$$3Li_2CO_3 + 10Fe_3O_4 + \frac{5}{2}O_2 \rightarrow 2LiFe_5O_8 + CO_2 \uparrow \tag{2.2}$$

Li_2CO_3	Fe_3O_4	B_2O_3	PbO
1.17 mol%	0.97 mol%	2.94 mol%	4.43 mol%

First, we increased the temperature at rate 50 °C/hour up to 1100 °C, and kept in 12 hours, then decreased the temperature at rate −1°C/hour to 600 °C. We got the mm-scale single crystals of $LiFe_5O_8$ by crushing the obtained crystals to separate the $LiFe_5O_8$ and Flux materials.

2.2.2 $Ba_2Mg_2Fe_{12}O_{22}$

The single crystals of $Ba_2Mg_2Fe_{12}O_{22}$ were also prepared by the Flux method. Following the Ishiwata *et al.*'s paper[67], we chose the Na_2O-Fe_2O_3 flux and the Pt crucible. The chemical formula and the mixing molar ratio that we used are the following.

$$2BaCO_3 + 6Fe_2O_3 + 2MgO \rightarrow Ba_2Mg_2Fe_{12}O_{22} + 2CO_2 \uparrow \tag{2.3}$$

$BaCO_3$	MgO	Fe_2O_3	Na_2CO_3
16.33 mol%	16.33 mol%	55.10 mol%	12.24 mol%

First, we increased the temperature at rate 50 °C/hour up to 1420 °C, and kept in 20 hours, then decreased the temperature at rate −0.8 °C/hour to 1000 °C. we obtained the mm-scale single crystals of $Ba_2Mg_2Fe_{12}O_{22}$.

2.2.3 $Ba_2MnGe_2O_7$

We prepared the single crystals of $Ba_2MnGe_2O_7$ by using the FZ method in Hanasaki lab of Osaka university with the help of Dr. Murakawa. Following the Murakawa *et al.*'s paper[68], we mixed the powders of $BaCO_3$, Mn_3O_4 and GeO_2. After four times of the O_2 annealing for 2 days at 1000 °C in the alumina crucible, we obtained the cm-scale single crystal rod by the FZ method in flowing O_2 gas with the growth speed of 0.7 mm/hour.

Chapter 3

Non-reciprocal magnon propagation in a chiral ferromagnet

In this chapter, we show the observation of the non-reciprocal magnon propagation in the bulk chiral ferromagnet $LiFe_5O_8$ where the lattice structure of the bulk breaks SIS.

3.1 Fundamental properties

$LiFe_5O_8$ is crystallized into a spinel-type crystal structure as shown in Fig. 3.1(a). This crystal has the similar structure of magnetite, but in this material Li ions are substituted for the one-fourth of Fe ions at the B site of the spinel structure and the ordered Li ions break the mirror symmetry (space group $P4_132$)[69]. The magnetic moments of Fe ions are ferromagnetically (more precisely, ferrimagnetically) ordered by the ferromagnetic exchange interaction around 900 K[70]. Thus the uniform DM interaction works in the $LiFe_5O_8$ sample, and the effective Hamiltonian can be obtained as follows[55]:

$$H = \int d\mathbf{r} \left[\frac{J}{2a} (\nabla \mathbf{S})^2 - \frac{D}{a^2} \mathbf{S} \cdot (\nabla \times \mathbf{S}) \right] + H_A + H_D + H_Z. \tag{3.1}$$

Here H_D is the magnetic dipole-dipole interaction. In above Hamiltonian without H_A, the helical magnetic structure is realized due to the DM interaction at zero magnetic field as observed in MnSi[71]. Nevertheless, the ferromagnetic state appears in this material, because the DM interaction is weaker than H_A. However we should notice that the magnetic anisotropy is also not so large. Figure 3.1(b) shows the magnetization curves of the $LiFe_5O_8$ sample, which is utilized in this study, for various magnetic field directions. We see from Fig. 3.1(b) that the magnetic anisotropy is small in the $LiFe_5O_8$ sample, because all the magnetization curves do not show hysteresis and saturate in a small magnetic field ($\sim$ 0.2 T). The small anisotropy affected the magnetization curves as the diamagnetic field. The effect of the weak DM interaction can be observed from the viewpoint of the magnon excitation.

As Kataoka theoretically suggested[55], the uniform DM interaction modulates the magnon band asymmetric as shown in Fig. 1.7(c). Therefore the non-reciprocal magnon propagation is expected in this system. However, we must draw attention to the effect of H_D that is dominant in the magnon propagation around $k = 0$, which is known as the magnetostatic waves. For the plate-like sample with the in-plane magnetic field, the magnetostatic wave propagation along the magnetization direction have the negative group velocity and symmetric dispersion relation (for the detailed calculation, see Appendix A.2). H_D is more dominant than the ferromagnetic exchange and the DM interactions up to $k \sim 1/t$, where t is the thickness of the sample. Thus, in order to observe the non-reciprocal magnon propagation

it is necessary to prepare the microwave which can excite the magnons with large k. In this study, we have measured the microwave response of the chiral ferromagnet $LiFe_5O_8$ and the centrosymmetric ferromagnet $Y_3Fe_5O_{12}$ for reference on the micro-fabricated microwave antennae and demonstrated that the magnon propagation along the magnetization direction is non-reciprocal in $LiFe_5O_8$ due to the DM interaction. The $Y_3Fe_5O_{12}$ single crystal was grown by Crystal Systems Corporation. The dimensions of the samples are both $2 \times 0.9 \times 0.6$ mm^3. For both the samples, the widest surface is the (110) plane and the longest direction is $[1\bar{1}0]$.

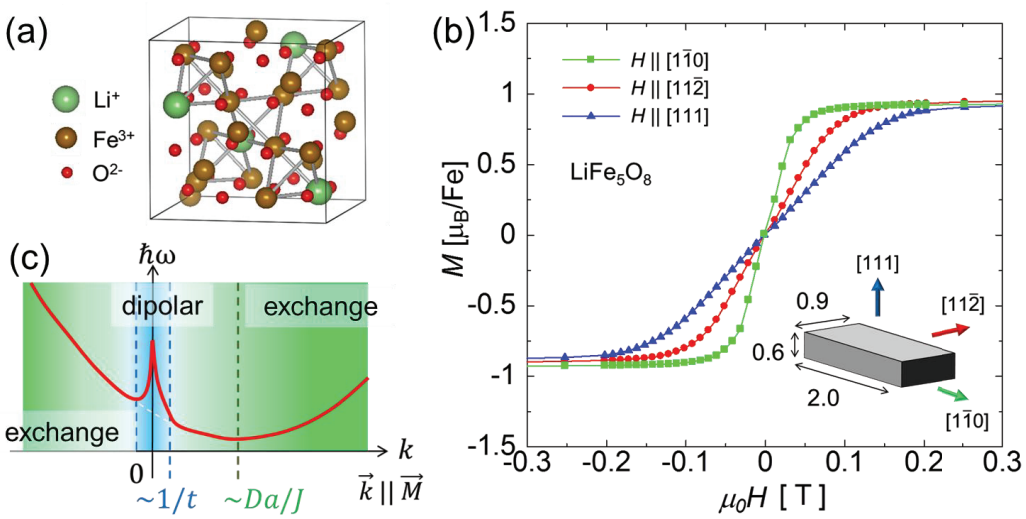

Figure 3.1: **Fundamental properties of $LiFe_5O_8$.** (a) Chiral crystal structure of $LiFe_5O_8$. (b) Magnetization curves of the sample $LiFe_5O_8$ for various magnetic field directions. Inset shows the sample figure and crystal orientations. (c) Sketch of the expected asymmetric magnon band dispersion of $LiFe_5O_8$ in the IFMS. The ferromagnetic exchange and the DM interactions are dominant in the "exchange" region for magnon propagation, whereas the magnetic dipole-dipole interaction is dominant in the "dipolar" region. Reprinted figures from [65]. Copyright 2015, by American Physical Society.

3.2 Ferromagnetic magnon excitation in uniform microwave

Magnetic field dependence of magnon with small wave number

First, let us consider the magnetic excitation in a spatially uniform microwave. We measured the microwave absorption of $LiFe_5O_8$ by using the macro microwave guide line as antenna (see Fig. 3.2 and Section 2.1.1), the superconducting magnet and a vector network analyzer at room temperature. The sample is placed at the edge of the shorted CPW. The macro waveguide makes the spatially uniform microwave magnetic field, such field excites the small wave number ($k \sim 0$) magnon mode (uniform mode). Figures 3.2(b) and 3.2(c) show the microwave absorption spectra under the magnetic fields (0.1, 0.2, 0.3 T). Microwave absorption spectra ΔS_{11} is normalized reflectance S_{11} with the background 1 T, $\Delta S_{11}(\mu_0 H) = S_{11}(\mu_0 H) - S_{11}(1\text{ T})$, similar to the previous paper[72]. For $Y_3Fe_5O_{12}$, the absorption spectrum shows a sharp peak around 4.9 GHz and broad continuum above 5 GHz at 0.10 T. While the spectra keep the almost same spectral shape, their frequencies shifted with increase of the magnetic field. Such similar spectra were already reported by An *et al.*[73]. They identified the origin of the sharp spectra and the continuum as the FMR and the Damon-Eshbach mode, respectively (see Appendix A.2). In the case of $LiFe_5O_8$, they denoted the same tendency of the spectral shape and the magnetic field dependence in $Y_3Fe_5O_{12}$, whereas the frequency scale is higher than that for $Y_3Fe_5O_{12}$. We plot the magnetic field dependence of the FMR frequency for $LiFe_5O_8$ and $Y_3Fe_5O_{12}$ in Fig. 3.2(d). The solid lines are the results of fitting with the theoretical formula Eq.(A.26), where the saturation magnetization M_s and the first-order magnetic anisotropy constant K_1 are, respectively, 2.96×10^5 A/m and -9×10^3 J/m^3 for $LiFe_5O_8$[74], and 1.4×10^5 A/m and -6×10^2 J/m^3 for $Y_3Fe_5O_{12}$[75, 76]. The used fitting parameters are the demagnetization factors for [111], $[\bar{1}\bar{1}2]$, and $[1\bar{1}0]$ direction, $N_{111} = 0.71, N_{\bar{1}\bar{1}2} = 0.237$ and $N_{1\bar{1}0} = 0.053$ for both the $LiFe_5O_8$ and $Y_3Fe_5O_{12}$ samples. They approximately consistent with the sample figure.

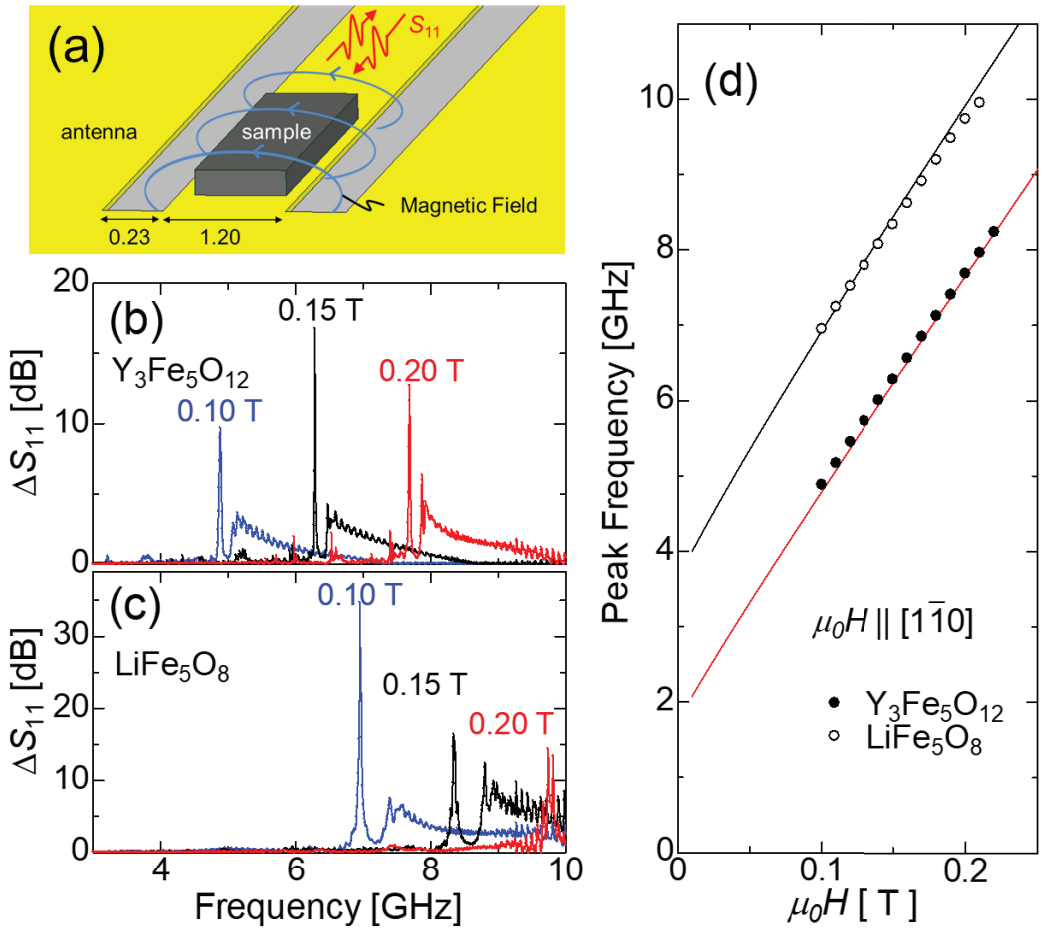

Figure 3.2: **Uniform ferromagnetic resonance modes in $LiFe_5O_8$ and $Y_3Fe_5O_{12}$.** (a) Sketch of experimental setup for the absorption of the uniform microwave magnetic field. (b) and (c) Microwave absorption spectra ΔS_{11} for (b) YIG and (c) $LiFe_5O_8$ in various magnetic fields along $[1\bar{1}0]$ at room temperature. (d) Magnetic field dependence of peak frequency for $LiFe_5O_8$ (open circle) and $Y_3Fe_5O_{12}$ (closed circle). Solid lines are the results of fitting with the theoretical formula Eq. (A.26). Reprinted figures from [65]. Copyright 2015, by American Physical Society.

Mean free path of ferromagnetic magnon

The spectral shape of the FMR absorption has an information about the mean free path of magnetostatic waves. It is important for the experiment of the magnon propagation with two antennae discussed in the next section. The mean free path

l_{free} is expressed as

$$l_{free} = v_g \tau = \frac{v_g}{2\pi \Delta f}, \tag{3.2}$$

where v_g, τ, and Δf are group velocity, relaxation time, and peak width of absorption spectra, respectively. The group velocity is proportional to the slope of the magnon dispersion curve. The magnon dispersion around $k = 0$ is dominated by the dipole-dipole interaction and its shape is sensitive to the boundary condition, which is mentioned in Appendix A.2 for details. The group velocity of $k = 0$ magnetostatic wave is zero in the metalized boundary condition but finite in the free boundary condition. In this case, the sample was on the metal plate in vacuum, so this situation is like intermediate between the metalized and free boundary conditions. We measured the non-reciprocal magnon propagation in the same condition. Therefore, the real group velocity at $k = 0$ is smaller than that in the free boundary condition, but the order remains the same. Of course, the rough estimation here is just only in order to compare the mean free path and the antenna-antenna distance (1 mm). For these reasons, we utilized the group velocity formula in the free boundary condition for the estimation of mean free path:

$$v_g = \frac{d\omega}{dk} = \frac{\gamma \mu_0^2 H_0 M_s t}{4\sqrt{\mu_0^2 H_0^2 - \mu_0 \frac{K_1 H_0}{M_s} - \frac{2K_1^2}{M_s^2} + \mu_0^2 H_0 M_s}}. \tag{3.3}$$

By using Eq. (3.3), we obtained the group velocity as 8.2×10^5 m/s for $LiFe_5O_8$ and 5.0×10^5 m/s for $Y_3Fe_5O_{12}$. From the shape of absorption spectra in Figs. 3.2(b) and 3.2(c), the peak width of absorption spectra Δf is 0.051 GHz for $LiFe_5O_8$ and 0.016 GHz for $Y_3Fe_5O_{12}$ at $\mu_0 H = 0.15$ T. The mean free path is obtained by using Eq. (3.2) with these parameters as 2.6 mm for $LiFe_5O_8$ and 5.0 mm for $Y_3Fe_5O_{12}$. Therefore, the mean free path is larger than the antenna-antenna distance.

3.3 Non-reciprocal ferromagnetic magnon propagation

Observation of magnon propagation using the micro-fabricated antennae

Magnon propagations were measured by the two microwave antennae. We prepared the micro-fabricated microwave circuit with meander-type antennae by using the photo-lithography. The two meander-type antennae made of Au 200 nm / Ti 50 nm thin film are fabricated on a sapphire substrate. The width and the space of slot line is $a = 5$ μm and the height of the antenna is $2b \simeq 1$ mm. The number of meander is 20, which means the slot line goes upward and turns back repeatedly 20 times in the antenna. As illustrated in Fig. 3.3(b), the spatially oscillating magnetic field is induced by the electric current along the conduction line. Thus, the center part of antenna has microwave magnetic field with wave number $k = 2\pi/(20\ \mu\text{m}) = 0.314\ \mu\text{m}^{-1}$ as shown in Fig. 2.2(c). More details are discussed in Section 2.1.2.

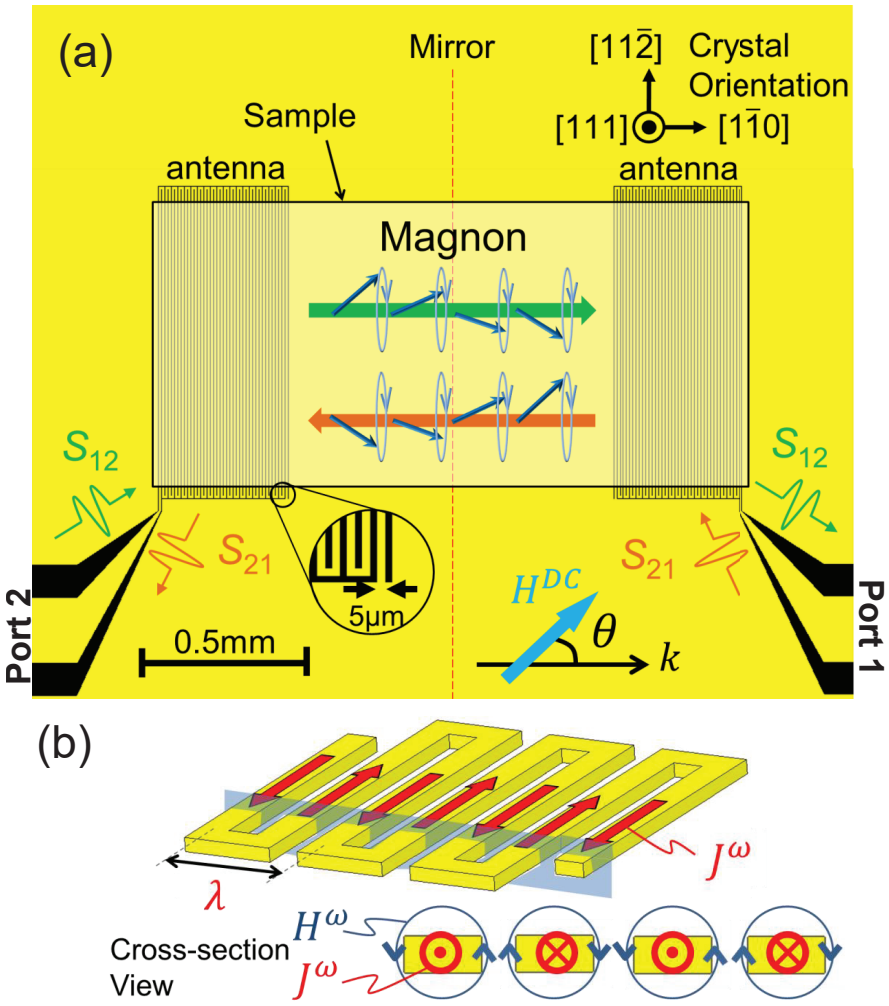

Figure 3.3: **Experimental setup for measurement of magnon propagation with finite wave number.** (a) Experimental setup of the non-reciprocal magnon propagation. The colored region indicates the Au/Ti electrodes. Meander-type microwave antennae are connected to two ports of the network analyzer. The rectangular sample is put on the top of the two antennae. (b) Sketch of the spatially oscillating magnetic fields induced by the microwave current in the meander-type antenna. Reprinted figures from [65]. Copyright 2015, by American Physical Society.

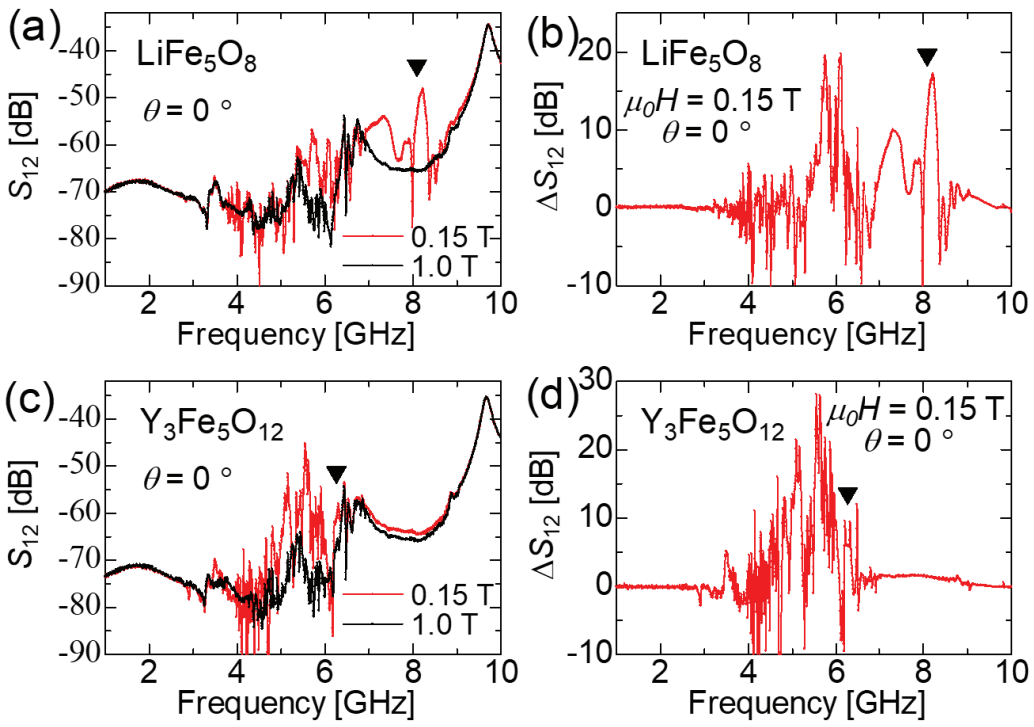

Figure 3.4: **Signal of magnon propagation and microwave cross-talk between two antennae.** (a) The microwave transmittance S_{12} of the $LiFe_5O_8$ sample-placed microwave circuit shown in Fig. 3.3(a) at 0.15 T and 1.0 T at room temperature ($\theta = 0$). (b) The microwave transmittance owing to magnon propagation ΔS_{12} at 0.15 T deduced from the difference of S_{12} from the 1.0 T data. The inverted triangle indicates the FMR mode and the same symbol are shown in (a) at the same frequency. (c) The microwave transmittance S_{12} of the $Y_3Fe_5O_{12}$ sample-placed the circuit shown in Fig. 3.3(a) at 0.15 T and 1.0 T ($\theta = 0$). (d) The microwave transmittance owing to the magnon propagation ΔS_{12} at 0.15 T deduced from the difference of S_{12} from 1.0 T data. The inverted triangle shows the FMR mode, which is the same in (c). Reprinted figures from [65]. Copyright 2015, by American Physical Society.

SIS breaking are necessary for the non-reciprocal phenomena, and our purpose is to observe the non-reciprocal magnon propagation originated from the DM interaction. For this reason, the structure of microwave circuit has mirror symmetry at the center as indicated by the dashed line in Fig. 3.3. We put the sample, $LiFe_5O_8$ and $Y_3Fe_5O_{12}$ which are the same as ones used in Fig. 3.2, on the center of two

antennae with crystal orientation as shown in Fig. 3.3. For $Y_3Fe_5O_{12}$ the device with sample has even mirror symmetry. Figure 3.4(a) shows the microwave admittance S_{12} in the microwave circuit shown in Fig. 3.3. The obtained microwave signal reflects the details of the microwave circuit and magnetic resonance from the sample, but we want to get the signal only related to the magnon propagation. From Fig. 3.2(d), at 1.0 T all magnetic excitations are far above 10 GHz, so S_{12} at 1.0 T reflects the details of the microwave circuit except for the sample. In contrast, S_{12} at 0.15 T is influenced by the both the details of the microwave circuit and the sample. Therefore S_{12} at 1.0 T is thought to be the background signal. To estimate the microwave transmittance only due to the magnon propagation, we deduced the difference of S_{12} from the 1.0 T data, ΔS_{12}. Figure 3.4(b) shows the normalized transmittance ΔS_{12} for $LiFe_5O_8$. In the same way, for the $Y_3Fe_5O_{12}$ sample, the normalized transmittance ΔS_{12} was obtained as shown in Figs. 3.4(c) and 3.4(d).

The asymmetric magnon band provides the non-reciprocal magnon propagation along the magnetization as discussed in Section 1.3. Thus we observed the microwave transmittance with magnetic field angle $\theta = 0$ [Figs. 3.5(a) and 3.5(c)] and 180° [Figs. 3.5(b) and 3.5(d)] for $LiFe_5O_8$ and $Y_3Fe_5O_{12}$ at 0.15 T at room temperature. The spectral shapes of normalized transmittance ΔS_{12} and ΔS_{21} for $LiFe_5O_8$ in Figs. 3.5(a) and 3.5(b), which show the magnon propagation, are obviously different as shown in Fig. 3.5(e). It shows the microwave non-reciprocity. In contrast, the non-reciprocity is almost negligible for $Y_3Fe_5O_{12}$ (see Figs. 3.5(c), 3.5(d) and 3.5(f)). In order to understand what this result indicates, first of all, we focus our attention on the mode determination of obtained peaks.

Theoretical determination of magnon modes

For $LiFe_5O_8$ we observed peaks at 8.3 and 7.3 GHz, and a broad band between 5 and 6.3 GHz. These spectra should be owing to the propagation of magnon modes, so we have to determine the magnon band dispersion. The Hamiltonian in $LiFe_5O_8$ are composed of the ferromagnetic exchange interaction, the DM interaction, the dipole-dipole interaction, the magnetic anisotropic term and the Zeeman term as shown in Eq. (3.1). The effective exchange field caused by the ferromagnetic exchange interaction is $\mu_0 \lambda_{ex} k^2 M_s = 5 \times 10^{-6}$ T at $k = 2\pi/(20\ \mu\text{m})$ for $Y_3Fe_5O_{12}$

(λ_{ex} is the spin stiffness constant, $\lambda_{ex} = 3 \times 10^{-16}$ m^2, and $M_s = 1.4 \times 10^5$ A/m for $Y_3Fe_5O_{12}$ [75, 77]). Indeed, the effective exchange field for $LiFe_5O_8$ is expected to be larger but the order is the same as that for $Y_3Fe_5O_{12}$. Thus, the ferromagnetic exchange interaction can be negligible in this wave number range. For this reason, the magnon dispersion relation can be described by the sum of the k-dependent energy of the magnetostatic wave and the k-linear energy dispersion derived from the DM interaction in this wave number region[78]. While the non-reciprocity is caused by the small DM interaction as discussed later, the spectral shape is largely determined by the dominant magnetostatic wave. From the calculation in Appendix A.2 and the experimental data, we can find that the theoretical analysis gives a good account of the experimentally observed spectrum. The comparison of frequencies is summarized in Table. 3.1. The micro-fabricated microwave antenna can induce and detect the magnon modes with $k = 0$ and $k = 2\pi/(20\ \mu\text{m})$. We assign the 8.3 GHz peak to the $k \sim 0$ mode and the broad band between 5 and 6.3 GHz to the combination of the large k modes ($k \sim 2\pi/(20\ \mu\text{m})$). The assignment of the $k = 0$ mode is consistent with the experimental result of the microwave absorption in the uniform microwave magnetic field shown in Section 3.2. Although the experimentally observed data (8.3 GHz) and the theoretical value (8.0 GHz) of excitation energy at $k = 0$ are not completely same, this slight difference comes from that the calculation does not contain the magnetic anisotropy owing to the sample shape. Here we roughly estimated the frequencies of magnetostatic waves avoiding the complex calculation to approximately determine the magnon modes. The magnetostatic backward volume wave mode at $k = 2\pi/(20\ \mu\text{m})$ depends on the index n which shows the spatial distribution along the normal direction to the substrate plane. The n is ordinary related to the shape of antenna, but the mode determination is difficult. Tentatively assuming $1 \leq n \leq 30$ modes are excited, the frequency ranges between 4.5 and 5.4 GHz. The maximum value of n was determined by the sample height 0.6 mm and the wave length of antenna 20 μm. The experimentally observed 7.3 GHz mode seems to be the standing wave mode of which the wavelength is twice the sample length. This wave number is smaller than the width of $k = 0$ peak in the antenna Fourier transformation pattern [Fig. 2.2(e)]. The standing wave of the magnon with asymmetric dispersion is nontrivial. However, the effect of asymmetry is negligible in this case because the difference

of frequency between the standing wave modes at $+k$ and $-k$ are very small. For $Y_3Fe_5O_{12}$ sample, the frequency of the magnetostatic wave at $k = 0$ is little different from that at large k. For this reason, these modes are not well separated and observed as a continuum between 4 and 6.3 GHz (see Fig. A.2(d)).

Let us now return to the discussion about microwave non-reciprocity again. Figure 3.5(e) shows that not all modes have the non-reciprocity in the chiral ferrimagnet $LiFe_5O_8$. The large non-reciprocity is observed for the large k mode whereas the $k = 0$ mode is reciprocal. When the magnetic field is reversed, the non-reciprocity is also reversed [Fig. 3.5(b)]. It is consistent with the non-reciprocity caused by the DM interaction which works as k-linear along the magnetization in the chiral ferromagnet. On the other hand, in the centrosymmetric ferrimagnet $Y_3Fe_5O_{12}$, the transmittance spectra are reciprocal in all frequency region. The result clearly shows that the measurement circuit with the centrosymmetric ferrimagnet $Y_3Fe_5O_{12}$ sample does not induce the microwave non-reciprocity. It is a piece of evidence which shows that our obtained microwave non-reciprocity is caused by the non-reciprocal magnon propagation due to the DM interaction.

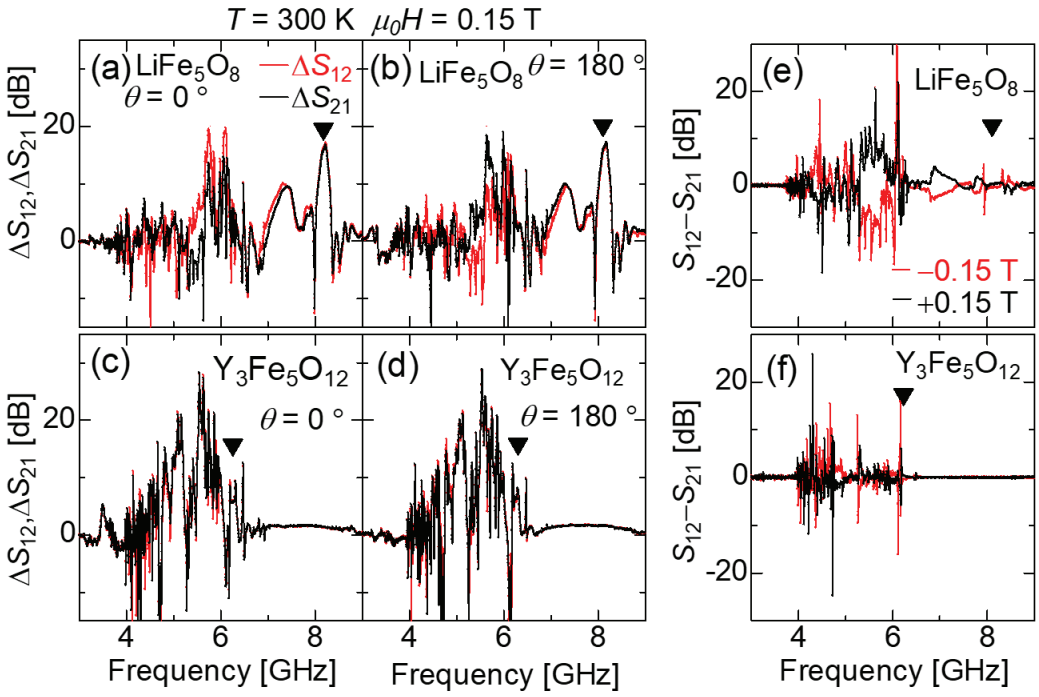

Figure 3.5: **Non-reciprocal magnon propagation and reciprocal magnon propagation in ferromagnets.** (a)-(d) Microwave transmittances owing to the magnon propagation from port 2 to port 1 (ΔS_{12}) and from port 1 to port 2 (ΔS_{21}) for (a) and (b) $LiFe_5O_8$ and (c) and (d) $Y_3Fe_5O_{12}$ are plotted as a function of the microwave frequency at room temperature. Magnitude of the magnetic field is 0.15 T and the direction of the magnetic field is indicated by θ defined in Fig. 3.3(a). The field direction $\theta = 0$ in (a) and (c) and $\theta = 180°$ in (b) and (d). FMR signals are represented by inverted triangles. (e) and (f) Non-reciprocity of microwave transmission $S_{12} - S_{21}$ of (e) $LiFe_5O_8$ and (f) $Y_3Fe_5O_{12}$ at ± 0.15 T and $\theta = 0°$. Reprinted figures from [65]. Copyright 2015, by American Physical Society.

Magnetic field directional dependence of non-reciprocity

In order to more clearly show the microscopic origin of the non-reciprocity, we plot ΔS_{12} and ΔS_{21} at various magnetic field directions around $\theta = 0$ for $LiFe_5O_8$ [Fig. 3.6(a)] and $Y_3Fe_5O_{12}$ [Fig. 3.6(b)]. For $Y_3Fe_5O_{12}$, the non-reciprocity is sensitive to the magnetic field angle θ. While at $\theta = 0$ the transmittance is reciprocal, with increasing θ, it gradually becomes non-reciprocal. It reflects the breaking of

Table 3.1: Comparison of magnon frequencies with various k determined by experimental data and theoretical analysis for $LiFe_5O_8$.

	Experiment	Theory
$k = 0$ mode	8.3 GHz	8.0 GHz
Standing	7.3 GHz	7.0 GHz (free)-
wave mode		7.7 GHz (metallized)
Large k mode	5.0-6.3 GHz	4.5-5.4 GHz ($n = 1 - 30$)

mirror symmetry in the experimental system by applying a magnetic field with angle tilted from $\theta = 0$. The non-reciprocity is reversed when the titling direction is reversed. For $LiFe_5O_8$, a similar angle dependence of the non-reciprocity is observed at $k = 0$ mode around 8 GHz. In contrast, the non-reciprocity of the large k modes of $LiFe_5O_8$ (between 5 and 6 GHz) is rather insensitive to θ. The angular dependence of all modes of $Y_3Fe_5O_{12}$ and $k = 0$ mode of $LiFe_5O_8$ seems to be almost same from the rough estimation in Fig. 3.6.

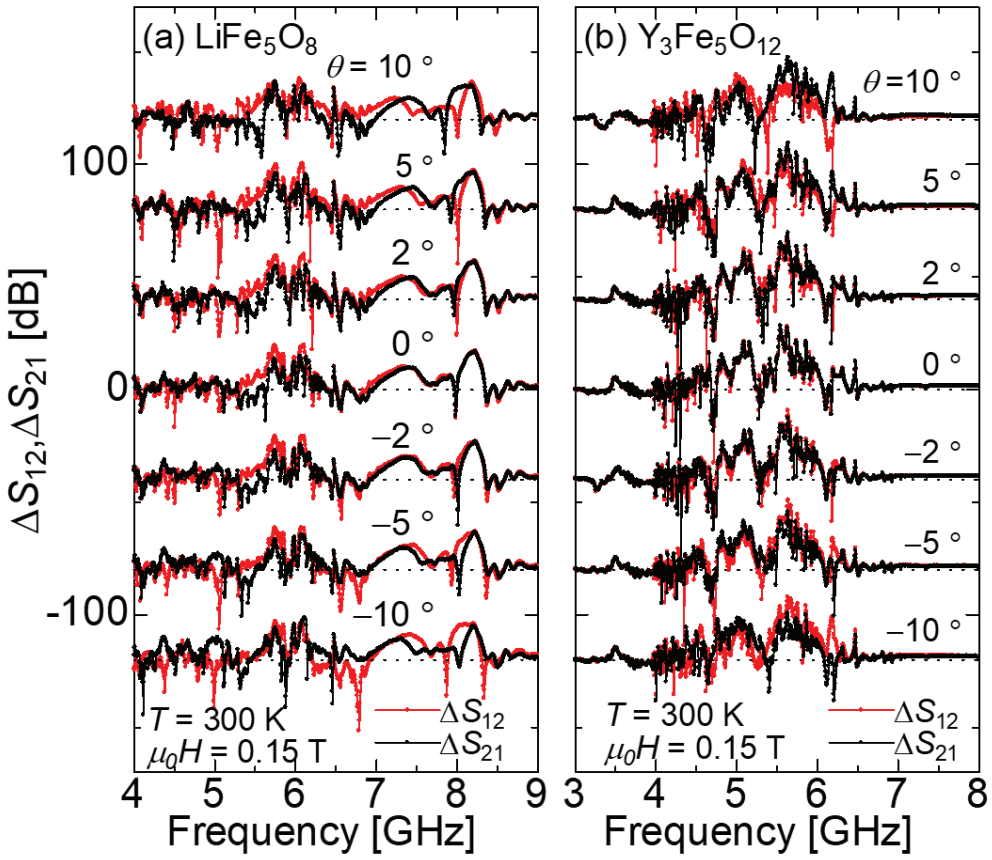

Figure 3.6: **Magnetic field directional dependence of magnon propagation.** (a) and (b) angular dependence of ΔS_{12} and ΔS_{21} for (a) $LiFe_5O_8$ and (b) $Y_3Fe_5O_{12}$ at 0.15 T at room temperature. Reprinted figures from [65]. Copyright 2015, by American Physical Society.

To discuss the angular dependence more quantitatively, we plot as a function of θ the integrated intensities of the non-reciprocity

$$\Delta I_{12} = \int (S_{12} - S_{21}) df,$$

for the large k modes of $LiFe_5O_8$ and $Y_3Fe_5O_{12}$ in Fig. 3.7, here f is the microwave frequency. The integrated intervals are $5 \leq f \leq 6$ GHz for $LiFe_5O_8$ and $4.3 \leq f \leq 5.3$ GHz for $Y_3Fe_5O_{12}$. The ΔI_{12} for $Y_3Fe_5O_{12}$ is negligible at $\theta = 0$ and increases linearly with θ. This character of the non-reciprocity can be described by the magnetostatic surface wave mode (Damon-Eshbach mode). The Damon-Eshbach wave non-reciprocally propagates perpendicular to the magnetization, which depends on the boundary condition of top and bottom surfaces.

In principle, the both non-reciprocity for $Y_3Fe_5O_{12}$ and $LiFe_5O_8$ should contain the non-reciprocity caused by the Damon-Eshbach mode. On the other hand, the non-reciprocity derived from the asymmetric band dispersion originating from the DM interaction is expected to show the maximum around $\theta = 0$ and decrease with increasing or decreasing θ. Based on the above consideration, the θ dependence of ΔI_{12} for $LiFe_5O_8$ is explained by the combination of the DM interaction and the Damon-Eshbach mode. In conclusion, the origin of the large non-reciprocity at $\theta = 0$ for $LiFe_5O_8$ is ascribed to the DM interaction caused by the lack of inversion symmetry in this material.

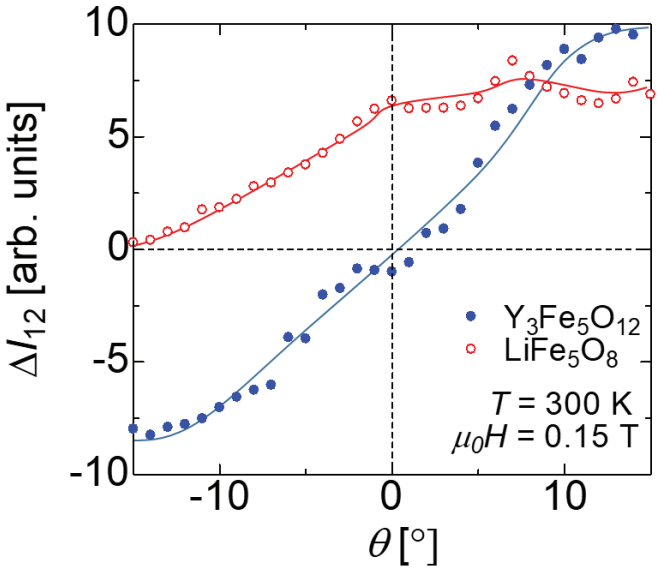

Figure 3.7: **Magnetic field directional dependence of non-reciprocity.** Integrated intensities of non-reciprocity ΔI_{12} for $LiFe_5O_8$ (open circle) and $Y_3Fe_5O_{12}$ (closed circle) are plotted as a function of the angle of the magnetic field. The solid lines are merely guides to eyes. Reprinted figures from [65]. Copyright 2015, by American Physical Society.

Lastly, the magnitude of the DM interaction will be examined by using the experimental result. According to the paper by Cortés-Ortuño and Landeros[78], the magnon band dispersion in the presence of the DM interaction is a simple summation of the symmetric dispersion of the magnetostatic wave and k-linear dispersion $2DSak$ if the ferromagnetic exchange interaction is neglected[55]. In our experiment [Fig. 3.5], the difference of the average frequency of large k modes

between ΔS_{12} and ΔS_{21} is $\sim$0.1 GHz, which corresponds to $DS \sim 0.4$ meV. We roughly estimate the ferromagnetic exchange interaction constant $J \sim 0.1$ eV from the transition temperature. From these values, we deduce D/J is order of $10^{-2} - 10^{-3}$, which is within the expected range for transition metal oxides.

3.4 Summary

In conclusion, we observed the non-reciprocal magnon propagation in a bulk chiral ferromagnet $LiFe_5O_8$ by using the micro-fabricated microwave antennae. We clearly showed that our newly observed magnon non-reciprocity has different magnetic field dependence from the classical magnon non-reciprocity owing to the DEM. This magnon non-reciprocity is consistent with the asymmetric band effect caused by the DM interaction in the IFMS of chiral materials. This result indicates the potentials of the magnon non-reciprocity caused by the bulk crystal structure and of the observation method by the micro-fabricated microwave antenna. In fact, after our report[65], other groups also reported the non-reciprocal magnon propagation in the IFMS of the other chiral materials by using the similar micro-fabricated microwave antennae[79, 80] and by using the neutron scattering[81], and other groups reported the non-reciprocal magnon propagation in thin film by using the micro-fabricated microwave antennae[82, 83]. In this way the concern with the magnon non-reciprocity owing to the relativistic asymmetric band has been growing.

Chapter 4

Magnetoelectrical control of non-reciprocal microwave propagation in a multiferroic helimagnet

The control of physical properties by external fields is essential in many contemporary technologies. For instance, optical phenomena caused by the electric field, such as electroluminescence and electrochromism, are useful for the display and other technologies. Microwave non-reciprocity has been utilized for the isolator from long ago, so it is also important phenomenon for application. However the external field control of the conventional microwave isolator is difficult in principle. Thus the non-reciprocal response owing to different principle is required. Microwave non-reciprocity was previously observed in a chiral magnet, whereas the non-reciprocity originated in the crystal chirality so it is difficult to control the non-reciprocity by electric field[42]. In this chapter, we suggest it as one solution to use the multiferroic helimagnet $Ba_2Mg_2Fe_{12}O_{22}$ that has magnon excitation in the microwave region and the polarization controllable by the poling electric field.

Recently, the controllable optical non-reciprocity has been reported for magnon excitation in the terahertz region in high magnetic fields of $3 \leq \mu_0 H \leq 7$ T[39], which is ascribed to the toroidal magnon mode. Here we show controllable non-reciprocity in ubiquitous frequency (10-15 GHz) and magnetic field (160 mT)

ranges in the multiferroic helimagnet $Ba_2Mg_2Fe_{12}O_{22}$. This approach offers a new avenue for the electrical control of microwave properties.

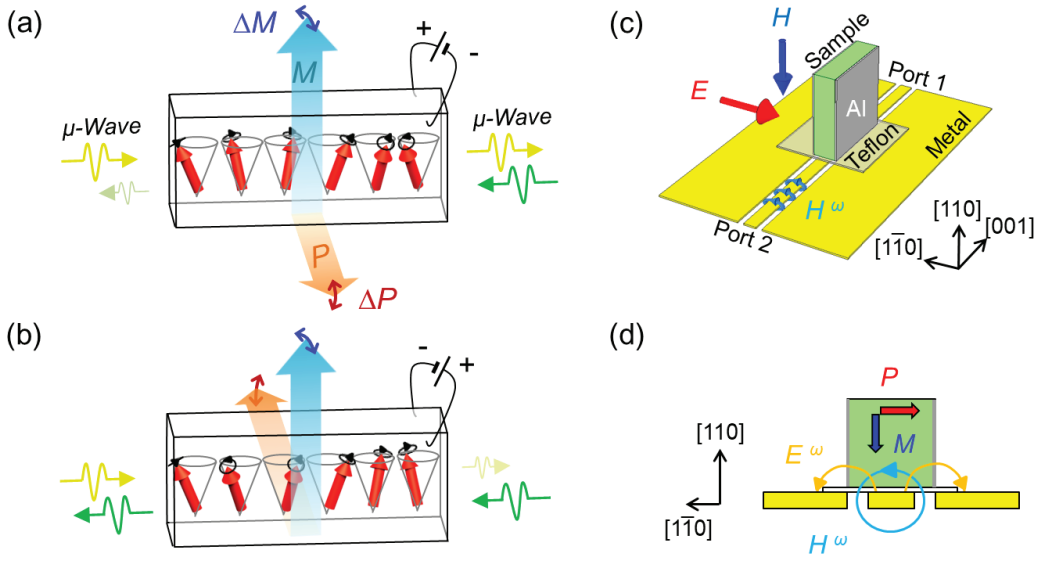

Figure 4.1: **Electrical control of non-reciprocal microwave transmission.** (a),(b) Sketch of non-reciprocal microwave transmission in ferroelectric helimagnets. The strong magnetoelectric coupling of a toroidal magnon in the transverse conical magnetic state provides the microwave non-reciprocity, which is the difference in the refractive indices between oppositely propagating microwaves. The microwave non-reciprocity as well as spin helicity can be controlled by the electric field. (c) Experimental setup of the microwave measurement. (d) Cross-section view of the (001) plane and the alternating magnetic field H^{ω} and electric field E^{ω} of microwaves in the experimental setup. Reprinted figures from [84]. Copyright ©2017, Rights Managed by Nature Publishing Group.

4.1 Fundamental properties

$Ba_2Mg_2Fe_{12}O_{22}$ is a ferrite with hexagonal structure, which is denoted as hexaferrite. Hexaferrite has six types depending on their chemical formula. Especially $Ba_2Mg_2Fe_{12}O_{22}$ is classified into the Y-type hexaferrite $(Ba,Sr)_2Me_2Fe_{12}O_{22}$ where Me means divalent metal ion[85]. The Y-type hexaferrite has the long period of helical spin structure and small magnetic anisotropy. Therefore it is expected that

the Y-type hexaferrite has the magnon excitation in microwave region. Indeed, other materials of hexaferrite family show the magnetoelectric effects above room temperature[85].

The crystal structure of $Ba_2Mg_2Fe_{12}O_{22}$ is composed to two types of alternately stacked blocks denoted as S and L blocks as shown Fig. 4.2(a). The magnetic moments of Fe ions are ferrimagnetically ordered within each block. As a result, the S and L blocks have small and large net magnetic moments, respectively. Figure 4.2(b) indicates the magnetization curve as a function of magnetic field perpendicular to the [001] axis at 6 K for $Ba_2Mg_2Fe_{12}O_{22}$. The dimensions of the sample were $1.1 \times 1. \times 0.3$ mm^3. The largest plane was perpendicular to the $[1\bar{1}0]$ direction, and the two longer sides were parallel to the [110] and [001] directions. Below 190 K, the magnetic moments of S and L blocks showed the conical magnetic orderings where the wave vector of spin structure was $\mathbf{q}_0 = (0, 0, 0.59)$[86, 87]. Thus $Ba_2Mg_2Fe_{12}O_{22}$ has a spontaneous magnetization. Figure 4.2(b) shows that the magnetization curve has several kinks reflecting magneto structural transitions which are indicated by inverted triangles. The helical plane is parallel to the [001] axis at zero magnetic field, whereas it was slanted and a spontaneous electric polarization is induced parallel to the $[1\bar{1}0]$ axis in a small magnetic field along the [110] axis while maintaining $\mathbf{q}_0 = (0, 0, 0.59)$. The ferroelectricity is caused by the spin current mechanism[67]. When the magnetic field was increased furthermore, the helical plane became perpendicular to the [110] axis, and a transverse conical state with $\mathbf{q}_0 = (0, 0, 3/4)$ appeared around 60 mT. Moreover a transverse conical state with $\mathbf{q}_0 = (0, 0, 3/2)$ became dominant above 200 mT[87]. Figure 4.2(a) shows the magnetic structure in the $\mathbf{q}_0 = (0, 0, 3/4)$ state. The phase transitions between helimagnetic structures are first-order transitions, and phase coexistence is observed around the phase boundaries. In particular, there is the $\mathbf{q}_0 = (0, 0, 3/2)$ state over the wide range of magnetic field indicated as shown in Fig. 4.2(b). The magnetic structure of $\mathbf{q}_0 = (0, 0, 3/2)$ state slightly changes around 200 mT[87]. Above 4.5 T, all the magnetic moments are forced to be ferrimagnetically ordered and the ferroelectricity is quenched. The spontaneous electric polarization was obtained by the integration of measured displacement currents. In order to increase the electric polarization, we utilized the poling procedure in a manner to a previous study[67]. After cooling the sample to 50 K without external fields, the electric

field was applied along [1$\bar{1}$0], and then the magnetic field as large as 5 T was applied parallel to [110]. Next, the magnetic field was decreased to 1 T, followed by cooling to 6 K. Finally, the electric field was removed. The displacement current was measured while sweeping the magnetic field. The obtained polarization curves are plotted as a function of magnetic field with several poling electric fields as shown in Fig. 4.3. Figure 4.3 indicates the amplitude of polarization is controlled and the sign of polarization is also reversed by the poling field.

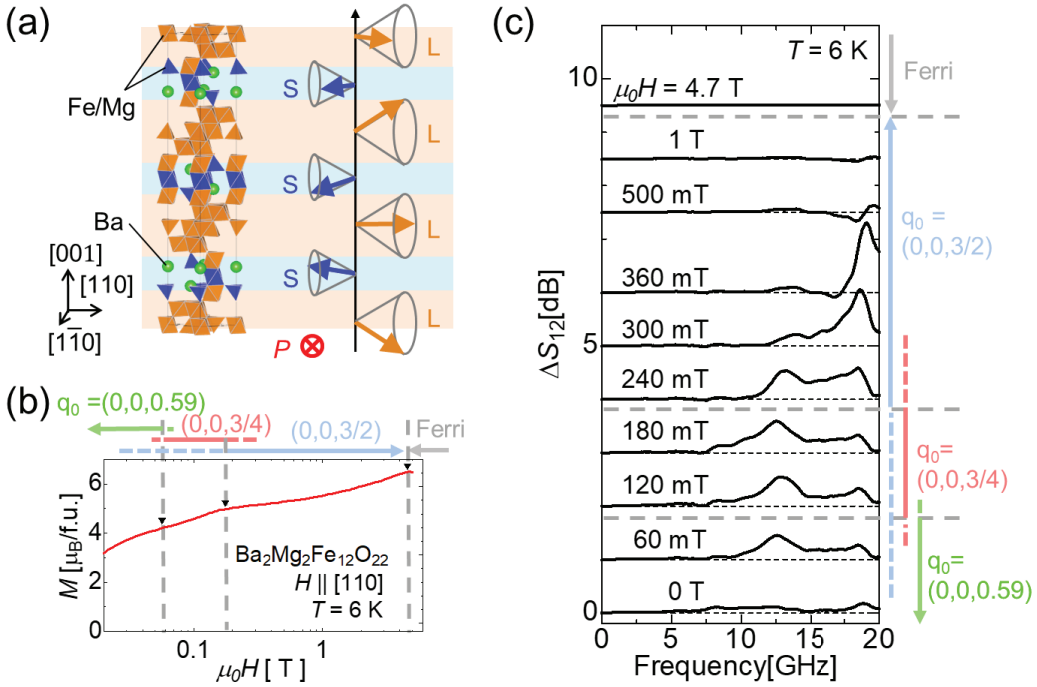

Figure 4.2: **Crystal structure and magnetic properties of $Ba_2Mg_2Fe_{12}O_{22}$.** (a) Crystal structure of $Ba_2Mg_2Fe_{12}O_{22}$ and the magnetic structure in the $\mathbf{q}_0 = (0, 0, 3/4)$ state, where the magnetoelectric control of the microwave nonreciprocity is demonstrated . (b) Magnetization curve of $Ba_2Mg_2Fe_{12}O_{22}$ at 6 K with the magnetic field along [110]. (c) Microwave absorption spectra ΔS_{12} obtained in the experimental setup [Fig. 4.1(c)] in several magnetic fields along [110] at 6K. Reprinted figures from [84]. Copyright ©2017, Rights Managed by Nature Publishing Group.

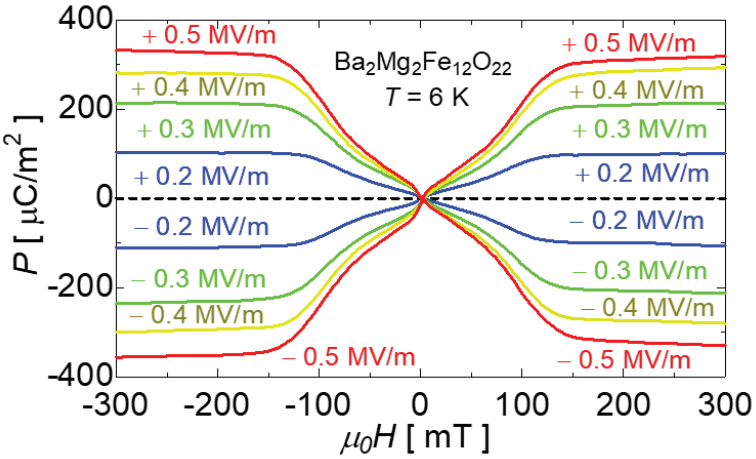

Figure 4.3: **Electric polarization of $Ba_2Mg_2Fe_{12}O_{22}$.** The spontaneous electric polarization was obtained by the measurement of displacement currents with several poling electric fields.

4.2 Magnetic field dependence of microwave absorption via magnon excitation

We measured the microwave absorption through the $Ba_2Mg_2Fe_{12}O_{22}$ sample in the experimental setup as shown in Fig. 4.1(c). The aluminum electrodes were attached to the largest sample planes for applying the electric field. The width of the strip line was 0.2 mm, and the gap between the slot line and ground planes was 0.05 mm. The $Ba_2Mg_2Fe_{12}O_{22}$ sample was placed on the CPW where the [001] direction was parallel to the wave vector of the microwave. A Teflon sheet with a thickness of 20 μm was inserted between the sample and waveguide to electrically protect the device. The spatial distribution of the magnetization and polarization of the sample and the microwave electric and magnetic fields are shown in Fig. 4.1(d). Figure 4.2(c) shows ΔS_{12} spectra at various magnetic fields at 6 K. Here the microwave absorption ΔS_{12} owing to magnetic excitations is defined as $|S_{12}(5\mathrm{T})| - |S_{12}(\mu_0 H)|$, because the magnetic resonance frequency was high enough in the entire measurement range at 5 T. Microwave absorption was almost absent at zero magnetic field, whereas a small and broad peak appeared at $\sim$ 12 GHz when the magnetic field was applied along the [110] direction.

When the magnetic field was increased above the phase transition between the $\mathbf{q}_0 = (0, 0, 0.59)$ and $\mathbf{q}_0 = (0, 0, 3/4)$ states ($\simeq 60$ mT), the frequency and intensity were slightly increased. For a detailed comparison of frequency in low magnetic field, we show the details of magnetic field dependence of microwave absorption spectra in Figs. 4.4(a) and 4.4(b). The absorption peak at ~ 12 GHz disappeared and the other peak at ~ 19 GHz became larger above the phase transition between the $\mathbf{q}_0 = (0, 0, 3/4)$ and $\mathbf{q}_0 = (0, 0, 3/2)$ states ($\simeq 200$ mT). Two peaks were simultaneously observed around the phase boundary because of the phase coexistence. The high-frequency peak increased with the magnetic field and disappeared at the measurement frequency range above 500 mT. The high-frequency peak was suppressed below 200 mT, but it remained being observed with the low-frequency peak. This result indicated the phase coexistence of the $\mathbf{q}_0 = (0, 0, 3/2)$ state. We demonstrated the control of microwave non-reciprocity mainly for the low-frequency peak in the $\mathbf{q}_0 = (0, 0, 3/4)$ state, because the measurement sensitivity in the frequency range of 9-14 GHz was better than that in the high-frequency region in our experimental setup.

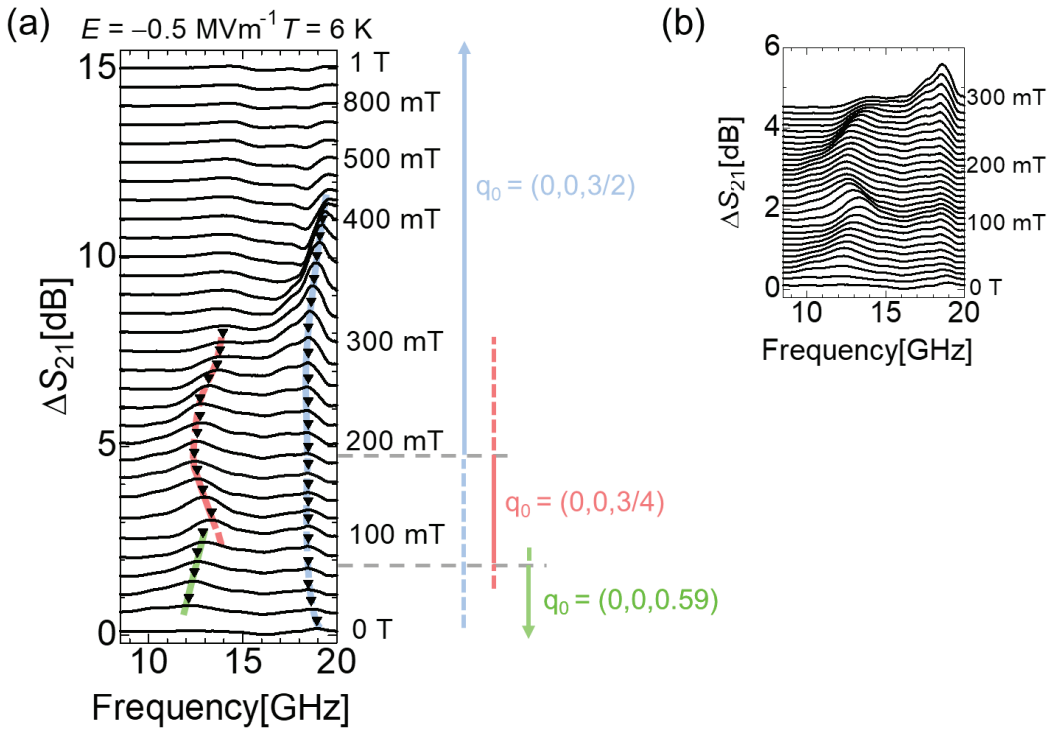

Figure 4.4: **Details of magnetic field dependence of microwave absorption spectra.** (a) Data from 0 to 1 T measured at 6 K. The inverted triangles indicates the absorption peaks and the solid lines are merely guides for the eyes. (b) More detailed data in the low magnetic field region. Reprinted figures from [84]. Copyright ©2017, Rights Managed by Nature Publishing Group.

4.3 Magnetoelectrical control of non-reciprocal microwave absorption

Figure 4.5 shows the magnetoelectrical control of non-reciprocal microwave absorption. The microwave absorption with the opposite wave vector ΔS_{21} was obtained by a similar procedure to ΔS_{12}. We performed the poling procedure to fix the spin helicity and control the sign of the polarization. After the poling procedure, we set the magnetic field at measured points, then we measured ΔS_{12} and ΔS_{21} at 6 K in the magnetic field without the electric field. Figures 4.5(a) and 4.5(c) show the microwave absorption spectra measured after the poling procedure with the electric field $E = +0.5$ MVm^{-1}, and Figs. 4.5(b) and 4.5(d) show the spec-

tra measured after the poling procedure with $E = -0.5$ MVm^{-1}. The measured magnetic field $\mu_0 H$ was +160 mT for Figs. 4.5(a),(c) and −160 mT for Figs. 4.5(b),(d). It is clear that the absorption spectra are different for each case. This result indicates the microwave non-reciprocity. The non-reciprocity was reversed by reverse of either E or H, but the non-reciprocity was unchanged by the reverse of the both fields.

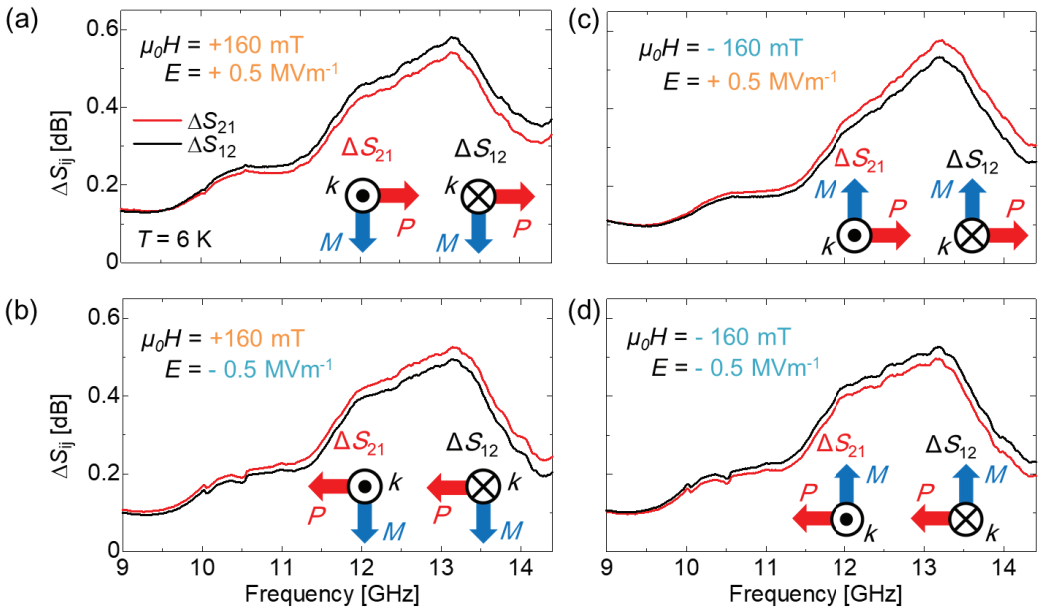

Figure 4.5: **Magnetoelectrical control of microwave non-reciprocity.** (a)-(d) Microwave absorption spectra $\Delta S_{12}, \Delta S_{21}$ at 6 K in ±160 mT (+160 mT in (a),(b) and −160 mT in (c),(d)). The poling electric fields were $E = \pm 0.5$ MVm^{-1} (+0.5 MVm^{-1} in (a),(c) and −0.5 MVm^{-1} in (b),(d)). Inset illustrates the directional relation between the polarization, magnetization and wave vectors k for ΔS_{12} and ΔS_{21} measurements. Reprinted figures from [84]. Copyright ©2017, Rights Managed by Nature Publishing Group.

We will now examine the effect of an external field more closely. For this purpose, we investigated the poling electric field dependence of microwave non-reciprocity $\Delta S_{12} - \Delta S_{21}$ at $\mu_0 H = 160$ mT and the magnetic field dependence by using the poling fields $E = \pm 0.5$ MVm^{-1}. The results are shown in Figs. 4.6(a) and 4.6(b), respectively. The sign of the non-reciprocity depended on the sign of the electric field E and the magnitude of the non-reciprocity monotonously

increased with E. When the magnetic field was increased, the frequency of the non-reciprocity was also increased, corresponding approximately to the increase of the absorption peak frequency (see also Fig. 4.7). Figure 4.6(c) indicates the integrated intensity of the non-reciprocity I_{12} between 9 and 14.4 GHz at $\mu_0 H = \pm 160$ mT as a function of E. The sign of I_{12} depended on the sign of EH and the magnitude of I_{12} gradually increased in the low-E region and tended to be saturated at ~ 0.5 MVm^{-1}. A similar E dependence was seen in the polarization results. It was clearly shown by plotting the polarization of Fig. 4.3 into Fig. 4.6(c) as a function of E. Thus, these field dependences are dominated by the ferroelectric domain population.

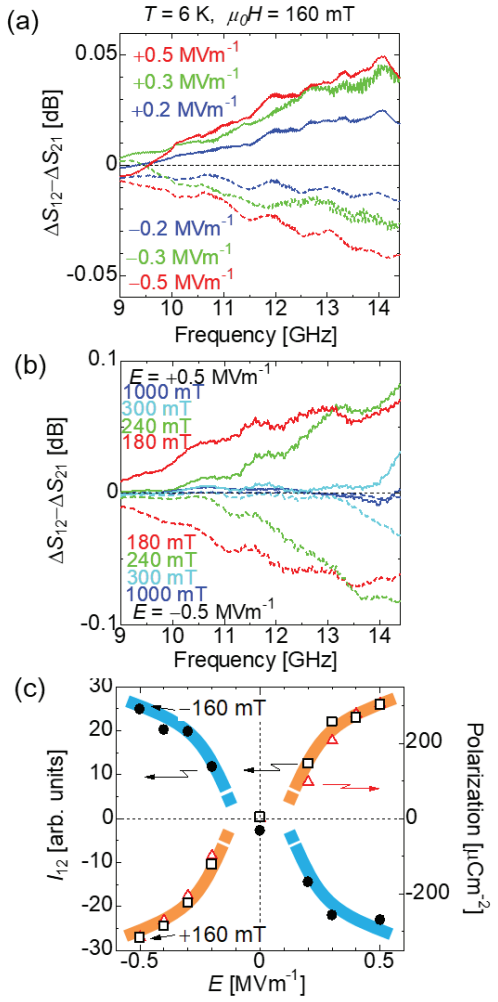

Figure 4.6: **Electric field and magnetic field dependences of microwave non-reciprocity.** (a) Poling field dependence of microwave non-reciprocities, $\Delta S_{12} - \Delta S_{21}$, at ± 160 mT at 6 K. The data of positive poling fields are plotted as solid lines and the data of negative poling fields are plotted as dashed lines. (b) Magnetic field dependence of microwave non-reciprocities is plotted in the same frequency range to (a) after electric field poling $E = +0.5$ MVm^{-1} (Solid lines) and $E = -0.5$ MVm^{-1} (dashed lines). (c) Integrated intensities of the microwave non-reciprocity I_{12} at ± 160 mT (open squares) and -160 mT (closed circles) are plotted as a function of the poling electric field E. The polarization at $+160$ mT (open triangles), which was obtained by Fig. 4.3, is also plotted as a function of E for comparison. The solid lines are merely guides for the eyes. Reprinted figures from [84]. Copyright ©2017, Rights Managed by Nature Publishing Group.

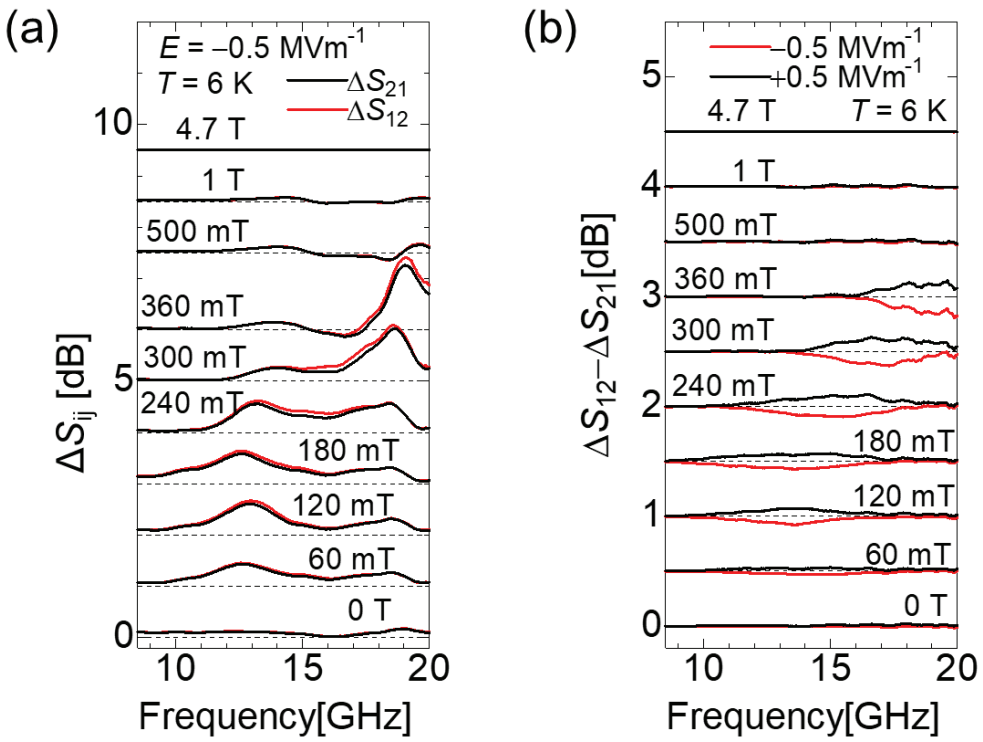

Figure 4.7: **Details of magnetic field dependence of microwave non-reciprocity.** (a) Magnetic field dependence of microwave absorption spectra $\Delta S_{12}, \Delta S_{21}$ at 6 K measured after the poling with $E = -0.5$ MVm^{-1}. (b) Magnetic field dependence of microwave non-reciprocities $\Delta S_{12} - \Delta S_{21}$ at 6 K measured after the poling with $E = \pm 0.5$ MVm^{-1}. Reprinted figures from [84]. Copyright ©2017, Rights Managed by Nature Publishing Group.

Discussion

We observed controllable microwave non-reciprocity for the lowest-energy magnetic resonance modes in the transverse conical states. The obtained non-reciprocity cannot be ascribed to the effect of the magnetic dipole-dipole interaction, because the non-reciprocity should not be changed by the poling electric field in the case of the magnetic dipole-dipole interaction. As mentioned in Section 1.2, the lowest-energy magnon excitation in the transverse conical state, which is the toroidal magnon mode, provides the large non-reciprocity in the wave vector parallel to $\mathbf{P} \times \mathbf{M}$ for the Voigt geometry. This is quite consistent with the obtained result. Similar magnon modes were previously reported at large magnetic fields in the

terahertz region for perovskite $R\mathrm{MnO_3}$ [39, 40], whereas we have observed it in this thesis at a low magnetic field in the microwave region. $R\mathrm{MnO_3}$ and $\mathrm{Ba_2Mg_2Fe_{12}O_{22}}$ are both helimagnets, but the period and the magnetic anisotropy are largely different. For $\mathrm{TbMnO_3}$, which is a typical material of perovskite helimagnets, the period is 2 nm, and the magnetic anisotropy constant $\mathrm{K_1}$ is 6×10^7 erg $\mathrm{cm^{-3}}$, whereas for $\mathrm{Ba_2Mg_2Fe_{12}O_{22}}$, the period is 23 nm and the magnetic anisotropy constant $\mathrm{K_1 + 2K_2}$ is -6×10^5 erg $\mathrm{cm^{-3}}$[88, 89, 90, 91]. The frequency difference reflects the differences in the magnetic anisotropy[92] and helical period. The magnitude of the microwave non-reciprocity in this study was as large as 6-8 %, which is smaller than that observed in the terahertz region. One of the reasons is that the intensity of pure magnetic excitation becomes relatively large, so the relative non-reciprocity becomes small in the case of the spontaneous conical state.

4.4 Summary

We demonstrated the controllable microwave non-reciprocity by using the multiferroic helimagnet $\mathrm{Ba_2Mg_2Fe_{12}O_{22}}$. We showed that the sign and amplitude of the microwave non-reciprocity can be controlled by the poling electric field. In addition, the difference of the non-reciprocity in helimagnet between the terahertz and the microwave regions was discussed. From the discussion, we found that the difference of the magnetic anisotropy and the helical period are related to the conical magnon excitation frequency and that in the low magnetic field the intensity of toroidal magnon is smaller than the intensity of conical magnon. The former indicates the index for searching the new candidates that show the controllable microwave non-reciprocity. One of the advantages of the microwave non-reciprocity is compatibility with other microwave technologies. For example, the non-reciprocity can be adequately enhanced by using a high-Q resonator. The electrical control of microwave properties has been extensively investigated for multiferroic heterostructures with the use of mechanical strain-mediated magnetoelectric coupling[93], whereas controllable microwave non-reciprocity in the transverse conical state seems to be more useful. Hence, our study indicates that the controllable microwave non-reciprocity is a new microwave functionality and has a large potential for practical applications.

Chapter 5

Non-reciprocal microwave propagation in a multiferroic antiferromagnet

Antiferromagnetic spintronics has been attracting much attention, because it does not have large magnetization and appropriate for nano-devices. In contrast to the magnon excitations in magnets with the finite magnetization, such as ferromagnets and conical magnets, the antiferromagnetic magnon excitation tends to need high frequency and high field for observation. In order to scrutinize the magnetic field dependent antiferromagnetic magnon modes and their NDD, here we chose $Ba_2MnGe_2O_7$, which has the low Néel temperature T_N and small anisotropy, as a sample and have investigated the magnon excitations in the microwave region.

5.1 Fundamental properties

Multiferroic properties

$Ba_2XGe_2O_7$ (X = Mn, Co) are non-centrosymmetric antiferromagnets (Space group: $P\bar{4}2_1m$)[68]. Figures 5.1(a) and 5.1(b) show the crystal and magnetic structures, respectively. $Ba_2XGe_2O_7$ are the easy-plane-type antiferromagnets and weak ferromagnetic owing to the DM interaction. While $Ba_2CoGe_2O_7$ is ferromagnetically ordered along [001] direction below 7 K[94], in $Ba_2MnGe_2O_7$ the net magnetization in one layer is opposite to those of the neighboring layers below 4 K[95]. Hence $Ba_2CoGe_2O_7$ has the net magnetization but $Ba_2MnGe_2O_7$ does not have in zero magnetic field. $Ba_2XGe_2O_7$ has the chiral magnetic point group ($m'm2'$) or the polar magnetic point group ($22'2'$) in the magnetic field [Fig. 5.2]. $Ba_2MnGe_2O_7$ has the electric polarization as shown in Fig. 5.3(c)[68]. This multiferroic property is explained by the metal ligand hybridization mechanism.

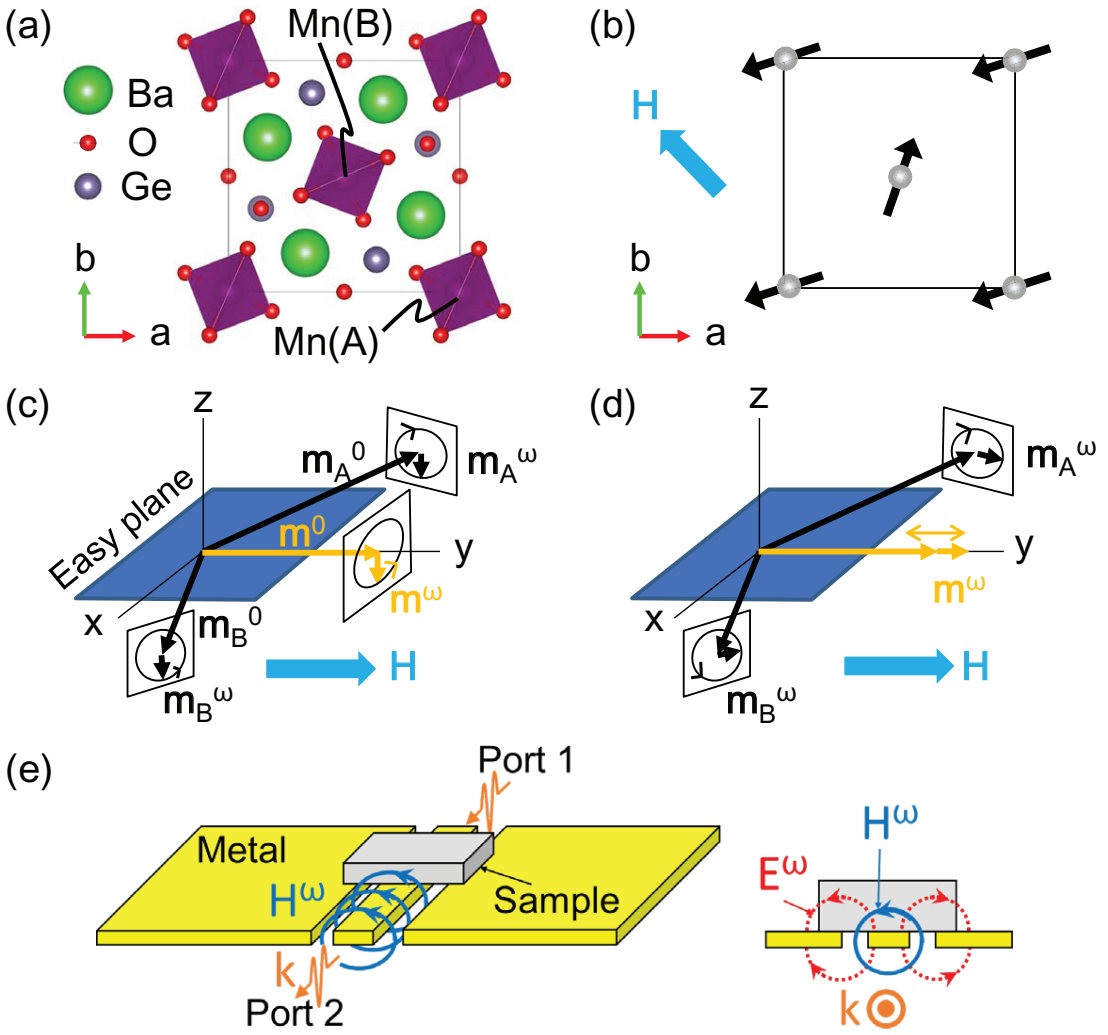

Figure 5.1: **Magnetic properties of $Ba_2MnGe_2O_7$.** (a) Crystal structure of $Ba_2MnGe_2O_7$. The two Mn ions are denoted as Mn(A) and Mn(B). (b) Magnetic structure in the magnetic field along the $[\bar{1}10]$ direction of $Ba_2MnGe_2O_7$. (c),(d) Illustrations of two magnon modes ((c) mode 1, (d) mode 2) in the in-plane magnetic field for an easy-plane antiferromagnet. $\mathbf{m}_A^0$, $\mathbf{m}_A^\omega$, $\mathbf{m}_B^0$, and $\mathbf{m}_B^\omega$ are the static and dynamical magnetic moments at the sublattice A and sublattice B, respectively. $\mathbf{m}^0$ and $\mathbf{m}^\omega$ are the static and dynamical parts of total magnetic moment, respectively. (e) Sketch of experimental setup. The sample is put at the center of coplanar wave guide. The microwave propagates along the center signal line. The alternating magnetic field $\mathbf{H}^\omega$ and the alternating electric field $\mathbf{E}^\omega$ are perpendicular to the microwave wave vector $\mathbf{k}$.

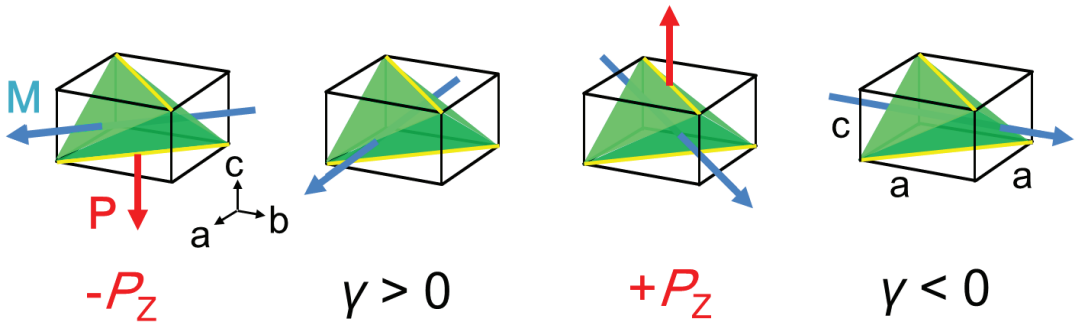

Figure 5.2: **Spatial inversion symmetry breaking depending on magnetization in $Ba_2MnGe_2O_7$.** Effective magnetizations parallel to [100] and [110] directions break the spatial inversion symmetry as $22'2'$ and $m'm2'$, respectively. $Ba_2MnGe_2O_7$ has the polarization P_z and the chirality γ.

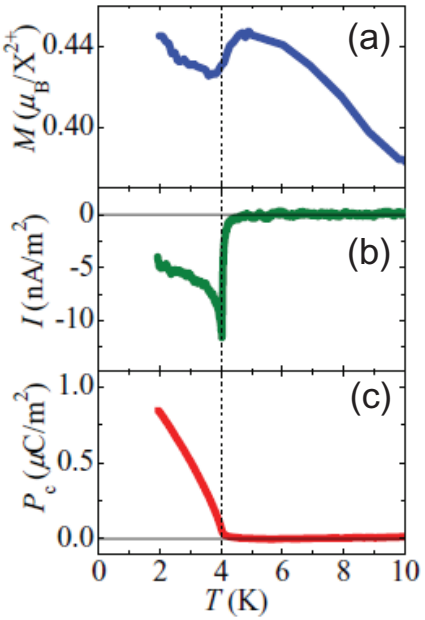

Figure 5.3: **Magnetization and Polarization of $Ba_2MnGe_2O_7$.** (a)-(c) The observed (a) magnetization, (b) the displacement current, and (c) the polarization of $Ba_2MnGe_2O_7$ measured in the magnetic field (1 T) applied along the [110] direction[68]. Reprinted figure from [68]. Copyright 2012 by the American Physical Society.

Magnetic excitations

Magnetic excitations of $Ba_2CoGe_2O_7$ have been observed in the neutron scattering[94] and the terahertz light measurement[96]. In the magnetic field along the magnetic easy plane of $Ba_2CoGe_2O_7$, the lowest energy mode and some gap modes were observed. The lowest energy mode is the precession mode of spins of each sublattice with same phases and corresponds to the quasi Nambu-Goldstone mode in zero field. It is called ω_1 mode [Fig. 5.1(c)]. In contrast, the lowest energy mode of gap modes is the precession mode of spins of each sublattice with phase shifted by π, where the effective magnetic moment is stretching. This mode is called ω_2 mode [Fig. 5.1(d)]. Magnon modes specific to antiferromagnets, such as ω_2 mode, has the gap energy that depends on the exchange interaction and magnetic anisotropy[97]. Almost antiferromagnets have gap magnon modes in the terahertz region.

In $Ba_2MnGe_2O_7$, Mn ion has a spin $S = 5/2$ with no orbital degrees of freedom. For this reason, it is likely that $Ba_2MnGe_2O_7$ has weaker magnetic anisotropy than that of $Ba_2CoGe_2O_7$. The Néel temperature is T_N =4 K so that the exchange interaction constant J between the nearest neighbor Mn ions is also small[95]. Therefore we expected that $Ba_2MnGe_2O_7$ has the antiferromagnetic magnon excitations in the microwave region. On the other hand, for $Ba_2CoGe_2O_7$, NDD of the terahertz light has been reported in ω_1 and ω_2 modes in large magnetic fields (4-12 T)[37, 25, 26]. In the microwave region, NDD has been only observed via the excitation of conical magnetic[42, 29, 84] and ferromagnetic[42, 28, 29] and paramagnetic magnon modes[30]. The observation of the antiferromagnetic magnon modes of $Ba_2MnGe_2O_7$ in the microwave region indicates the microwave non-reciprocity owing to the antiferromagnetic magnon excitations in the low magnetic field ($\sim$ 100 mT). Here we measured the microwave response of $Ba_2MnGe_2O_7$ in the range of 10 MHz - 40 GHz at the antiferromagnetic state (T = 1.8 K) and we observed the two antiferromagnetic magnon excitations within the microwave range. Indeed, we observed the non-reciprocal microwave response, the MCh and OME effects, of each mode.

5.2 Experimental details

We prepared single crystals of $Ba_2MnGe_2O_7$ by using the Floating zone method[68]. We measured the microwave absorption on the coplanar waveguide, which was designed so that the characteristic impedance coincides 50 Ω. The width of the signal line was 0.2 mm, and the gap between the signal line and ground planes was 0.05 mm. The single crystal was put on the center of waveguide and measured the microwave absorption in the external magnetic field (**H**). The microwave absorption spectra ΔS_{12} was deduced by the difference of $S_{12}(H)$ from the zero field value. Here, S_{12} is the transmittance coefficient from port 2 to port 1 (The two ports are connected to the two terminals of waveguide). In this case, we used the zero field data as the background because the present antiferromagnetic samples show negligible microwave absorption at $H = 0$. ΔS_{21} is the absorption of microwave for the wave vector opposite to the case of ΔS_{12}. The alternating magnetic field of microwave ($\mathbf{H}^{\omega}$) is induced in the plane perpendicular to the wave vector **k**. Hereafter, we specify which crystal axes are along **H** and perpendicular to $\mathbf{H}^{\omega}$ in order to describe the experimental geometry. All the experimental data in this paper were taken at $T = 1.8$ K.

5.3 Results and discussions

Figure 5.4(a) shows the microwave absorption spectra at various magnetic fields for $\mathbf{H} \parallel [1\bar{1}0]$ and $\mathbf{H}^{\omega} \perp [110]$. We have identified two peaks in the absorption spectra. One peak is observed in the low frequency region at a low magnetic field. The peak frequency and intensity increase with the magnetic field. This mode is denoted as ω_1 mode. The other mode is observed around 26 GHz in the low field region. The peak frequency is almost unchanged below 1 T but gradually decreases with the magnetic field above 1 T. This magnon mode is denoted as ω_2 mode. The peak frequencies are plotted as a function of magnetic field in Fig. 5.4(d). While the frequency of ω_1 mode increases linearly with the magnetic field, that of ω_2 mode gradually decreases as the magnetic field is increased. To examine the origin of these magnon modes, we measured the polarization dependence of absorption spectra. We have found that the absorption peak for ω_2 mode is absent for $\mathbf{H} \parallel$

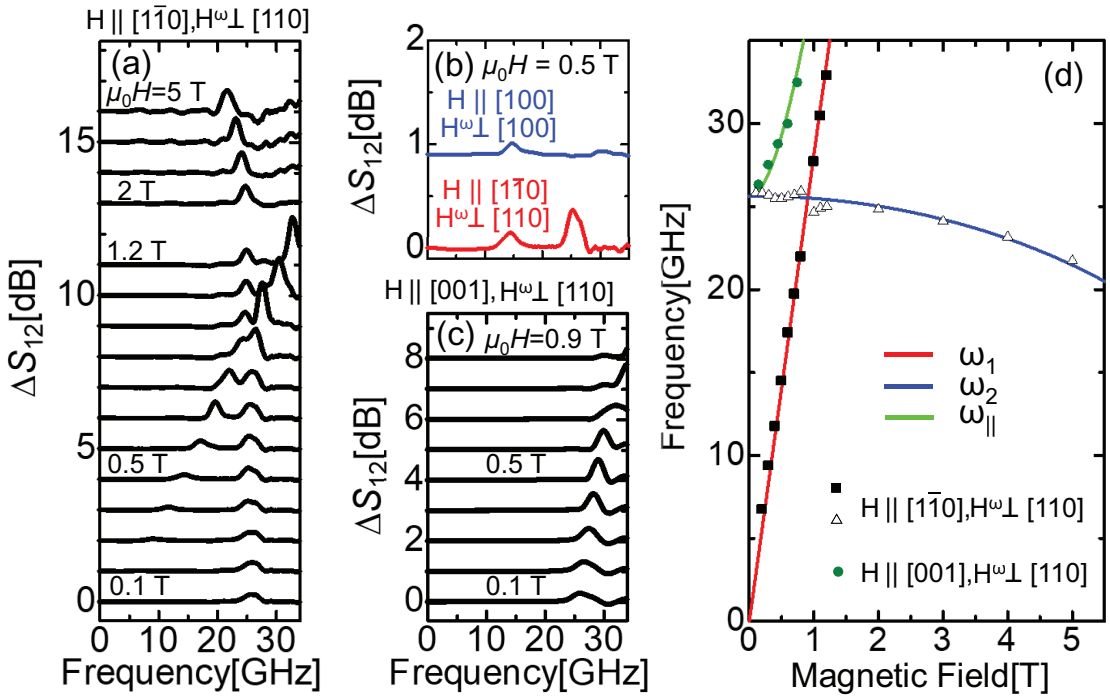

Figure 5.4: **Antiferromagnetic magnon modes.** (a) The microwave absorption spectra ΔS_{12} at various magnetic fields in the experimental geometry with $\mathbf{H} \parallel [1\bar{1}0]$ and $\mathbf{H}^{\omega} \perp [110]$. (b) Comparison of ΔS_{12} at 0.5 T in the two geometries, $\mathbf{H} \parallel [100], \mathbf{H}^{\omega} \perp [100]$ and $\mathbf{H} \parallel [1\bar{1}0]$, $\mathbf{H}^{\omega} \perp [110]$. (c) ΔS_{12} at various magnetic fields for $\mathbf{H} \parallel [001]$ and $\mathbf{H}^{\omega} \perp [110]$. (d) Experimentally observed and theoretically obtained magnon frequencies. Squares and triangles indicate the peak frequencies of experimentally observed magnon ω_1 mode and ω_2 mode for $\mathbf{H} \parallel [1\bar{1}0]$, $\mathbf{H}^{\omega} \perp [110]$, respectively, and circles the experimentally observed magnon mode for $\mathbf{H} \parallel [001]$, $\mathbf{H}^{\omega} \perp [110]$. The corresponding theoretical curves [Eqs. (5.1)-(5.3)] are plotted as solid lines.

[100] and $\mathbf{H}^{\omega} \perp [100]$ as shown in Fig. 5.4(b). This indicates the alternating magnetization in ω_2 mode is along the external static magnetic field. Actually such a polarization dependence is expected for the conventional magnon modes in easy-plane antiferromagnet in the in-plane magnetic field. Figures 5.1(c) and 5.1(d) illustrate the conventional magnon modes. The one mode is uniform oscillation of magnetic moment with keeping the relative angle of magnetic moments [Fig. 5.1(c)]. The other mode is the anti-phase oscillation of two magnetic moments in a unit cell [Fig. 5.1(d)]. The oscillation of total magnetic moment is along the external magnetic field. The ω_2 mode seems to correspond to the latter magnon modes judging from the polarization dependence while the ω_1 mode seems the former magnon mode. Theoretically, the frequencies of ω_1 mode and ω_2 mode are expressed as

$$\omega_1 = \gamma\mu_0 H\sqrt{1+\frac{H_{\rm A}}{2H_{\rm E}}}, \tag{5.1}$$

$$\omega_2 = \gamma\mu_0\sqrt{2H_{\rm E}H_{\rm A}-\frac{H_{\rm A}}{2H_{\rm E}}H^2}. \tag{5.2}$$

Here $\gamma, \mu_0, H_{\rm A}$, and $H_{\rm E}$ are the gyromagnetic ratio, the magnetic permeability in vacuum, the magnetic anisotropy field, and the exchange field, respectively. As shown in Fig. 5.4(d), these theoretical formula are quite consistent with the experimental observation. To further examine the theory-experiment correspondence, we study the magnon in the magnetic field along [001] direction. In this case, one mode is zero frequency rotation of magnetic moments around the [001] direction. Therefore, only one mode is expected in the finite frequency regime. We certainly observe only one magnon peak in this experimental geometry [Fig. 5.4(c)]. The magnetic field dependence of frequency is theoretically expressed as follow[97];

$$\omega_{\parallel} = \gamma\mu_0\sqrt{2H_{\rm E}\frac{2H_{\rm E}+H_{\rm A}}{(2H_{\rm E}-H_{\rm A})^2}H^2+2H_{\rm E}H_{\rm A}}. \tag{5.3}$$

The experimental data of peak frequency is reproduced with the same parameters as the in-plane-field case. From the fittings of experimental data to the theoretical formula, we obtained $\mu_0 H_A \simeq 0.09$ T and $\mu_0 H_E \simeq 4.67$ T, which are corresponding to the exchange interaction constant $J \simeq 27$ μeV and the single ion anisotropy $K \simeq 2$ μeV, respectively. While the estimated exchange interaction almost coincides with that estimated by the previous neutron scattering study[95], the magnitude

of magnetic anisotropy in this system was not reported previously. Reflecting the isotropic $S = 5/2$ state, the magnetic anisotropy is much smaller than the isostructural $Ba_2CoGe_2O_7$ (1.4 meV)[48, 96].

As mentioned above, microwaves are expected to show the non-reciprocity in time reversal and spatial inversion symmetries simultaneously broken systems. We tried to observe the microwave non-reciprocity in two experimental geometries. The first geometry is $\mathbf{H} \parallel \langle 100 \rangle$, $\mathbf{H}^{\omega} \perp \mathbf{H}$. In this case, only the ω_1 mode is observable. In the magnetic field along [100], the magnetic symmetry is chiral[25] and expected to show the non-reciprocity for counter-propagating microwave along the magnetic field direction. We show the microwave absorption spectra ΔS_{12} and ΔS_{21} at 0.4 T for $\mathbf{H} \parallel [100]$ in Fig. 5.5(a). We have found that ΔS_{12} and ΔS_{21} are different from each other. The difference of absorptions $\Delta S_{12} - \Delta S_{21}$ indicates the microwave non-reciprocity. It was reversed in the reversal magnetic field as shown in Fig. 5.5(b). It should be noted that the 90 degree rotation of sample around the [001] direction corresponding to the spatial inversion operation, and the chirality and microwave non-reciprocity should be reversed when $\mathbf{H} \parallel \mathbf{k} \parallel [010]$[25]. In order to discuss the effect of spatial inversion on the microwave non-reciprocity, we show the microwave non-reciprocity for $\mathbf{H} \parallel \mathbf{k} \parallel [010]$. As shown in Figs. 5.5(c) and 5.5(d), the microwave non-reciprocity is reversed by the spatial inversion. When the magnetic field is increased, the magnitude of non-reciprocity increases as shown in Fig. 5.5(e).

Let us move on to the second geometry of microwave non-reciprocity measurement, where $\mathbf{H} \parallel [1\bar{1}0]$ and $\mathbf{H}^{\omega} \perp [110]$. In this case, the sample has an electric polarization along [001], and both the ω_1 mode and the ω_1 mode are observable. Figures 5.6(a)-(c) and 5.6(d)-(f) show the microwave absorption spectra around the ω_1 mode and the ω_2 mode, respectively. One can see that the non-reciprocities in this low magnetic field are almost negligible in this experimental geometry. It should be noted that the non-reciprocity caused by the magnetic dipolar interaction[30], which is distinct from the non-reciprocity due to the material symmetry breaking, becomes dominant in the high magnetic field region above 0.5 T. The dipolar non-reciprocity was not reversed by the 90 degree rotation of sample around the [001] direction, which is equivalent to the spatial inversion.

Finally, let us compare the observed microwave non-reciprocity with the the-

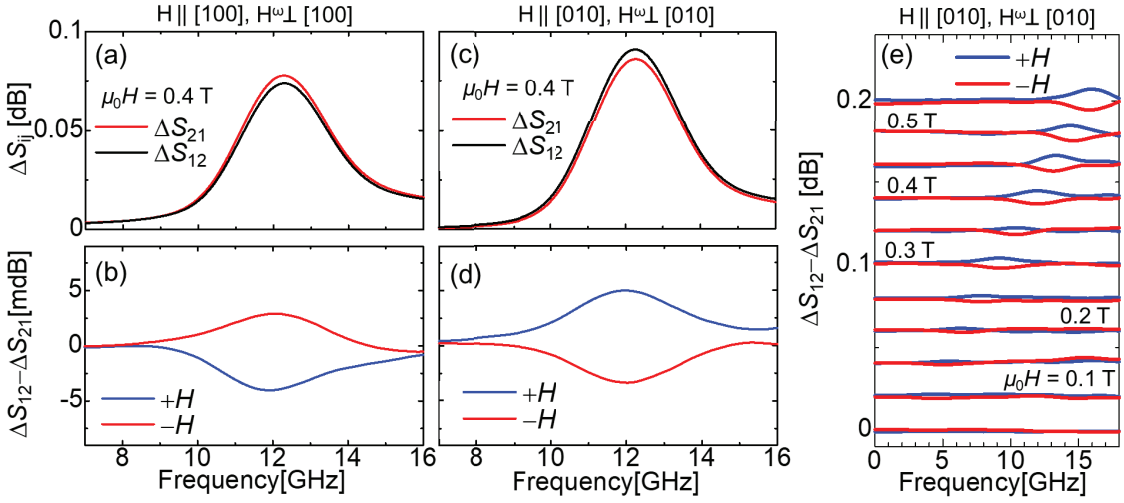

Figure 5.5: **Microwave non-reciprocity for H ∥ [100] and $\mathbf{H}^{\omega}$ ⊥ [100].** (a) Microwave absorption spectra ΔS_{12} and ΔS_{21} for **H** ∥ [100] and $\mathbf{H}^{\omega}$ ⊥ [100]. (b) Microwave non-reciprocity $\Delta S_{12} - \Delta S_{21}$ at ±0.4 T for **H** ∥ [100] and $\mathbf{H}^{\omega}$ ⊥ [100]. (c) ΔS_{12} and ΔS_{21} for **H** ∥ [010] and $\mathbf{H}^{\omega}$ ⊥ [010]. (d) $\Delta S_{12} - \Delta S_{21}$ at ±0.4 T for **H** ∥ [010] and $\mathbf{H}^{\omega}$ ⊥ [010]. (e) $\Delta S_{12} - \Delta S_{21}$ for **H** ∥ [010] and $\mathbf{H}^{\omega}$ ⊥ [010] at various positive and negative magnetic fields.

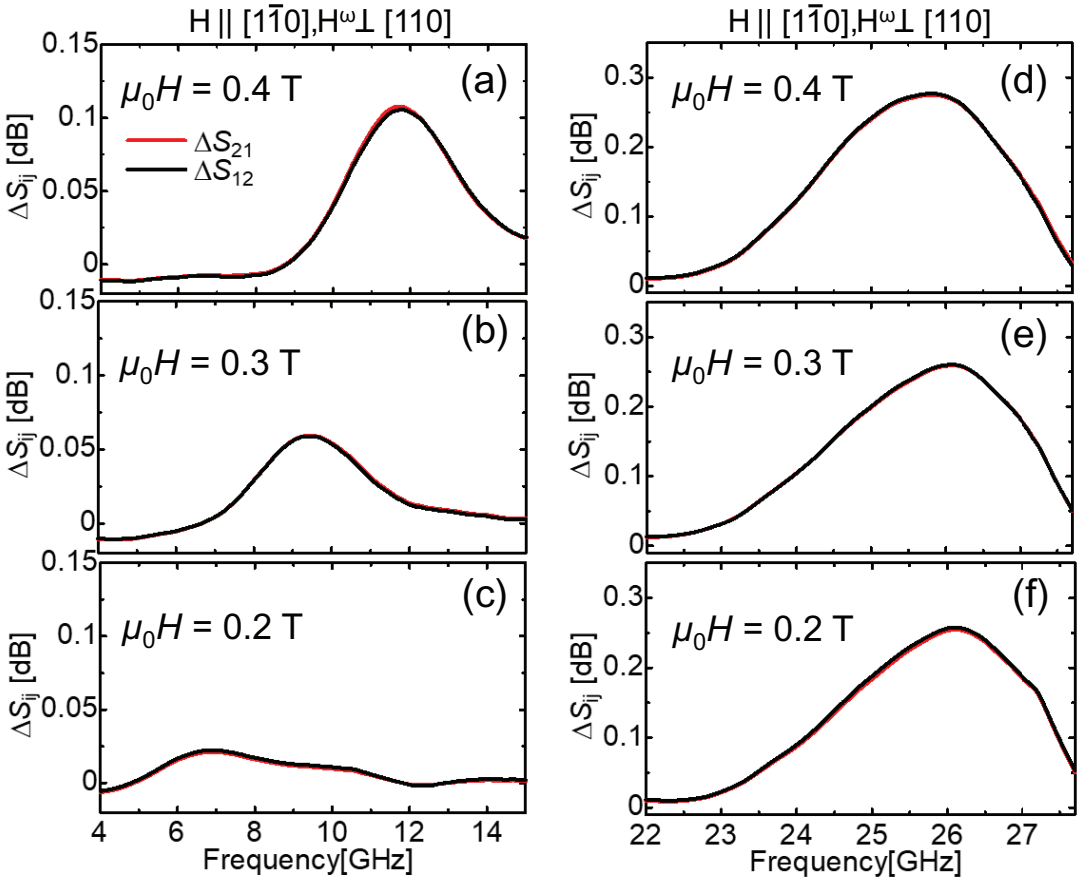

Figure 5.6: **Microwave non-reciprocity for H ∥ [1$\bar{1}$0] and H$^{\omega}$ ⊥ [110].** (a)-(f)Microwave absorption spectra ΔS_{12} and ΔS_{21} for **H** ∥ [1$\bar{1}$0] and **H**$^{\omega}$ ⊥ [110]. (a), (b), and (c) show the spectra around the frequency of ω_1 mode at 0.4 T, 0.3 T, and 0.2 T, respectively. (d), (e), and (f) around the frequency of ω_2 mode at 0.4 T, 0.3 T, and 0.2 T, respectively.

oretical calculation. Theoretically, the relative non-reciprocity for the linearly polarized microwave with $\mathbf{k} \parallel \mathbf{x}$ and $\mathbf{H}^{\omega} \parallel \mathbf{z}$, and $\mathbf{E}^{\omega} \parallel \mathbf{y}$ can be expressed as(see Appendix B)

$$\frac{\Delta S_{12} - \Delta S_{21}}{\Delta S_{12} + \Delta S_{21}} = \frac{\mathrm{Im}\left[\chi_{zy}^{me} + \chi_{yz}^{em}\right]}{2\mathrm{Im}\left[\sqrt{(1+\chi_{zz}^{mm})\left(\varepsilon_{\infty} + \chi_{yy}^{ee}\right)}\right]}, \tag{5.4}$$

where χ_{ij}^{me}, χ_{ij}^{em}, χ_{ij}^{ee}, χ_{ij}^{mm}, ε_{∞} are magnetoelectric, electromagnetic, electric, and magnetic susceptibility tensors and high frequency relative dielectric constant, respectively. According to the Kubo formula, these susceptibilities are obtained by the following relations(see Appendix B);

$$\chi_{ij}^{me} = \frac{NV}{\hbar}\sqrt{\frac{\mu_0}{\varepsilon_0}}\sum_n \frac{\langle 0\,|\Delta M_i|\,n\rangle\,\langle n\,|\Delta P_j|\,0\rangle}{\omega - \omega_n + i\delta}, \tag{5.5}$$

$$\chi_{ij}^{em} = \frac{NV}{\hbar}\sqrt{\frac{\mu_0}{\varepsilon_0}}\sum_n \frac{\langle 0\,|\Delta P_i|\,n\rangle\,\langle n\,|\Delta M_j|\,0\rangle}{\omega - \omega_n + i\delta}, \tag{5.6}$$

$$\chi_{ij}^{mm} = \frac{NV}{\hbar}\mu_0\sum_n \frac{\langle 0\,|\Delta M_i|\,n\rangle\,\langle n\,|\Delta M_j|\,0\rangle}{\omega - \omega_n + i\delta}, \tag{5.7}$$

$$\chi_{ij}^{ee} = \frac{NV}{\hbar}\frac{1}{\varepsilon_0}\sum_n \frac{\langle 0\,|\Delta P_i|\,n\rangle\,\langle n\,|\Delta P_j|\,0\rangle}{\omega - \omega_n + i\delta}, \tag{5.8}$$

where $\Delta\mathbf{M}$ and $\Delta\mathbf{P}$ are, respectively, the dynamical polarization and magnetization induced by the magnon. The matrix element of $\Delta\mathbf{M}$ can be deduced by using spin wave theory. For the calculation of $\Delta\mathbf{P}$, we assume the metal ligand hybridization type magnetoelectric coupling and the coupling constant is determined by the fitting of dc magnetoelectric response measured by Murakawa *et al*[68]. For the detail of theoretical calculations, see Appendix B. In Fig. 5.7, we plot the theoretically calculated and experimentally observed relative non-reciprocity $(\Delta S_{12}-\Delta S_{21})/(\Delta S_{12}+\Delta S_{21})$ for the ω_1 mode. Both the microwave absorption and the difference of ΔS_{12} and ΔS_{21} decrease with decreasing the magnetic field. The relative non-reciprocity gradually increases as the magnetic field is decreased. The theoretical calculation of relative non-reciprocity coincides with the experimental data with respect to both the magnitude and the field dependence. On the other hand, the theoretical value of non-reciprocity in the second experimental geometry is quite small compared with the first one, similarly to the experimental result. In

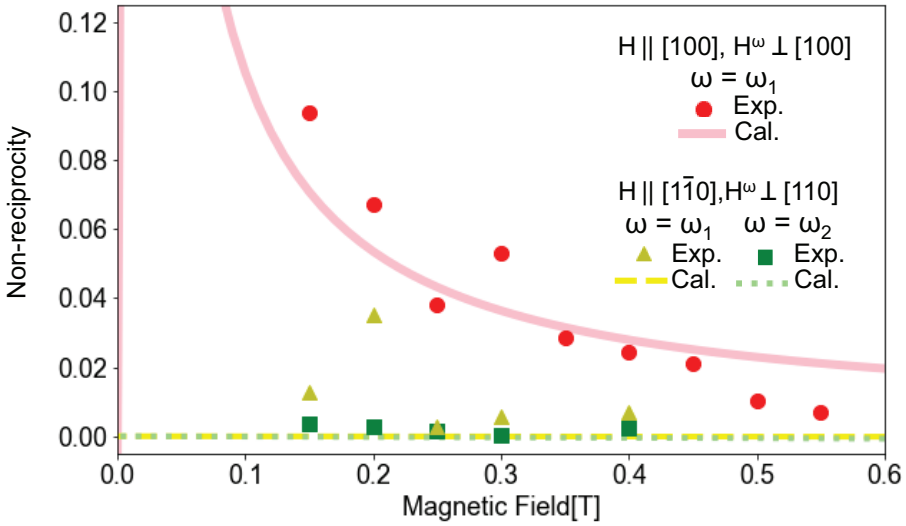

Figure 5.7: **Relative microwave non-reciprocity.** The relative microwave non-reciprocity $(\Delta S_{12} - \Delta S_{21})/(\Delta S_{12} + \Delta S_{21})$ for $\mathbf{H} \parallel [100]$, $\mathbf{H}^{\omega} \perp [100]$ for the mode 1 is plotted as circles. Solid line stands for the corresponding theoretical calculation. The relative microwave non-reciprocities for $\mathbf{H} \parallel [1\bar{1}0]$, $\mathbf{H}^{\omega} \perp [110]$ for ω_1 mode and ω_2 mode are plotted as triangles and squares, respectively. Dashed and dotted lines show the theoretical calculation of microwave non-reciprocity of ω_1 mode and ω_2 mode for $\mathbf{H} \parallel [1\bar{1}0]$, $\mathbf{H}^{\omega} \perp [110]$, respectively.

this geometry, the static polarization shows a maximum as a function of angle of $\mathbf{H}$[68], and the alternating electric polarization due to magnon excitation becomes quite small. For this reason, the non-reciprocity due to the dynamical ME effect is also quite small in this case. Thus, the microwave non-reciprocity in this system is quantitatively explained by the theoretical calculation, which give rise to the satisfactory understanding of microwave non-reciprocity in $Ba_2MnGe_2O_7$.

5.4 Summary

In summary, we observed the antiferromagnetic magnon modes of $Ba_2MnGe_2O_7$ in the microwave region. The notable microwave non-reciprocity was observed for the ω_1 mode for $\mathbf{H} \parallel [100]$ and $\mathbf{H}^{\omega} \perp [100]$. On the other hand, it is negligible for both the ω_1 mode and ω_2 mode when $\mathbf{H} \parallel [1\bar{1}0]$ and $\mathbf{H}^{\omega} \perp [110]$. The presence /absence

and magnitude of non-reciprocity are explained by the theoretical analysis based on the spin wave theory and Kubo formula. These quantitative experiment-theory correspondences adequately ensure the validity of background physics such as non-reciprocal microwave response and the metal ligand hybridization mechanism.

Chapter 6

Conclusions

We have demonstrated the non-reciprocity of the microwave and the magnon propagations in the non-centrosymmetric magnets. We have obtained the new knowledge about the non-reciprocal microwave response related to magnon excitations as follows.

- Magnon non-reciprocally propagates along the magnetization in a bulk ferromagnet with chiral crystal structure. This non-reciprocity can be explained by the asymmetric magnon dispersion owing to the Dzyaloshinskii-Moriya interaction which is only finite in the system with simultaneous breaking of time-reversal symmetry and space-inversion symmetry. This conclusion is supported by the results in Section 3.3.

- The non-reciprocity derived from the Dzyaloshinskii-Moriya interaction in a chiral ferromagnet is clearly discriminated from the non-reciprocities originated from the Damon-Eshbach mode. This is because the former propagates parallel to the direction of the magnetic field, whereas the latter propagates perpendicular to the direction of the magnetic field. This conclusion is based on the results in Section 3.3.

- The multiferroic helimagnet $Ba_2Mg_2Fe_{12}O_{22}$ has the conical magnon excitation in the microwave region. In the microwave region, the type-II multiferroics $Ba_2Mg_2Fe_{12}O_{22}$ shows the optical magnetoelectric effect. In addition, the amplitude and the sign of the non-reciprocity of microwave can be con-

trolled by the poling electric field. This conclusion is introduced by the results in Chapter 4.

- The multiferroic antiferromagnet $Ba_2MnGe_2O_7$ has the conventional antiferromagnetic magnon modes with easy plane anisotropy in the microwave region. The fitting of experimentally observed magnetic field dependence of these modes to the theoretical equation provides the exchange interaction constant and the magnetic anisotropy of $Ba_2MnGe_2O_7$. We observed the microwave non-reciprocity of one of the magnon modes. The microwave non-reciprocity is quantitatively explained by using the spin wave theory, the Kubo formula, and the metal ligand hybridization mechanism. This conclusion is drawn by the results and discussion in Chapter 5.

From what has been discussed and newly obtained as mentioned above, we can conclude the following.

One goal of the non-reciprocal response is the realization of completely non-reciprocal (one-way) propagation or isolator. We need to build theories of non-reciprocal response for that. Our study reveals the following two points as the basic theory. One is "In a non-centrosymmetric bulk ferromagnet, the Dzyaloshinskii-Moriya interaction makes non-reciprocal magnon propagation." In order to realize the magnon-isolator by using a bulk magnet, studying other bulk magnets, such as ferroelectric ferromagnets and centrosymmetric conical magnets, and increasing the magnitude of the non-reciprocity will become issues in the future. The other is "The non-reciprocal microwave propagation is so small that the observation is difficult near the typical antiferromagnetic magnon excitations, but the not small non-reciprocal microwave propagation is observed only in the low magnetic field ($\sim$100 mT) in the ω_1 mode." Although antiferromagnetic magnon excitations have been studied mostly in the high magnetic field (>1 T), from the point of view of the non-reciprocal response, our study suggests that it is necessary to study them in the lower magnetic field. On the other hand, our study suggests that the hexaferrite has the potential of the electrically controllable microwave-isolator as a new microwave function. While the poling procedure is needed to control the electric polarization in $Ba_2Mg_2Fe_{12}O_{22}$ at present, the electrical switching of polarization is, in principle, possible after resolving the problem of electrical leakage due to

residual carriers. In fact, some research groups succeeded in switching the ferroelectric polarization in a related material[**?**, **?**]. In addition, hexaferrite has many kinds of materials including the room temperature multiferroics. The future issues are to realize the non-reciprocal microwave propagation at room temperature, to increase the magnitude of non-reciprocity and to accelerate the switching speed of the polarization.

Appendix A

Theory of magnon

A.1 Magnon modes in ferromagnets

In this section, we would like to review the magnon theory in ferromagnets and calculate the magnetic field dependence of magnon frequency for Section 3.2. For the details of magnon theory, see the standard texts[97, 75].

A.1.1 Uniform magnetic resonance mode in ferromagnets

Vibration of the spin or the magnetic moment propagates as the wave in material, which is denoted as spin wave. The magnetic interactions between the moments, such as the exchange interaction and the magnetic dipole-dipole interaction, provide the spin wave. The spin wave was first introduced by Bloch using the microscopic model with the exchange interaction[98] in 1930, and in this paper he derived the $T^{3/2}$ law which is the law about the temperature variation of saturation magnetization in ferromagnets at low temperature. This shows that the spontaneous magnetization decreases with the three-halves power of T via the spin wave excited by thermal energy, and it was observed six years after by Fallot[99]. The semiclassical derivation of spin wave was first published by Heller and Kramers in 1934[100], after that Herring and Kittel reviewed clearly[101]. On the other hand, after ten years of the proposal of spin wave, Holstein and Primakoff derived the quantized spin wave, which is called magnon, from the second quantization with the exchange interaction, the dipole interaction and the Zeeman interaction

between a magnetic field and spin[102]. Here we show the equation of motion of magnetization which is used for the semiclassical approach.

Equation of motion of magnetization

Let us consider the time variation of spin momentum $\mathbf{S}$ with the external magnetic field $\mu_0\mathbf{H}$ by using the Heisenberg picture.

$$\frac{d\mathbf{S}}{dt} = -\frac{i}{\hbar}[\mathbf{S}, \mathcal{H}] = -\mu_0(\mathbf{S} \times \mathbf{H}), \tag{A.1}$$

where $\hbar$ is the Planck constant divided by 2π. Here we used the Hamiltonian $\mathcal{H} = \mu_0\mathbf{H} \cdot \mathbf{S}$. The time derivative of the angular momentum shows the torque, so the right-hand side in Eq.(A.1) indicates that the external field provides the torque to the spin momentum. From this equation, we can find that the spin continues precessing around the magnetic field. On the other hand, by considering the magnetization as the classical vector, the following equation expresses the time variation of magnetization.

$$\frac{d\mathbf{M}}{dt} = -\gamma\mu_0(\mathbf{M} \times \mathbf{H}) \tag{A.2}$$

Here, $\gamma = g\mu_{\mathrm{B}}$ is the gyromagnetic ratio and g is the g-factor and μ_{B} is the Bohr magneton. This phenomenological equation is the lossless form of the Landau-Lifshitz (LL) equation of motion for the magnetization. If the magnetization followed the equation, when the magnetization began to precess around the field, it kept the state of motion as the stationary state. However in real materials the magnetization interacts with the phonon and the magnon, and its energy dissipation works to the magnetization motion as the damping term. As a result, the magnetization gradually becomes to be parallel to the field. This dissipation mechanism was introduced by Landau and Lifshitz in 1935 in the following way[51].

$$\frac{d\mathbf{M}}{dt} = -\gamma\mu_0(\mathbf{M} \times \mathbf{H}) + \lambda\mathbf{M} \times (\mathbf{M} \times \mathbf{H}) \tag{A.3}$$

This is the loss form of the Landau-Lifshitz equation. Here the λ is the damping constant of LL equation, and this equation only offers an indication of the magnetization motion when the λ is much less than γ. In contrast, in 1955 Gilbert introduced the new equation of motion of magnetization by using the time derivative of magnetization as the damping term[52].

$$\frac{d\mathbf{M}}{dt} = -\gamma\mu_0(\mathbf{M} \times \mathbf{H}) + \frac{\alpha}{M_s}\mathbf{M} \times \frac{d\mathbf{M}}{dt} \tag{A.4}$$

Here, the M_s is the saturation magnetization and the α is the Gilbert damping constant. This equation holds without dependence on the amplitude of the damping constant. This is called the Landau-Lifshitz-Gilbert equation or shortly the LLG equation. Today when we consider the magnetization motion we use the LLG equation in a lot of cases and it is the easiest way for the uniform magnon mode, where the all magnetization oscillate with the same phases. Such magnon mode at wave number $k = 0$ is called the ferromagnetic resonance (FMR) or simply the uniform mode.

Magnon energy with magnetic anisotropy

Firstly, considering the magnetic anisotropy of the sample shape, we introduce the relation of the magnon energy in uniform mode and the saturation magnetization and magnetic fields. Assuming that the time-dependent magnetization $\mathbf{M}(t) = \mathbf{M}_0 + \mathbf{m}(t)$ and the time-dependent magnetic field $\mu_0\mathbf{H}(t) = \mu_0\mathbf{H}_0 + \mu_0\mathbf{h}(t)$ and its time-dependent terms $\mathbf{m}(t) \propto e^{i\omega t}$ and $\mathbf{h}(t) \propto e^{i\omega t}$, we substitute them in the LLG equation [Eq.(A.4)].

$$i\omega\mathbf{m} + \gamma\mathbf{m} \times \mu_0\mathbf{H}_0 + \frac{i\alpha\omega}{M_s}\mathbf{m} \times \mathbf{M}_0 = -\gamma\mathbf{M}_0 \times \mu_0\mathbf{h} \tag{A.5}$$

Here, we used the linear approximation that the second or higher order time-dependent terms are ignored. As the following, the magnetic shape anisotropy is introduced as the demagnetizing tensor $\tilde{\mathbf{N}}$.

$$\tilde{\mathbf{N}} = \begin{pmatrix} N_{11} & N_{12} & N_{13} \\ N_{12} & N_{22} & N_{23} \\ N_{13} & N_{23} & N_{33} \end{pmatrix} \tag{A.6}$$

And the magnetic fields get the additional term of the tensor $\tilde{\mathbf{N}}$.

$$\mu_0\mathbf{H}_0 = \mu_0\mathbf{H}_{e0} - \tilde{\mathbf{N}} \cdot \mathbf{M}_0 \tag{A.7}$$

$$\mu_0\mathbf{h} = \mu_0\mathbf{h}_e - \tilde{\mathbf{N}} \cdot \mathbf{m} \tag{A.8}$$

Substituting them in the linearized LLG equation, we obtain the following equation.

$$i\omega\mathbf{m}+\gamma\mathbf{m}\times(\mu_0\mathbf{H}_{e0}-\tilde{\mathbf{N}}\cdot\mathbf{M}_0)+\gamma(\tilde{\mathbf{N}}\cdot\mathbf{m})\times\mathbf{M}_0-\frac{i\alpha\omega}{M_s}\mathbf{m}\times\mathbf{M}_0 = -\gamma\mathbf{M}_0\times\mu_0\mathbf{h}_e. \tag{A.9}$$

Here, supposing that the static magnetic field and the saturation magnetization is parallel to the z axis and that the time variation of the external field $\mathbf{h}_e = 0$ and that the damping of magnetization $\alpha = 0$, the magnon frequency ω_0 is

$$\omega_0 = \sqrt{(\omega_H + \gamma N_{11} M_s)(\omega_H + \gamma N_{22} M_s) - \gamma N_{12}^2 M_s^2} \tag{A.10}$$

$$\omega_H = \gamma(H_{e0} - N_{33} M_s). \tag{A.11}$$

Furthermore, considering the principal axis respectively diagonalizes the demagnetizing tensor.

$$\omega_0 = \gamma\mu_0 \sqrt{(H_{e0} + (N_x - N_z)M_s)(H_{e0} + (N_y - N_z)M_s)} \tag{A.12}$$

It is the famous formula introduced by Kittel[103], so the FMR mode is sometimes also called the Kittel mode. If the shape of magnetic material is plate-like which the widest plane is in the yz space [Fig. A.1(a)], the demagnetization coefficients are respectively

$$N_x = 1, N_y = N_z = 0. \tag{A.13}$$

Thus, the magnon frequency is

$$\omega_0 = \gamma\mu_0 \sqrt{H_{e0}(H_{e0} + M_s)}. \tag{A.14}$$

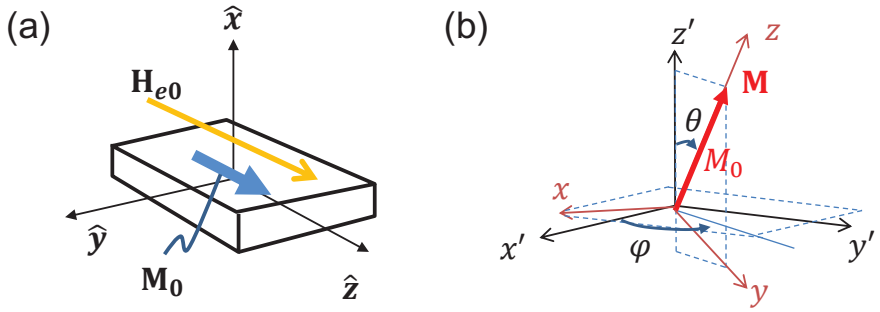

Figure A.1: **Coordinate axes for calculation of diamagnetic field effect against magnon energy.** (a)Coordinate axes for the plate-like sample, (b)Coordinate axes for the case of the rotated magnetization.

Secondly, let us consider the magnetocrystalline-anistropy as the diamagnetic field to obtain the magnon frequency in more detail. For example in cubic, when

we only consider the first order of anisotropic constant K_1, the magnetocrystalline-anisotropy energy is

$$U_{an} = \frac{1}{4}K_1(\sin^2 2\theta + \sin^4\theta \sin^2 2\varphi). \tag{A.15}$$

The coordinate axes of the rotational magnetization is as shown in Fig. A.1(b). Here, the directional cosines of magnetization are written as

$$\begin{aligned} \sin^2\theta &= (1 - \frac{M_{z'}^2}{M_s^2}), \cos^2\theta = \frac{M_{z'}^2}{M_s^2} \\ \sin^2\varphi &= \frac{M_{y'}^2}{M_s^2}(1 - \frac{M_{z'}^2}{M_s^2})^{-1}, \cos^2\varphi = \frac{M_{x'}^2}{M_s^2}(1 - \frac{M_{z'}^2}{M_s^2})^{-1}. \end{aligned} \tag{A.16}$$

From these expression, $U_{an} = K_1(1 - \frac{M_{z'}^2}{M_s^2})\frac{M_{z'}^2}{M_s^2} + \frac{M_{x'}^2}{M_s^2}\frac{M_{y'}^2}{M_s^2}$ and the effective field of magnetocrystalline-anisotropy is

$$\mu_0 \mathbf{H}_{an} = -\frac{\partial U_{an}}{\partial \mathbf{M}}, \tag{A.17}$$

in the form

$$\mu_0 \mathbf{H}_{an} = -\tilde{\mathbf{N}}^{an}\mathbf{M}. \tag{A.18}$$

Here the goal is obtaining the magnon frequency with $M_x \parallel [111]$ and $M_y \parallel [\bar{1}\bar{1}2]$ and $M_z \parallel [1\bar{1}0]$. This calculation is preparation for Chapter 3. In the case that the direction of magnetization is $[1\bar{1}0]$ direction, substituting $\theta = \frac{\pi}{2}$ and $\varphi = -\frac{\pi}{4}$ in the form of magnetization with $x' - y' - z'$ coordinate leads to that the effective field of magnetocrystalline-anisotropy is

$$\mu_0 \mathbf{H}_{an} = \mu_0 \begin{pmatrix} H_{anx} \\ H_{any} \\ H_{anz} \end{pmatrix} = \frac{K_1}{2M_s^4} \begin{pmatrix} 2M_x(M_s^2 - M_x^2) \\ 4(2M_y^3 - M_s^2 M_y) \\ -2M_s(M_s^2 - M_x^2) \end{pmatrix}. \tag{A.19}$$

When we use the approximation $M_x^2, M_y^2 \sim 0$ because of $M_x, M_y \ll M_z \simeq M_s$,

$$\mu_0 \mathbf{H}_{an} = -\frac{K_1}{M_s^2} \begin{pmatrix} -1 & 0 & 0 \\ 0 & 2 & 0 \\ 0 & 0 & 1 \end{pmatrix} \begin{pmatrix} M_X \\ M_y \\ M_s \end{pmatrix} = -\tilde{\mathbf{N}}^{an} \cdot \mathbf{M}. \tag{A.20}$$

Next, changing the coordinate rotated around the z axis leads to that the effective

field is

$$\begin{aligned}\mu_0\mathbf{H}_{an} &= (e_x,e_y,e_z)^t\tilde{\mathbf{U}}\tilde{\mathbf{U}}\tilde{\mathbf{N}}^t\tilde{\mathbf{U}}\tilde{\mathbf{U}}\begin{pmatrix} M_X \\ M_y \\ M_z \end{pmatrix} \\ &= (e_x^{''},e_y^{''},e_z^{''})\tilde{\mathbf{N}}^{''}\begin{pmatrix} M_X^{''} \\ M_y^{''} \\ M_z^{''} \end{pmatrix}, \end{aligned} \tag{A.21}$$

where the $\tilde{\mathbf{U}}$ is the rotation matrix and the inverse matrix $\tilde{\mathbf{U}}^{-1}$ is the same as the transposed matrix ${}^t\tilde{\mathbf{U}}$. In the case of the $M_x^{''} \parallel [111]$ and $M_y^{''} \parallel [\bar{1}\bar{1}2]$, the rotation matrix is

$$\tilde{\mathbf{U}} = \frac{1}{\sqrt{3}}\begin{pmatrix} -\sqrt{2} & 1 & 0 \\ -1 & -\sqrt{2} & 0 \\ 0 & 0 & \sqrt{3} \end{pmatrix}, \tag{A.22}$$

so the demagnetizing tensor of magnetocrystalline-anisotropy is

$$\tilde{\mathbf{N}}^{an} = \frac{K_1}{M_s^2}\begin{pmatrix} 0 & \sqrt{2} & 0 \\ \sqrt{2} & 1 & 0 \\ 0 & 0 & 1 \end{pmatrix}. \tag{A.23}$$

Finally, combining the obtained demagnetizing tensors, we obtain the total demagnetizing tensor $\tilde{\mathbf{N}}_{total}$.

$$\begin{aligned}\tilde{\mathbf{N}}_{total} &= \tilde{\mathbf{N}} + \tilde{\mathbf{N}}^{an} \\ &= \begin{pmatrix} a & 0 & 0 \\ 0 & b & 0 \\ 0 & 0 & 1-a-b \end{pmatrix} + \frac{K_1}{M_s^2}\begin{pmatrix} 0 & \sqrt{2} & 0 \\ \sqrt{2} & 1 & 0 \\ 0 & 0 & 1 \end{pmatrix}. \end{aligned} \tag{A.24}$$

From this result, the magnon frequency is

$$\begin{aligned}\omega_0 &= \sqrt{(\omega_H+\gamma a M_s)(\omega_H+\gamma(b+\alpha_1)M_s) - 2\gamma\alpha_1^2 M_s^2} \\ \omega_H &= \gamma(H_{e0} - (1-a-b+\alpha_1)M_S), \end{aligned} \tag{A.25}$$

where the $\frac{K_1}{M_s^2} = \alpha_1$. When we substitute $a = N_{111}$ and $b = N_{\bar{1}\bar{1}2}$ in Eq.(A.25), the magnon frequency is

$$\omega_0 = \gamma\sqrt{[\mu_0 H + (N_{111} - N_{1\bar{1}0})\mu_0 M_s - \frac{K_1}{M_s}][\mu_0 H_0 + (N_{\bar{1}\bar{1}2} - N_{1\bar{1}0})\mu_0 M_s]2\frac{K_1^2}{M_s^2}} \tag{A.26}$$

where $N_{111}, N_{\bar{1}\bar{1}2}$, and $N_{1\bar{1}0}$ are the demagnetization factor for [111], [$\bar{1}\bar{1}2$], and [$1\bar{1}0$] direction, respectively.

A.1.2 Ferromagnetic magnon mode with finite wave number

The interactions which propagate the magnon are the exchange interaction and the magnetic dipole-dipole interaction. The exchange interaction is dominant in the large wave number region, in contrast the dipolar interaction is dominant in the small wave number region, so the magnon modes are classified in the wave number space. The quantum magnon mode via the former is usually called the exchange magnon, the classical magnon mode via the latter is usually called the dipolar magnon, and the intermediate mode is usually called the dipolar-exchange magnon[104, 105].

The dipolar magnon is mentioned in detail in the next section, so here I ignore the dipolar interaction in Hamiltonian. For example in the simple cubic lattice structure with the lattice constant a, the continuum approximation of Hamiltonian is

$$\begin{aligned}
\mathcal{H} &= -\frac{1}{V_0}\int d\mathbf{r}\left\{J\sum_i \mathbf{S}(\mathbf{r})\cdot\mathbf{S}(\mathbf{r}+a\mathbf{e}_i) - \mu_0\mathbf{H}\cdot\mathbf{S}(\mathbf{r})\right\} \\
&= -\frac{1}{V_0}\int d\mathbf{r}\left\{J\sum_i[-\frac{1}{2}\mathbf{S}(\mathbf{r}+a\mathbf{e}_i) - \mathbf{S}(\mathbf{r})^2 + S^2] - \mu_0\mathbf{H}\cdot\mathbf{S}(\mathbf{r})\right\} \\
&= \frac{1}{V_0}\int d\mathbf{r}\left\{\frac{Ja^2}{2}\sum_i(\frac{\partial\mathbf{S}(\mathbf{r})}{\partial\mathbf{e}_i})^2 - \mu_0\mathbf{H}\cdot\mathbf{S}(\mathbf{r})\right\} \\
&= \frac{1}{V_0}\int d\mathbf{r}\left\{\frac{Ja^2}{2}(\nabla\mathbf{S}(\mathbf{r}))^2 - \mu_0\mathbf{H}\cdot\mathbf{S}(\mathbf{r})\right\}, \qquad \text{(A.27)}
\end{aligned}$$

where $\mathbf{S}$ is the spatially dependent spin moment divided by $\hbar$, J is the exchange interaction constant and V_0 is the volume of the unit cell. By using the approximate Holstein-Primakoff transformation[102], in the induced ferromagnetic state (IFMS)

with the magnetic field $\mathbf{H} \parallel \mathbf{z}$ the $\mathbf{S}(\mathbf{r})$ is

$$\begin{aligned} S_x &= i\sqrt{\frac{S}{2}}[a(\mathbf{r}) - a(\mathbf{r})^+] \\ S_y &= \sqrt{\frac{S}{2}}[a(\mathbf{r}) + a(\mathbf{r})^+] \\ S_z &= S - a(\mathbf{r})^+ a(\mathbf{r}), \end{aligned} \tag{A.28}$$

where the $a(\mathbf{r})$ and $a(\mathbf{r})^+$ are the free magnon operators, which satisfy $[a(\mathbf{r}), a(\mathbf{r}')^+] = \delta(\mathbf{r} - \mathbf{r}')$. Indeed the Fourier transform of $a(\mathbf{r})$ is defined by

$$a(\mathbf{r}) = \sum_k a_k \exp(i\mathbf{k} \cdot \mathbf{r}). \tag{A.29}$$

From these results, the Hamiltonian is expressed as following[55].

$$\mathcal{H} = \sum_k (2JSk^2 + \mu_0 H) a_k^+ a_k \tag{A.30}$$

Thus, the magnon energy is

$$\hbar\omega_k = 2JSk^2 + \mu_0 H \tag{A.31}$$

The above calculations clearly show that the magnon gains the Zeeman energy and increases with the square of wave number with the exchange interaction and the external dc magnetic field. Without the magnetic field, the magnon at $k = 0$ is the massless mode, which is known as the Nambu-Goldstone (N-G) magnon mode[106, 107, 108]. The branches of the N-G mode are sometimes called the N-G magnon mode in the broad sense or the quasi N-G mode.

A.2 Dipolar magnon modes

In this section, we introduce the dipolar magnon mode so-called the magnetostatic wave modes by the limit of long wavelength of the Maxwell's equations for Section 3.3. The magnetostatic wave modes are classical modes, so they are completely different from the exchange magnon mode. We show that the magnetostatic waves are excited by the external AC magnetic field with a long wavelength.

A.2.1 Gyrotropy of ferromagnets

First, let us consider the interaction of the magnetization motion and the electromagnetic wave. From substituting the time-dependent magnetization $\mathbf{m}(t) = \mathbf{m}_0 e^{i\omega t}$ and the time-dependent magnetic field $\mathbf{h}(t) = \mathbf{h}_0 e^{i\omega t}$ in the LLG equation without damping term [Eq.(A.2)], the magnetic susceptibility tensor $\tilde{\chi}$ is obtained.

$$\mathbf{m} = \tilde{\chi} \cdot \mathbf{h}$$

$$\tilde{\chi} = \begin{pmatrix} \chi & -i\kappa & 0 \\ i\kappa & \chi & 0 \\ 0 & 0 & 0 \end{pmatrix}, \tag{A.32}$$

where

$$\chi = \frac{\omega_M \omega_H}{\omega_H^2 - \omega^2}, \kappa = \frac{\omega_M \omega}{\omega_H^2 - \omega^2} \tag{A.33}$$

$$\omega_H = \gamma \mu_0 H_0, \omega_M = \gamma \mu_0 M_s. \tag{A.34}$$

The magnetic susceptibility was first calculated by Polder[109] in 1949, so this tensor is called Polder tensor or Polder susceptibility tensor. The elements of Polder tensor diverge at the frequency $\omega = \omega_H$ and its property provides the ferromagnetic resonance. As a general rule, the ac magnetic field $\mathbf{h}$ can only oscillate the magnetization parallel to $\mathbf{h}$. However the Polder tensor has the non-diagonal components, so the ac field $\mathbf{h}$ also can oscillate the magnetization perpendicular to $\mathbf{h}$ with a phase shift of $\pi/2$. Such property owing to the nonsymmetry of the magnetic susceptibility tensor is called magnetic gyrotropy. On the other hand, properties owing to the nonsymmetry of the electric susceptibility, such as Faraday effect, is called electric gyrotropy. From the magnetic susceptibility, we get the time variation of magnetic flux density $\mathbf{b}$ and the permeability tensor $\tilde{\mu}$ as the following.

$$\begin{aligned} \mathbf{b} &= \mu_0 \mathbf{h} + \mu_0 \mathbf{m} \\ &= \mu_0 (\tilde{\mathbf{I}} + \tilde{\chi}) \cdot \mathbf{h} = \tilde{\mu} \cdot \mathbf{h} \end{aligned} \tag{A.35}$$

$$\mathbf{b} = \tilde{\mu} \cdot \mathbf{h}, \tilde{\mu} = \mu_0 \begin{pmatrix} 1+\chi & -i\kappa & 0 \\ i\kappa & 1+\chi & 0 \\ 0 & 0 & 1 \end{pmatrix} \tag{A.36}$$

The diagonal element of permeability is negative in the frequency region from ω_H to $\sqrt{\omega_H(\omega_H+\omega_M)}$. This resonance frequency dependence of permeability is first observed by Griffiths[110]. He put the Ni film (0.025 mm) into the two cylindrical microwave cavity with different resonance frequencies and he measured the magnetic field dependence of the product of permeability and electric resistivity, and he discovered the relation of the magnetic field and the resonance frequency. Such resonance absorption of microwave owing to the magnetization dynamics in ferromagnet is called ferromagnetic resonance absorption.

A.2.2 Magnetostatic wave modes

Let us consider the introduction of the magnetostatic wave (MSW) mode from the Maxwell's equations in the magnetostatic limit $\|\mathbf{k}\| \gg \|\mathbf{k}_0\|$, where $\mathbf{k}_0$ is the wave vector of light. From the Maxwell's equations in this limit, we obtain the following equations.

$$\begin{aligned} \nabla \times \mathbf{h} &= 0 \\ \nabla \cdot \mathbf{b} &= 0 \\ \nabla \times \mathbf{e} &= i\omega \mathbf{b}, \end{aligned} \tag{A.37}$$

where $\mathbf{e}$ is the time variation of electric field and $\mathbf{e} = \mathbf{e}_0 e^{i\omega t}$. These equations are called magnetostatic equations and the waves expressed by them are called magnetostatic waves. When we introduce the magnetostatic scalar potential φ by the equation $\mathbf{h} = -\nabla\varphi$, from the magnetostatic equations and the magnetic susceptibility tensor we obtain the following equation at the dc magnetic field $\mathbf{H}_0 = H_0\mathbf{z}$.

$$(1+\chi)\left[\frac{\partial^2\varphi}{\partial x^2} + \frac{\partial^2\varphi}{\partial y^2}\right] + \frac{\partial^2\varphi}{\partial z^2} = 0 \tag{A.38}$$

This equation was first introduced by Walker[111] in 1957, so it is called Walker's equation. Using the Walker's equation with $\varphi \propto e^{i\mathbf{k}\cdot\mathbf{r}}$ and $\mathbf{H} = H_0\mathbf{z} + \mathbf{h}$, we obtain the frequency of MSW with θ which is the angle of $\mathbf{k}$ and $\mathbf{H}_0$.

$$\omega = \sqrt{\omega_H(\omega_H + \omega_M \sin^2\theta)} \tag{A.39}$$

From the above equation, we get the frequency range of MSW as below.

$$\omega_H \leq \omega \leq \sqrt{\omega_H(\omega_H+\omega_M)} \tag{A.40}$$

Such frequency region is called magnetostatic wave manifold, and it equals the region of the negative permeability. The MSW was first observed by White and Solt using the experiment of cavity resonance with ferrite[112].

The MSW has a lot of unique dispersions depending on the condition of magnetic field and sample shape. Here we only show the case of thin plate-type sample with in-plane magnetic field as shown in Fig. A.2(a). At the in-plane field there are two types of MSW modes. One mode propagates parallel to the magnetic field and the other mode propagates perpendicular to the magnetic field. The former mode is called magnetostatic backward volume wave (MSBVW) mode and the latter is called magnetostatic surface wave (MSSW) mode or Damon-Eshbach mode (DEM) derived from the name of theorists who first introduced the DEM[53]. First, consider the MSW mode propagating parallel to the magnetic field and z axis. Here the magnetostatic scalar potential is expressed as

$$\varphi = (A \sin \kappa x + B \cos \kappa x) \exp ikz, \tag{A.41}$$

where A and B are real constants, κ is the x component of the wave number, and k is the z component of the wave number. The Walker's equation with the boundary condition provides the dispersion relation of MSBVW[113]. For preparation of the experiment in Chapter 3, let us consider the case of the ferrite film where the surface is attached to the metallic ground of the microwave circuit while the top surface is free. First, we solve the walker equation assuming both the top and bottom surface are attached to metal. Then we show the solution for the free boundary condition and suggest the difference of the boundary condition is not critical for the comparison with the experiment. If the surfaces are attached to the metal, the normal component of magnetic induction is zero at the surface. Thus,

$$(1 + \chi_{xx}) \frac{\partial \varphi}{\partial x} = 0, \tag{A.42}$$

at $x = 0$ and $x = t$, where the χ_{xx} is the xx component of the magnetic susceptibility tensor. Putting Eq. A.41 into the above formula, we obtain

$$A = 0, \tag{A.43}$$

$$\kappa = \frac{n\pi}{t}, \tag{A.44}$$

$$\varphi = B \cos(\frac{n\pi}{t} x) \exp ikz, \tag{A.45}$$

where n is a positive integer. Depending on n, the magnetic field distribution along x direction is different. Substituting Eq. A.44 into the walker equation, we get

$$(1+\chi_{xx})\frac{(n\pi)^2}{t^2}+k^2=0. \tag{A.46}$$

The explicit form of χ_{xx} in this configuration is expressed as

$$\chi_{xx}=\frac{\mu_0^2 H_0 M_s}{\mu_0^2 H_0^2-\mu_0\frac{K_1 H_0}{M_s}-\frac{2K_1^2}{M_s^2}-(\omega/\gamma)^2}. \tag{A.47}$$

The higher-order magnetic anisotropy is neglected. Then we get the following dispersion relation:

$$\omega=\gamma\sqrt{\mu_0^2 H_0^2-\mu_0\frac{K_1 H_0}{M_s}-\frac{2K_1^2}{M_S^2}+\frac{\mu_0^2 H_0 M_s}{1+(kt/n\pi)^2}} \tag{A.48}$$

Figure A.2(b) indicates the dispersion of MSBVW at $\mu_0 H$ =0.15 T for $LiFe_5O_8$. In addition, we calculated the MSBVW with parameters of the lithium ferrite ($LiFe_5O_8$) and the yttrium iron garnet ($Y_3Fe_5O_{12}$) for preparation of the experiment in Chapter 3.

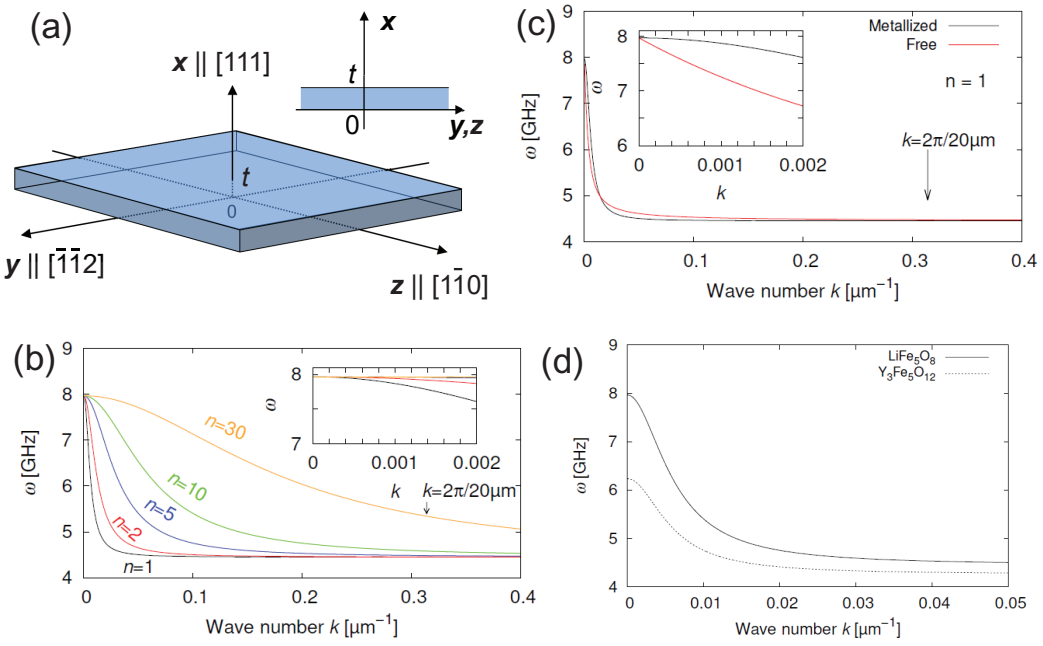

Figure A.2: **Magnetostatic backward volume modes for famous ferrites.** (a) Illustration of the geometry used in the calculation of MSBVW. The plate shows the figure of crystal and [111], [$\bar{1}\bar{1}2$], and [$1\bar{1}0$] are the crystal orientation. (b) The dispersion relations of MSBVW in lithium ferrite ($LiFe_5O_8$) in the case of metalized boundary condition. The index n classifies the magnon mode branches with different spatially oscillating patterns along the normal direction of the crystal plate. The arrow shows the wavelength that can be excited by the antenna which was used for the experiment in Chapter 3, $k = 2\pi/(20\mu\text{m})$. (c) Comparison of the $n = 1$ dispersion relations of MSBVW in lithium ferrite for free and metalized boundary conditions. The arrow shows the momentum k excited by the microwave antenna, $k = 2\pi/(20\mu\text{m})$. Inset shows the dispersion relation in the low k region. (d) The $n = 1$ dispersion relations of $LiFe_5O_8$ (solid lines) and yttrium iron garnet ($Y_3Fe_5O_{12}$) (dashed lines). The metalized boundary condition is employed. Reprinted figures from [65]. Copyright 2015, by American Physical Society.

Appendix B

Microwave non-reciprocity in $Ba_2MnGe_2O_7$

B.1 Magnetic structure in magnetic fields

In this chapter, we theoretically discuss the magnetic excitation and the microwave non-reciprocity in order to compare with the experimentally observed data. Similar calculations were already done in literatures[25, 26, 48]. We assume the Hamiltonian in $Ba_2MnGe_2O_7$ is

$$\mathcal{H} = J \sum_{<i,j>} \mathbf{S}_i \cdot \mathbf{S}_j + K \sum_i \left(S_i^z\right)^2 + g\mu_{\mathrm{B}} \sum_i \mathbf{S}_i \cdot (\mu_0 \mathbf{H}) \,. \tag{B.1}$$

Here, g is a g value, and μ_{B} is the Bohr magneton. μ_0 is the magnetic permeability in vacuum. J is the nearest-neighbor exchange interaction constant. The nearest-neighbor exchange interaction is antiferromagnetic ($J > 0$). The interplane magnetic interaction is small compared with the intraplane one[95], therefore ignored here for simplicity. Dzyaloshinskii-Moriya interaction is also ignored. The single-ion anisotropy $K > 0$ indicates the easy-plane-type magnetic anisotropy. $\mathbf{S}_i = (S_i^x, S_i^y, S_i^z)$ is the spin operator at i sublattice ($i = \mathrm{A}, \mathrm{B}$), the magnetic moment is $\mathbf{m}_i = -g\mu_{\mathrm{B}}\mathbf{S}_i$.

In this section, we deduce the magnetic structure in magnetic fields at $T = 0$ K with use of classical approach. We assume two-sublattice magnetic structure. The magnetic field is applied in the tetragonal plane. Therefore, the magnetic field

vector can be expressed as

$$\mathbf{H} = H\left(\cos\theta_{\mathrm{H}}, \sin\theta_{\mathrm{H}}, 0\right). \tag{B.2}$$

In this case, the spins for each sublattice are vector along the tetragonal plane expressed as

$$\mathbf{S}_i = S\left(\cos\theta_i, \sin\theta_i, 0\right), \tag{B.3}$$

where $\theta_i (i = \mathrm{A}, \mathrm{B})$ stands for the angle of spin for the i sublattice. Then the energy is estimated as

$$\frac{E}{N} = 4JS^2 \cos 2\theta + hS\left\{\cos\left(\theta_{\mathrm{A}} - \theta_{\mathrm{H}}\right) + \cos\left(\theta_{\mathrm{B}} - \theta_{\mathrm{H}}\right)\right\}, \tag{B.4}$$

where $2\theta = \theta_{\mathrm{A}} - \theta_{\mathrm{B}} \quad (\theta_{\mathrm{A}} > \theta_{\mathrm{B}}), \quad h = g\mu_{\mathrm{B}}\mu_0 H$. N is the number of unit cell. Neglecting the finite temperature effect, the spins are ordered so that the energy is minimized. From the condition, we obtain the directions of spins as follows;

$$\cos\theta = \frac{h}{8JS}, \tag{B.5}$$

$$\theta_{\mathrm{A}} = \theta_{\mathrm{H}} + \theta + \pi, \quad \theta_{\mathrm{B}} = \theta_{\mathrm{H}} - \theta + \pi. \tag{B.6}$$

The obtained magnetic structure is shown in Fig. B.1(a).

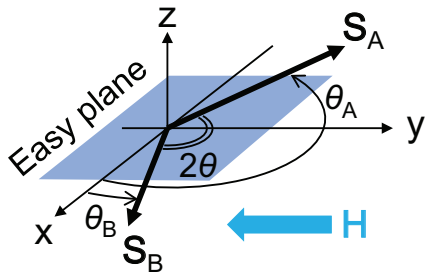

Figure B.1: The ground state of easy-plane-type antiferromagnets in the inplane magnetic field **H**.

B.2 Electric polarization

The electric polarization of $Ba_2MnGe_2O_7$ can be induced by the metal ligand hybridization mechanism. The local electric dipole moment at i sublattice is described as

$$\mathbf{p}_i = \lambda \sum_j (\mathbf{S}_i \cdot \mathbf{e}_{ij})^2 \mathbf{e}_{ij}, \tag{B.7}$$

where λ is a constant and $\mathbf{e}_{ij} = (e_{ij}^x, e_{ij}^y, e_{ij}^z)$ is the unit vector along the bond connecting Mn ion at i sublattice and jth coordinated oxygen ion. For $Ba_2MnGe_2O_7$, the lattice constants are $a = b = 8.5022$ Å and $c = 5.5244$ Å. In the unit cell, the Mn ions are located at the positions (0,0,0) and $(0.5a, 0.5a, 0)$. The four coordinated oxygens around the Mn A ion are at $(0.0825a, 0.187a, 0.2117c)$, $(-0.0825a, -0.187a, 0.2117c)$, $(-0.187a, 0.0825a, -0.2117c)$, and $(0.187a, -0.0825a, -0.2117c)$. On the other hand, The coordinated oxygens around Mn B are at $(0.687a, 0.5825a, 0.2117c)$, $(0.313a, 0.4175a, 0.2117c)$, $(0.4175a, 0.687a, -0.2117c)$, $(0.5825a, 0.313a, -0.2117c)$. From these informations, we obtained

$$\begin{aligned}
\mathbf{e}_{A1} &= (0.33487, 0.75903, 0.55833) = (d, f, l), \\
\mathbf{e}_{A2} &= (-d, -f, l), \\
\mathbf{e}_{A3} &= (-f, d, -l), \\
\mathbf{e}_{A4} &= (f, -d, -l),
\end{aligned}$$

$$\begin{aligned}
\mathbf{e}_{B1} &= (f, d, l), \\
\mathbf{e}_{B2} &= (-f, -d, l), \\
\mathbf{e}_{B3} &= (-d, f, -l), \\
\mathbf{e}_{B4} &= (d, -f, -l).
\end{aligned}$$

The polarization is estimated as the summation of local electric dipole moments divided by the volume as follows;

$$\begin{aligned}
\mathbf{P} &= \frac{\lambda}{2NV} \sum_{i}^{2N} \sum_{j}^{4} \left(\mathbf{S}_i \cdot \mathbf{e}_{ij}\right)^2 \mathbf{e}_{ij} \\
&= \frac{\lambda}{2V} \sum_{j=1}^{4} \left[\left\{ \left(\mathbf{S}_{\mathrm{A}} \cdot \mathbf{e}_{Aj}\right)^2 + \left(\mathbf{S}_{\mathrm{B}} \cdot \mathbf{e}_{Aj}\right)^2 \right\} \mathbf{e}_{Aj} \right. \\
&\quad \left. + \left\{ \left(\mathbf{S}_{\mathrm{A}} \cdot \mathbf{e}_{Bj}\right)^2 + \left(\mathbf{S}_{\mathrm{B}} \cdot \mathbf{e}_{Bj}\right)^2 \right\} \mathbf{e}_{Bj} \right] \\
&= \frac{8dfl\lambda}{V} \begin{pmatrix} S_{\mathrm{A}}^y S_{\mathrm{A}}^z + S_{\mathrm{B}}^y S_{\mathrm{B}}^z \\ S_{\mathrm{A}}^x S_{\mathrm{A}}^z + S_{\mathrm{B}}^x S_{\mathrm{B}}^z \\ S_{\mathrm{A}}^x S_{\mathrm{A}}^y + S_{\mathrm{B}}^x S_{\mathrm{B}}^y \end{pmatrix}. \qquad \text{(B.8)}
\end{aligned}$$

The effect of inter layer antiferromagnetic stacking is included in this formula. We introduce the ferromagnetic vector $\mathbf{S}_{\mathrm{F}}$ and the antiferromagnetic vector $\mathbf{S}_{\mathrm{AF}}$;

$$\mathbf{S}_{\mathrm{F}} = \begin{pmatrix} S^x_{\mathrm{A}} + S^x_{\mathrm{B}} \\ S^y_{\mathrm{A}} + S^y_{\mathrm{B}} \\ S^z_{\mathrm{A}} + S^z_{\mathrm{B}} \end{pmatrix}, \tag{B.9}$$

$$\mathbf{S}_{\mathrm{AF}} = \begin{pmatrix} S^x_{\mathrm{A}} - S^x_{\mathrm{B}} \\ S^y_{\mathrm{A}} - S^y_{\mathrm{B}} \\ S^z_{\mathrm{A}} - S^z_{\mathrm{B}} \end{pmatrix}. \tag{B.10}$$

With these vectors, the polarization can be expressed as

$$\mathbf{P}^0 = \frac{4dfl\lambda}{V} \begin{pmatrix} S^y_{\mathrm{F}} S^z_{\mathrm{F}} + S^y_{\mathrm{AF}} S^z_{\mathrm{AF}} \\ S^x_{\mathrm{F}} S^z_{\mathrm{F}} + S^x_{\mathrm{AF}} S^z_{\mathrm{AF}} \\ S^x_{\mathrm{F}} S^y_{\mathrm{F}} + S^x_{\mathrm{AF}} S^y_{\mathrm{AF}} \end{pmatrix}. \tag{B.11}$$

In order to compare with the experimentally observed polarization and estimate the coupling constant λ, we calculate the magnetic structure at finite temperature with use of molecular field approach. The magnitude of spin is expressed as the thermodynamical average $\langle \mathbf{S}_{\mathrm{A}} \rangle$ and $\langle \mathbf{S}_{\mathrm{B}} \rangle$.

$$\langle \mathbf{S}_i \rangle = \bar{S} \left(\cos\theta'_i, \sin\theta'_i, 0 \right) \tag{B.12}$$

Here $i = \mathrm{A}, \mathrm{B}$ and $|\langle \mathbf{S}_{\mathrm{A}} \rangle| = |\langle \mathbf{S}_{\mathrm{B}} \rangle| = \bar{S}$. From the mean-field approximation, the Hamiltonian is

$$\mathcal{H} = \mathcal{H}_{\mathrm{A}} + \mathcal{H}_{\mathrm{B}}, \tag{B.13}$$

$$\mathcal{H}_{\mathrm{A}} = \sum_i \left(4J \langle \mathbf{S}_{\mathrm{B}} \rangle + \mathrm{g}\mu_{\mathrm{B}}\mu_0 \mathbf{H} \right) \cdot \mathbf{S}_{\mathrm{A}}, \tag{B.14}$$

$$\mathcal{H}_{\mathrm{B}} = \sum_i \left(4J \langle \mathbf{S}_{\mathrm{A}} \rangle + g\mu_{\mathrm{B}}\mu_0 \mathbf{H} \right) \cdot \mathbf{S}_{\mathrm{B}}. \tag{B.15}$$

The effective magnetic fields are

$$\mathbf{H}_{\mathrm{eff,A}} = \frac{4J}{g\mu_{\mathrm{B}}} \langle \mathbf{S}_{\mathrm{B}} \rangle + \mu_0 \mathbf{H}, \tag{B.16}$$

$$\mathbf{H}_{\mathrm{eff,B}} = \frac{4J}{g\mu_{\mathrm{B}}} \langle \mathbf{S}_{\mathrm{A}} \rangle + \mu_0 \mathbf{H}. \tag{B.17}$$

Because the magnetic torques are zero at steady state,

$$\mathbf{H}_{\mathrm{eff,A}} \times g\mu_{\mathrm{B}} \langle \mathbf{S}_{\mathrm{A}} \rangle = \mathbf{H}_{\mathrm{eff,B}} \times g\mu_{\mathrm{B}} \langle \mathbf{S}_{\mathrm{B}} \rangle = 0. \tag{B.18}$$

Thus the direction of spins is determined as follows;

$$2\theta' = \theta'_{\mathrm{A}} - \theta'_{\mathrm{B}} \quad (\theta'_{\mathrm{A}} > \theta'_{\mathrm{B}}), \tag{B.19}$$

$$\cos\theta' = \frac{h}{8J\bar{S}}, \tag{B.20}$$

$$\theta'_{\mathrm{A}} = \theta_{\mathrm{H}} + \theta' + \pi, \quad \theta'_{\mathrm{B}} = \theta_{\mathrm{H}} - \theta' + \pi. \tag{B.21}$$

The thermodynamical average of magnitude of spin $\bar{S}$ is expressed as follows;

$$\begin{aligned} \bar{S} &= SB_s \left[\frac{\mathbf{H}_{\mathrm{eff,A}} \cdot g\mu_{\mathrm{B}} \langle \mathbf{S}_{\mathrm{A}} \rangle}{k_{\mathrm{B}} T} \right] \\ &= SB_s \left[-\frac{4J\left\{2\left(h/8J\right)^2 - \bar{S}^2\right\} - h^2/8J}{k_B T} S \right]. \end{aligned} \tag{B.22}$$

Here k_B is the Boltzmann constant and $B_s[x]$ is the Brillouin function,

$$B_s\left[x\right] = \frac{2S+1}{2S} \coth\left(\frac{2S+1}{2S}x\right) - \frac{1}{2S}\coth\left(\frac{x}{2S}\right). \tag{B.23}$$

From Eq. (B.22), we can numerically obtain the h dependence of $\bar{S}$. The h dependence of θ' is also obtained by Eq. (S20). In the magnetic field along [110] ($\theta_{\mathrm{H}} = \pi/4$),

$$\langle \mathbf{S}_{\mathrm{A}} \rangle = \frac{\bar{S}}{\sqrt{2}} \begin{pmatrix} -\cos\theta' + \sin\theta' \\ -\cos\theta' - \sin\theta' \\ 0 \end{pmatrix}, \quad \langle \mathbf{S}_{\mathrm{B}} \rangle = \frac{\bar{S}}{\sqrt{2}} \begin{pmatrix} -\cos\theta' - \sin\theta' \\ -\cos\theta' + \sin\theta' \\ 0 \end{pmatrix}, \tag{B.24}$$

$$\langle \mathbf{S}_{\mathrm{F}} \rangle = -\sqrt{2}\bar{S}\cos\theta' \begin{pmatrix} 1 \\ 1 \\ 0 \end{pmatrix}, \quad \langle \mathbf{S}_{\mathrm{AF}} \rangle = \sqrt{2}\bar{S}\sin\theta' \begin{pmatrix} 1 \\ -1 \\ 0 \end{pmatrix}. \tag{B.25}$$

Thus the polarization is

$$\mathbf{P} = \frac{8dfl\lambda}{V} \bar{S}^2 \begin{pmatrix} 0 \\ 0 \\ 2\cos^2\theta' - 1 \end{pmatrix}. \tag{B.26}$$

Figure B.2 compares the obtained polarization and experimental data[3]. Here we used parameters, $S = 5/2$, $T = 1.8$ K, $V = 8.5022 \times 8.5022 \times 5.5244 \times 10^{-30}$ m^3, and $4JS/g\mu_{\mathrm{B}} = \mu_0 H_{\mathrm{E}} = 4.67$ T. The h-dependences are similar to each other. From the comparison, we obtained $|\lambda|$ is estimated as 9×10^{-35}Cm.

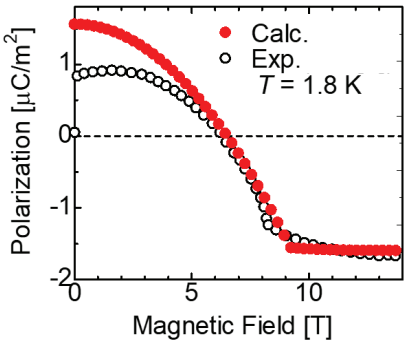

Figure B.2: Polarization experimentally obtained by Murakawa *et al.*[68] and calculated polarization based on Eq. (B.26) with $|\lambda| = 9 \times 10^{-35}$ Cm.

B.3 Antiferromagnetic magnon modes

In this section, we discuss the antiferromagnetic magnon modes. Finite temperature effect is neglected for simplicity. First, we introduced the coordinate system along the spin direction. The spin coordinate system is rotated so that the x-axis is aligned with the direction of ordered spin moments by the unitary operator

$$U = \exp\left(-i\sum_i \theta_i S_i^z\right). \tag{B.27}$$

The spin moments in the rotated system ($\tilde{\mathbf{S}}_i$) are

$$U^\dagger \mathbf{S}_i U \equiv \tilde{\mathbf{S}}_i = R_z\left(\theta_i\right)\mathbf{S}_i, \tag{B.28}$$

where

$$R_z\left(\theta_i\right) = \begin{pmatrix} \cos\theta_i & -\sin\theta_i & 0 \\ \sin\theta_i & \cos\theta_i & 0 \\ 0 & 0 & 1 \end{pmatrix}. \tag{B.29}$$

The Hamiltonian (Eq. (B.1)) is transformed by U into

$$\begin{aligned}\tilde{\mathcal{H}} = J\sum_{<i,j>}\left\{\left(\tilde{S}_i^x\tilde{S}_j^x + \tilde{S}_i^y\tilde{S}_j^y\right)\cos\left(\theta_i-\theta_j\right) + \tilde{S}_i^z\tilde{S}_j^z + \left[\tilde{\mathbf{S}}_i\times\tilde{\mathbf{S}}_j\right]^z\sin\left(\theta_i-\theta_j\right)\right\} \\ + K\sum_i\left(\tilde{S}_i^z\right)^2 + h\sum_i\left\{\tilde{S}_i^x\cos\left(\theta_i-\theta_{\mathrm{H}}\right) - \tilde{S}_i^y\sin\left(\theta_i-\theta_{\mathrm{H}}\right)\right\}.\end{aligned} \tag{B.30}$$

In the rotated system, the Holstein-Primakoff (H-P) transformations are

$$\tilde{S}_i^x = S - a_i^\dagger a_i, \quad \tilde{S}_i^y = \sqrt{\frac{S}{2}}\left(a_i + a_i^\dagger\right) + O\left(S^{-\frac{1}{2}}\right), \quad \tilde{S}_i^z = -i\sqrt{\frac{S}{2}}\left(a_i - a_i^\dagger\right) + O\left(S^{-\frac{1}{2}}\right), \tag{B.31}$$

$$\tilde{S}_j^x = S - b_j^\dagger b_j, \quad \tilde{S}_j^y = \sqrt{\frac{S}{2}}\left(b_j + b_j^\dagger\right) + O\left(S^{-\frac{1}{2}}\right), \quad \tilde{S}_j^z = -i\sqrt{\frac{S}{2}}\left(b_j - b_j^\dagger\right) + O\left(S^{-\frac{1}{2}}\right). \tag{B.32}$$

Here a_i, b_j and $a_i^\dagger$, $b_j^\dagger$ are the boson annihilation and creation operators, respectively. In this chapter, we discuss the magnon modes coupled to the microwave. The microwave wavelength is fairly long compared with the atomic distance. The coupled magnon modes can be regarded as spatially uniform. Therefore, we assume that a_i,$a_i^\dagger$, b_i, and $b_i^\dagger$ are independent of atomic site indicated by suffix i. Hereafter, we omit the suffix. Then the H-P transformed Hamiltonian becomes

$$\tilde{\mathcal{H}} = \bar{E} + \frac{1}{2}\Psi^\dagger \mathcal{H}_M \Psi + O\left(S^{\frac{1}{2}}\right). \tag{B.33}$$

Here,

$$\bar{E} = 4JNS\left(S+1\right)\cos 2\theta - hN\left(2S+1\right)\cos\theta, \tag{B.34}$$

$$\Psi^\dagger = \left(a^\dagger,\ b^\dagger,\ a,\ b\right), \tag{B.35}$$

$$\mathcal{H}_M = \begin{pmatrix} 4JS+KS & 4JS\cos^2\theta & -KS & -4JS\sin^2\theta \\ 4JS\cos^2\theta & 4JS+KS & -4JS\sin^2\theta & -KS \\ -KS & -4JS\sin^2\theta & 4JS+KS & 4JS\cos^2\theta \\ -4JS\sin^2\theta & -KS & 4JS\cos^2\theta & 4JS+KS \end{pmatrix}. \tag{B.36}$$

The magnon energy ω_n is obtained by the secular equation

$$\Sigma^z \mathcal{H}_M \mathbf{u}_n = \omega_n \mathbf{u}_n, \tag{B.37}$$

where

$$\Sigma^z = \begin{pmatrix} 1 & 0 & 0 & 0 \\ 0 & 1 & 0 & 0 \\ 0 & 0 & -1 & 0 \\ 0 & 0 & 0 & -1 \end{pmatrix}. \tag{B.38}$$

The eigenvalues are obtained as:

$$\omega_1 = 8JS\cos\theta\sqrt{1+\frac{K}{4J}} = g\mu_{\mathrm{B}}\mu_0 H\sqrt{1+\frac{H_{\mathrm{A}}}{2H_{\mathrm{E}}}}, \tag{B.39}$$

$$\omega_2 = \sqrt{16JSKS\left(1-\cos^2\theta\right)} = g\mu_{\rm B}\mu_0\sqrt{2H_{\rm E}H_{\rm A}\left(1-\left(\frac{H}{2H_{\rm E}}\right)^2\right)}. \tag{B.40}$$

Here the exchange field $H_{\rm E}$ and the magnetic anisotropy field $H_{\rm A}$ are defined as

$$H_{\rm E} = \frac{4JS}{g\mu_{\rm B}\mu_0}, \quad H_{\rm A} = \frac{2KS}{g\mu_{\rm B}\mu_0}. \tag{B.41}$$

The diagonalized Hamiltonian is obtained by the Bogoliubov transformation

$$\begin{pmatrix} a \\ b \\ a^\dagger \\ b^\dagger \end{pmatrix} = \frac{1}{\sqrt{2}} \begin{pmatrix} \cosh\phi_2 & \cosh\phi_1 & -\sinh\phi_2 & \sinh\phi_1 \\ -\cosh\phi_2 & \cosh\phi_1 & \sinh\phi_2 & \sinh\phi_1 \\ -\sinh\phi_2 & \sinh\phi_1 & \cosh\phi_2 & \cosh\phi_1 \\ \sinh\phi_2 & \sinh\phi_1 & -\cosh\phi_2 & \cosh\phi_1 \end{pmatrix} \begin{pmatrix} \alpha \\ \beta \\ \alpha^\dagger \\ \beta^\dagger \end{pmatrix}, \tag{B.42}$$

where

$$\cosh\phi_2 = \sqrt{\frac{4JS\left(1-\cos^2\theta\right)+KS}{2\omega_2}+\frac{1}{2}}, \tag{B.43}$$

$$\sinh\phi_2 = \sqrt{\frac{4JS\left(1-\cos^2\theta\right)+KS}{2\omega_2}-\frac{1}{2}}, \quad \left(h \le 8JS\sqrt{1-\frac{K}{4J}}\right), \tag{B.44}$$

$$\cosh\phi_1 = \sqrt{\frac{4JS\left(1+\cos^2\theta\right)+KS}{2\omega_1}+\frac{1}{2}}, \tag{B.45}$$

$$\sinh\phi_1 = \sqrt{\frac{4JS\left(1+\cos^2\theta\right)+KS}{2\omega_1}-\frac{1}{2}}. \tag{B.46}$$

$$\tilde{\mathcal{H}} = \bar{E} + \omega_2\left(\alpha^\dagger\alpha+\frac{1}{2}\right) + \omega_1\left(\beta^\dagger\beta+\frac{1}{2}\right) + O\left(S^{\frac{1}{2}}\right), \tag{B.47}$$

With use of creation and annihilation operators, we can expressed $\mathbf{S}_{\rm A}$ and $\mathbf{S}_{\rm B}$ as

$$\mathbf{S}_{\rm A} = \mathbf{m}_{\rm A}S - \mathbf{m}_{\rm A}a^\dagger a + \sqrt{\frac{S}{2}}\left\{\frac{\partial\mathbf{m}_{\rm A}}{\partial\theta_{\rm A}}\left(a+a^\dagger\right) - i\hat{\mathbf{z}}\left(a-a^\dagger\right)\right\} + O\left(S^{-\frac{1}{2}}\right), \tag{B.48}$$

$$\mathbf{S}_{\rm B} = \mathbf{m}_{\rm B}S - \mathbf{m}_{\rm B}b^\dagger b + \sqrt{\frac{S}{2}}\left\{\frac{\partial\mathbf{m}_{\rm B}}{\partial\theta_{\rm B}}\left(b+b^\dagger\right) - i\hat{\mathbf{z}}\left(b-b^\dagger\right)\right\} + O\left(S^{-\frac{1}{2}}\right), \tag{B.49}$$

$$\mathbf{m}_{\rm A} = \left(\cos\theta_{\rm A}, \sin\theta_{\rm A}, 0\right), \quad \mathbf{m}_{\rm B} = \left(\cos\theta_{\rm B}, \sin\theta_{\rm B}, 0\right). \tag{B.50}$$

In the case of $\theta_{\rm H} = 0$,

$$\frac{\partial\mathbf{m}_{\rm A}}{\partial\theta_{\rm A}} = \begin{pmatrix} \sin\theta \\ -\cos\theta \\ 0 \end{pmatrix}, \quad \frac{\partial\mathbf{m}_{\rm B}}{\partial\theta_{\rm B}} = \begin{pmatrix} -\sin\theta \\ -\cos\theta \\ 0 \end{pmatrix}, \tag{B.51}$$

$$
\begin{aligned}
\mathbf{S}_{\mathrm{F}} &= \mathbf{S}_{\mathrm{A}} + \mathbf{S}_{\mathrm{B}} \\
&= \sqrt{\frac{S}{N}} \begin{pmatrix} \sin\theta \left(\cosh\phi_2 - \sinh\phi_2\right) \left(\alpha + \alpha^\dagger\right) \\ -\cos\theta \left(\cosh\phi_1 + \sinh\phi_1\right) \left(\beta + \beta^\dagger\right) \\ -i \left(\cosh\phi_1 - \sinh\phi_1\right) \left(\beta - \beta^\dagger\right) \end{pmatrix} \\
&\quad -2S \begin{pmatrix} \cos\theta \\ 0 \\ 0 \end{pmatrix} \\
&\quad + (\text{2nd order terms of } \alpha, \beta) + O\left(S^{-\frac{1}{2}}\right). \qquad \text{(B.52)}
\end{aligned}
$$

The dynamical and static components of $\mathbf{S}_{\mathrm{F}}$ ($\mathbf{S}_F^\omega$ and $\mathbf{S}_F^0$) are, respectively, expressed by the first and second terms as follows:

$$
\begin{aligned}
\mathbf{S}_F^\omega &= \sqrt{\frac{S}{N}} \begin{pmatrix} \sin\theta \left(\cosh\phi_2 - \sinh\phi_2\right) \left(\alpha + \alpha^\dagger\right) \\ -\cos\theta \left(\cosh\phi_1 + \sinh\phi_1\right) \left(\beta + \beta^\dagger\right) \\ -i \left(\cosh\phi_1 - \sinh\phi_1\right) \left(\beta - \beta^\dagger\right) \end{pmatrix}, \qquad \text{(B.53)} \\
\mathbf{S}_F^0 &= -2S \begin{pmatrix} \cos\theta \\ 0 \\ 0 \end{pmatrix}. \qquad \text{(B.54)}
\end{aligned}
$$

Similarly,

$$
\begin{aligned}
\mathbf{S}_{\mathrm{AF}} &= \mathbf{S}_{\mathrm{A}} - \mathbf{S}_{\mathrm{B}} \\
&= \sqrt{\frac{S}{N}} \begin{pmatrix} \sin\theta \left(\cosh\phi_1 + \sinh\phi_1\right) \left(\beta + \beta^\dagger\right) \\ -\cos\theta \left(\cosh\phi_2 - \sinh\phi_2\right) \left(\alpha + \alpha^\dagger\right) \\ -i \left(\cosh\phi_2 + \sinh\phi_2\right) \left(\alpha - \alpha^\dagger\right) \end{pmatrix} \\
&\quad -2S \begin{pmatrix} 0 \\ \sin\theta \\ 0 \end{pmatrix} \\
&\quad + (\text{2nd order terms of } \alpha, \beta) + O\left(S^{-\frac{1}{2}}\right). \qquad \text{(B.55)}
\end{aligned}
$$

The dynamical and static components of $\mathbf{S}_{\rm AF}$ ($\mathbf{S}^{\omega}_{AF}$ and $\mathbf{S}^{0}_{AF}$) are, respectively, defined by the first and second terms as follows:

$$\mathbf{S}^{\omega}_{AF} = \sqrt{\frac{S}{N}} \begin{pmatrix} \sin\theta \left(\cosh\phi_1 + \sinh\phi_1\right) \left(\beta + \beta^{\dagger}\right) \\ -\cos\theta \left(\cosh\phi_2 - \sinh\phi_2\right) \left(\alpha + \alpha^{\dagger}\right) \\ -i \left(\cosh\phi_2 + \sinh\phi_2\right) \left(\alpha - \alpha^{\dagger}\right) \end{pmatrix}, \tag{B.56}$$

$$\mathbf{S}^{0}_{AF} = -2S \begin{pmatrix} 0 \\ \sin\theta \\ 0 \end{pmatrix}. \tag{B.57}$$

In the case of $\theta_{\rm H} = 3\pi/4$,

$$\frac{\partial \mathbf{m}_{\rm A}}{\partial \theta_{\rm A}} = \frac{1}{\sqrt{2}} \begin{pmatrix} \cos\theta - \sin\theta \\ \cos\theta + \sin\theta \\ 0 \end{pmatrix}, \quad \frac{\partial \mathbf{m}_{\rm B}}{\partial \theta_{\rm B}} = \frac{1}{\sqrt{2}} \begin{pmatrix} \cos\theta + \sin\theta \\ \cos\theta - \sin\theta \\ 0 \end{pmatrix}, \tag{B.58}$$

$$\begin{aligned} \mathbf{S}_{\rm F} &= \sqrt{\frac{S}{2N}} \times \\ &\begin{pmatrix} -\sin\theta \left(\cosh\phi_2 - \sinh\phi_2\right) \left(\alpha + \alpha^{\dagger}\right) + \cos\theta \left(\cosh\phi_1 + \sinh\phi_1\right) \left(\beta + \beta^{\dagger}\right) \\ \sin\theta \left(\cosh\phi_2 - \sinh\phi_2\right) \left(\alpha + \alpha^{\dagger}\right) + \cos\theta \left(\cosh\phi_1 + \sinh\phi_1\right) \left(\beta + \beta^{\dagger}\right) \\ -\sqrt{2}i \left(\cosh\phi_1 - \sinh\phi_1\right) \left(\beta - \beta^{\dagger}\right) \end{pmatrix} \\ &+\sqrt{2}S\cos\theta \begin{pmatrix} 1 \\ -1 \\ 0 \end{pmatrix} \\ &+ (\text{2nd order terms of } \alpha, \beta) + O\left(S^{-\frac{1}{2}}\right), \end{aligned} \tag{B.59}$$

$$\begin{aligned} \mathbf{S}_{\rm AF} &= \sqrt{\frac{S}{2N}} \times \\ &\begin{pmatrix} \cos\theta \left(\cosh\phi_2 - \sinh\phi_2\right) \left(\alpha + \alpha^{\dagger}\right) - \sin\theta \left(\cosh\phi_1 + \sinh\phi_1\right) \left(\beta + \beta^{\dagger}\right) \\ \cos\theta \left(\cosh\phi_2 - \sinh\phi_2\right) \left(\alpha + \alpha^{\dagger}\right) + \sin\theta \left(\cosh\phi_1 + \sinh\phi_1\right) \left(\beta + \beta^{\dagger}\right) \\ -\sqrt{2}i \left(\cosh\phi_2 + \sinh\phi_2\right) \left(\alpha - \alpha^{\dagger}\right) \end{pmatrix} \\ &+\sqrt{2}S\sin\theta \begin{pmatrix} 1 \\ 1 \\ 0 \end{pmatrix}. \end{aligned} \tag{B.60}$$

B.4 Microwave non-reciprocity

B.4.1 Dynamical Susceptibility tensors

In this section, we discuss dynamical susceptibility tensors for the estimation of microwave non-reciprocity in the later section. For the magnetoelectric substance, the oscillating electric and magnetic flux densities ($\mathbf{D}^\omega = (D_x^\omega, D_y^\omega, D_z^\omega), \mathbf{B}^\omega = (B_x^\omega, B_y^\omega, B_z^\omega)$) in oscillating electric and magnetic fields ($\mathbf{E}^\omega = (E_x^\omega, E_y^\omega, E_z^\omega)$, $\mathbf{H}^\omega = (H_x^\omega, H_y^\omega, H_z^\omega)$) can be expressed as:

$$D_i^\omega = \varepsilon_0(\varepsilon_\infty + \chi_{ij}^{ee})E_j^\omega + \sqrt{\varepsilon_0\mu_0}\chi_{ij}^{em}H_j, \tag{B.61}$$

$$B_i^\omega = \mu_0(1 + \chi_{ij}^{mm})H_j^\omega + \sqrt{\varepsilon_0\mu_0}\chi_{ij}^{me}E_j, \tag{B.62}$$

where χ^{mm}, χ^{ee}, χ^{em} and χ^{me} are magnetic, electric, electromagnetic, and magnetoelectric dynamical tensors, respectively. ε_0 is the permittivity in vacuum. ε_∞ is the relative permittivity at high frequency. According to ref. [116], $\varepsilon_\infty \approx 14$. The nonzero component of these dynamical susceptibility tensors can be determined by the symmetry analysis[114, 115]. Let us discuss them under $\mathbf{H} \parallel [100]$ and $\mathbf{H} \parallel [1\bar{1}0]$ corresponding to the experiments. The magnetic point groups are $22'2'$ and $m'm2'$ for $\mathbf{H} \parallel [100]$ and $\mathbf{H} \parallel [1\bar{1}0]$, respectively. Therefore, for $\mathbf{H} \parallel [100]$,

$$\chi^{mm} = \begin{pmatrix} \chi_{xx}^{mm} & 0 & 0 \\ 0 & \chi_{yy}^{mm} & \chi_{yz}^{mm} \\ 0 & -\chi_{yz}^{mm} & \chi_{zz}^{mm} \end{pmatrix}, \quad \chi^{ee} = \begin{pmatrix} \chi_{xx}^{ee} & 0 & 0 \\ 0 & \chi_{yy}^{ee} & \chi_{yz}^{ee} \\ 0 & -\chi_{yz}^{ee} & \chi_{zz}^{ee} \end{pmatrix},$$

$$\chi^{me} = \begin{pmatrix} \chi_{xx}^{me} & 0 & 0 \\ 0 & \chi_{yy}^{me} & \chi_{yz}^{me} \\ 0 & \chi_{zy}^{me} & \chi_{zz}^{me} \end{pmatrix}, \quad \chi^{em} = \begin{pmatrix} -\chi_{xx}^{me} & 0 & 0 \\ 0 & -\chi_{yy}^{me} & \chi_{zy}^{me} \\ 0 & \chi_{yz}^{me} & -\chi_{zz}^{me} \end{pmatrix}, \tag{B.63}$$

where $\mathbf{x} \parallel [100], \mathbf{y} \parallel [010]$ and $\mathbf{z} \parallel [001]$. For $\mathbf{H} \parallel [1\bar{1}0]$,

$$\chi^{mm} = \begin{pmatrix} \chi_{xx}^{mm} & 0 & \chi_{xz}^{mm} \\ 0 & \chi_{yy}^{mm} & 0 \\ -\chi_{xz}^{mm} & 0 & \chi_{zz}^{mm} \end{pmatrix}, \quad \chi^{ee} = \begin{pmatrix} \chi_{xx}^{ee} & 0 & \chi_{xz}^{ee} \\ 0 & \chi_{yy}^{ee} & 0 \\ -\chi_{xz}^{ee} & 0 & \chi_{zz}^{ee} \end{pmatrix},$$

$$\chi^{me} = \begin{pmatrix} 0 & 0 & \chi_{xz}^{me} \\ 0 & 0 & \chi_{yz}^{me} \\ \chi_{zx}^{me} & \chi_{zy}^{me} & 0 \end{pmatrix}, \quad \chi^{em} = \begin{pmatrix} 0 & 0 & -\chi_{zx}^{me} \\ 0 & 0 & \chi_{zy}^{me} \\ -\chi_{xz}^{me} & \chi_{yz}^{me} & 0 \end{pmatrix}, \tag{B.64}$$

where $\mathbf{x} \parallel [110], \mathbf{y} \parallel [001]$ and $\mathbf{z} \parallel [1\bar{1}0]$.

The dynamical susceptibility tensors at $T = 0$ are obtained by the Kubo formula as follows;

$$\chi^{me}_{\beta\gamma} = \frac{NV}{\hbar}\sqrt{\frac{\mu_0}{\varepsilon_0}}\sum_n \frac{\langle 0\,|\Delta M_\beta|\,n\rangle\,\langle n\,|\Delta P_\gamma|\,0\rangle}{\omega - \omega_n + i\delta}, \tag{B.65}$$

$$\chi^{em}_{\beta\gamma} = \frac{NV}{\hbar}\sqrt{\frac{\mu_0}{\varepsilon_0}}\sum_n \frac{\langle 0\,|\Delta P_\beta|\,n\rangle\,\langle n\,|\Delta M_\gamma|\,0\rangle}{\omega - \omega_n + i\delta}, \tag{B.66}$$

$$\chi^{mm}_{\beta\gamma} = \frac{NV}{\hbar}\mu_0\sum_n \frac{\langle 0\,|\Delta M_\beta|\,n\rangle\,\langle n\,|\Delta M_\gamma|\,0\rangle}{\omega - \omega_n + i\delta}, \tag{B.67}$$

$$\chi^{ee}_{\beta\gamma} = \frac{NV}{\hbar}\frac{1}{\varepsilon_0}\sum_n \frac{\langle 0\,|\Delta P_\beta|\,n\rangle\,\langle n\,|\Delta P_\gamma|\,0\rangle}{\omega - \omega_n + i\delta}, \tag{B.68}$$

where $|0\rangle$ is the ground state and $|n\rangle$ is the magnon excited state. Here, $\Delta\mathbf{M}$ and $\Delta\mathbf{P}$ are, respectively, the dynamical polarization and magnetization induced by the magnons expressed as follows;

$$\Delta\mathbf{M} = -\frac{1}{2NV}\sum_i^{2N} g\mu_{\mathrm{B}}\Delta\mathbf{S}_i \simeq -\frac{1}{V}g\mu_{\mathrm{B}}\mathbf{S}^\omega_{\mathrm{F}}, \tag{B.69}$$

$$\begin{aligned}\Delta\mathbf{P} &= \frac{\lambda}{NV}\sum_i^{2N}\sum_j^{4}(\mathbf{S}_i\cdot\mathbf{e}_{ij})(\Delta\mathbf{S}_i\cdot\mathbf{e}_{ij})\,\mathbf{e}_{ij} \\ &= \frac{4dfl\lambda}{V}\begin{pmatrix} S^0_{\mathrm{F},y}S^\omega_{\mathrm{F},z} + S^\omega_{\mathrm{F},y}S^0_{\mathrm{F},z} + S^0_{\mathrm{AF},y}S^\omega_{\mathrm{AF},z} + S^\omega_{\mathrm{AF},y}S^0_{\mathrm{AF},z} \\ S^0_{\mathrm{F},x}S^\omega_{\mathrm{F},z'} + S^\omega_{\mathrm{F},x}S^0_{\mathrm{F},z'} + S^0_{\mathrm{AF},x}S^\omega_{\mathrm{AF},z'} + S^\omega_{\mathrm{AF},x}S^0_{\mathrm{AF},z} \\ S^0_{\mathrm{F},x}S^\omega_{\mathrm{F},y} + S^\omega_{\mathrm{F},x}S^0_{\mathrm{F},y} + S^0_{\mathrm{AF},x}S^\omega_{\mathrm{AF},y} + S^\omega_{\mathrm{AF},x}S^0_{\mathrm{AF},y} \end{pmatrix}.\end{aligned} \tag{B.70}$$

B.4.2 Microwave non-reciprocity in coplanar waveguide

In order to theoretically obtain the microwave non-reciprocity, we should estimate the damping rate of microwave in the microwave coplanar waveguide with sample. We assume that $x'y'z'$-coordinate is fixed to the microwave wave guide. The x'-direction is along the microwave propagation direction. y' is parallel to the coplanar pattern but perpendicular to x'. The z' direction is perpendicular to the coplanar pattern. In our experimental setup, the microwave is composed of two linearly polarized waves (polarization 1: $\mathbf{E}^\omega \parallel \mathbf{z}'$, $\mathbf{H}^\omega \parallel \mathbf{y}'$) and

(polarization 2: $\mathbf{E}^\omega \parallel \mathbf{y}'$, $\mathbf{H}^\omega \parallel \mathbf{z}'$). For simplicity, we assume the two polarizations are equally mixed. We also assume that the linear polarization is approximately maintained in the substance. In order to estimate the refractive index for the polarization 1 ($\mathbf{E}^\omega \parallel \mathbf{z}', \mathbf{H}^\omega \parallel \mathbf{y}'$), We put $E^\omega_{x'} = E^\omega_{y'} = H^\omega_{x'} = H^\omega_{z'} = 0$, $E^\omega_{z'} = |E^\omega_{z'}| \exp[i(kx' - \omega t)]$, $H^\omega_{y'} = \left|H^\omega_{y'}\right| \exp[i(kx' - \omega t)]$ into the Maxwell equations, and obtain

$$-kE^\omega_{z'} = \omega \left\{ \left(1 + \chi^{mm}_{y'y'}\right) \mu_0 H^\omega_{y'} + \chi^{me}_{y'z'} \sqrt{\varepsilon_0 \mu_0} E^\omega_{z'} \right\}, \tag{B.71}$$

$$kH^\omega_{y'} = -\omega \left\{ \left(\varepsilon_\infty + \chi^{ee}_{z'z'}\right) \varepsilon_0 E^\omega_{z'} + \chi^{em}_{z'y'} \sqrt{\varepsilon_0 \mu_0} H^\omega_{y'} \right\}. \tag{B.72}$$

From the requirement of existence of solution other than $E^\omega_z = H^\omega_y = 0$, we get

$$k = \omega \sqrt{\varepsilon_0 \mu_0} \left(-\frac{\chi^{me}_{y'z'} + \chi^{em}_{z'y'}}{2} \pm \sqrt{\left(\varepsilon_\infty + \chi^{ee}_{z'z'}\right)\left(1 + \chi^{mm}_{y'y'}\right)} \right). \tag{B.73}$$

The magnitude of second term is much larger than that of first term. Therefore, the upper sign is corresponding to the $k > 0$ solution while the lower sign to the $k < 0$ solution. The difference of refractive indices n for positive and negative k is

$$\Delta n = -\left(\chi^{me}_{y'z'} + \chi^{em}_{z'y'}\right). \tag{B.74}$$

The average of refractive indices is

$$\bar{n} = \sqrt{\left(\varepsilon_\infty + \chi^{ee}_{z'z'}\right)\left(1 + \chi^{mm}_{y'y'}\right)}. \tag{B.75}$$

Because the absorption coefficient α is expressed as $\omega \mathrm{Im}[n]/c$, the difference of absorption coefficient is

$$\Delta\alpha_1 = -\frac{\omega}{c} \mathrm{Im}\left[\chi^{me}_{y'z'} + \chi^{em}_{z'y'}\right], \tag{B.76}$$

and the average of absorption coefficient is

$$\bar{\alpha}_1 = \frac{\omega}{c} \mathrm{Im}\left[\sqrt{\left(\varepsilon_\infty + \chi^{ee}_{z'z'}\right)\left(1 + \chi^{mm}_{y'y'}\right)}\right]. \tag{B.77}$$

The suffix "1" stands for the first polarization ($\mathbf{E}^\omega \parallel \mathbf{z}$, $\mathbf{H}^\omega \parallel \mathbf{y}$).

On the other hand, for the polarization $\mathbf{E}^\omega \parallel \mathbf{y}', \mathbf{H}^\omega \parallel \mathbf{z}'$ (polarization 2), the microwave non-reciprocity and the average of microwave absorption are, respectively,

$$\Delta\alpha_2 = \frac{\omega}{c} \mathrm{Im}\left[\chi^{me}_{z'y'} + \chi^{em}_{y'z'}\right], \tag{B.78}$$

$$\bar{\alpha}_2 = \frac{\omega}{c} \mathrm{Im}\left[\sqrt{\left(\varepsilon_\infty + \chi^{ee}_{y'y'}\right)\left(1 + \chi^{mm}_{z'z'}\right)}\right]. \tag{B.79}$$

We assume the relative magnitude of the microwave non-reciprocity in our experiment is corresponding to

$$\frac{\Delta\alpha}{\bar{\alpha}} \simeq \frac{\Delta\alpha_1 + \Delta\alpha_2}{\bar{\alpha}_1 + \bar{\alpha}_2}. \tag{B.80}$$

The microwave absorption spectrum is obtained from the absorption coefficients as follows;

$$\Delta S_{12} + \Delta S_{21} = -2\bar{\alpha}L \times 20\log_{10} e, \tag{B.81}$$

$$\Delta S_{12} - \Delta S_{21} = -\Delta\alpha L \times 20\log_{10} e. \tag{B.82}$$

Here L is the propagation length of microwave in a sample. Thus the relative magnitude of the microwave non-reciprocity is equivalent to the experimental value.

$$2\frac{\Delta S_{12} - \Delta S_{21}}{\Delta S_{12} + \Delta S_{21}} = \frac{\Delta\alpha}{\bar{\alpha}} \tag{B.83}$$

B.4.3 Microwave non-reciprocity for $\mathbf{H} \parallel [100]$ and $\mathbf{H}^{\omega} \perp [100]$

In this subsection, we theoretically estimate the non-reciprocity for $\mathbf{H} \parallel [100]$, $\mathbf{H}^{\omega} \perp [100]$. The real and imaginary part of the dynamical susceptibilities are

expressed as follows:

$$\mathrm{Im}\left[\chi^{me}_{y'z'}+\chi^{em}_{z'y'}\right] = \frac{NV}{\hbar}\sqrt{\frac{\mu_0}{\varepsilon_0}}\sum_n \frac{-2\delta\left\langle 0\left|\Delta M_{y'}\right|n\right\rangle\left\langle n\left|\Delta P'_z\right|0\right\rangle}{\left(\omega-\omega_n\right)^2+\delta^2}, \quad \text{(B.84)}$$

$$\mathrm{Im}\left[\chi^{me}_{z'y'}+\chi^{em}_{y'z'}\right] = \frac{NV}{\hbar}\sqrt{\frac{\mu_0}{\varepsilon_0}}\sum_n \frac{-2\delta\left\langle 0\left|\Delta M_{z'}\right|n\right\rangle\left\langle n\left|\Delta P'_y\right|0\right\rangle}{\left(\omega-\omega_n\right)^2+\delta^2}, \quad \text{(B.85)}$$

$$\mathrm{Im}\left[\chi^{ee}_{z'z'}\right] = \frac{NV}{\hbar}\frac{1}{\varepsilon_0}\sum_n \frac{-\delta\left\langle 0\left|\Delta P'_z\right|n\right\rangle\left\langle n\left|\Delta P'_z\right|0\right\rangle}{\left(\omega-\omega_n\right)^2+\delta^2}, \quad \text{(B.86)}$$

$$\mathrm{Re}\left[\chi^{ee}_{z'z'}\right] = \frac{NV}{\hbar}\frac{1}{\varepsilon_0}\sum_n \frac{\left(\omega-\omega_n\right)\left\langle 0\left|\Delta P'_z\right|n\right\rangle\left\langle n\left|\Delta P'_z\right|0\right\rangle}{\left(\omega-\omega_n\right)^2+\delta^2}, \quad \text{(B.87)}$$

$$\mathrm{Im}\left[\chi^{ee}_{y'y'}\right] = \frac{NV}{\hbar}\frac{1}{\varepsilon_0}\sum_n \frac{-\delta\left\langle 0\left|\Delta P'_y\right|n\right\rangle\left\langle n\left|\Delta P'_y\right|0\right\rangle}{\left(\omega-\omega_n\right)^2+\delta^2}, \quad \text{(B.88)}$$

$$\mathrm{Re}\left[\chi^{ee}_{y'y'}\right] = \frac{NV}{\hbar}\frac{1}{\varepsilon_0}\sum_n \frac{\left(\omega-\omega_n\right)\left\langle 0\left|\Delta P'_y\right|n\right\rangle\left\langle n\left|\Delta P'_y\right|0\right\rangle}{\left(\omega-\omega_n\right)^2+\delta^2}, \quad \text{(B.89)}$$

$$\mathrm{Im}\left[\chi^{mm}_{y'y'}\right] = \frac{NV}{\hbar}\mu_0\sum_n \frac{-\delta\left\langle 0\left|\Delta M_{y'}\right|n\right\rangle\left\langle n\left|\Delta M_{y'}\right|0\right\rangle}{\left(\omega-\omega_n\right)^2+\delta^2}, \quad \text{(B.90)}$$

$$\mathrm{Re}\left[\chi^{mm}_{y'y'}\right] = \frac{NV}{\hbar}\mu_0\sum_n \frac{\left(\omega-\omega_n\right)\left\langle 0\left|\Delta M_{y'}\right|n\right\rangle\left\langle n\left|\Delta M_{y'}\right|0\right\rangle}{\left(\omega-\omega_n\right)^2+\delta^2}, \quad \text{(B.91)}$$

$$\mathrm{Im}\left[\chi^{mm}_{z'z'}\right] = \frac{NV}{\hbar}\mu_0\sum_n \frac{-\delta\left\langle 0\left|\Delta M_{z'}\right|n\right\rangle\left\langle n\left|\Delta M_{z'}\right|0\right\rangle}{\left(\omega-\omega_n\right)^2+\delta^2}, \quad \text{(B.92)}$$

$$\mathrm{Re}\left[\chi^{mm}_{z'z'}\right] = \frac{NV}{\hbar}\mu_0\sum_n \frac{\left(\omega-\omega_n\right)\left\langle 0\left|\Delta M_{z'}\right|n\right\rangle\left\langle n\left|\Delta M_{z'}\right|0\right\rangle}{\left(\omega-\omega_n\right)^2+\delta^2}. \quad \text{(B.93)}$$

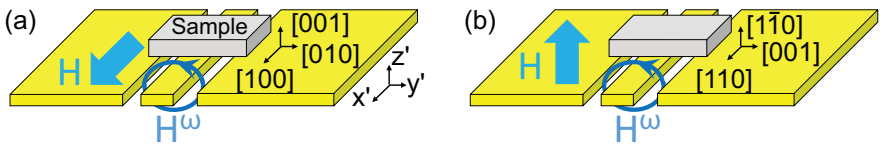

Figure B.3: (a),(b) Experimental setups for the microwave non-reciprocity measurements (a) for $\mathbf{H} \parallel [100]$, $\mathbf{H}^\omega \perp [100]$ and (b) for $\mathbf{H} \parallel [1\bar{1}0]$, $\mathbf{H}^\omega \perp [110]$.

The matrix elements of $\Delta\mathbf{M}$ and $\Delta\mathbf{P}$ are

$$\langle 0\,|\Delta M_{y'}|\,\alpha\rangle = \langle\alpha\,|\Delta M_{y'}|\,0\rangle = 0, \tag{B.94}$$

$$\langle 0\,|\Delta M_{y'}|\,\beta\rangle = \langle\beta\,|\Delta M_{y'}|\,0\rangle = \frac{g\mu_{\rm B}}{V}\sqrt{\frac{S}{N}}\cos\theta\,(\cosh\phi_1+\sinh\phi_1)\,, \tag{B.95}$$

$$\langle 0\,|\Delta M_{z'}|\,\alpha\rangle = \langle\alpha\,|\Delta M_{z'}|\,0\rangle = 0, \tag{B.96}$$

$$\langle 0\,|\Delta M_{z'}|\,\beta\rangle = -\langle\beta\,|\Delta M_{z'}|\,0\rangle = i\frac{g\mu_{\rm B}}{V}\sqrt{\frac{S}{N}}\,(\cosh\phi_1-\sinh\phi_1)\,, \tag{B.97}$$

$$\langle 0\,|\Delta P_{y'}|\,\alpha\rangle = \langle\alpha\,|\Delta P_{y'}|\,0\rangle = 0, \tag{B.98}$$

$$\langle 0\,|\Delta P_{y'}|\,\beta\rangle = -\langle\beta\,|\Delta P_{y'}|\,0\rangle = i\frac{8dflS\lambda}{V}\sqrt{\frac{S}{N}}\cos\theta\,(\cosh\phi_1-\sinh\phi_1)\,, \tag{B.99}$$

$$\langle 0\,|\Delta P_{z'}|\,\alpha\rangle = \langle\alpha\,|\Delta P_{z'}|\,0\rangle = 0, \tag{B.100}$$

$$\langle 0\,|\Delta P_{z'}|\,\beta\rangle = \langle\beta\,|\Delta P_{z'}|\,0\rangle = \frac{8dflS\lambda}{V}\sqrt{\frac{S}{N}}(2\cos^2\theta-1)\,(\cosh\phi_1+\sinh\phi_1)\,, \tag{B.101}$$

where $|\alpha\rangle = \alpha^\dagger\,|0\rangle$ and $|\beta\rangle = \beta^\dagger\,|0\rangle$. At $\omega=\omega_2$ $(n=\alpha)$, the microwave absorption is zero. The relative microwave non-reciprocity at $\omega=\omega_1$ $(n=\beta)$ is

$$\frac{\Delta\alpha}{\bar{\alpha}} = \frac{16dflS^2\lambda g\mu_{\rm B}}{V\hbar\delta}\sqrt{\frac{\mu_0}{\varepsilon_0}}\left\{\cos\theta\left(2\cos^2\theta-1\right)(\cosh\phi_1+\sinh\phi_1)^2-\cos\theta\,(\cosh\phi_1-\sinh\phi_1)^2\right\}$$
$$\times\ \sqrt{2}\left\{\frac{Y_1}{\sqrt{X_1+\sqrt{X_1^2+Y_1^2}}}+\frac{Y_2}{\sqrt{X_2+\sqrt{X_2^2+Y_2^2}}}\right\}^{-1}, \tag{B.102}$$

where

$$X_1 = \varepsilon_\infty-\left(\frac{8dflS^2g\mu_{\rm B}\lambda}{\hbar V\delta}\right)^2\frac{\mu_0}{\varepsilon_0}\left(2\cos^2\theta-1\right)^2\cos^2\theta\,(\cosh\phi_1+\sinh\phi_1)^4\,, \tag{B.103}$$

$$X_2 = \varepsilon_\infty-\left(\frac{8dflS^2g\mu_{\rm B}\lambda}{\hbar V\delta}\right)^2\frac{\mu_0}{\varepsilon_0}\cos^2\theta\,(\cosh\phi_1-\sinh\phi_1)^4\,, \tag{B.104}$$

$$Y_1 = \frac{\left(8dflS^{\frac{3}{2}}\lambda\right)^2}{\hbar V\varepsilon_0\delta}\left(2\cos^2\theta-1\right)^2(\cosh\phi_1+\sinh\phi_1)^2+\varepsilon_\infty\frac{\mu_0g\mu_{\rm B}^2S}{\hbar V\delta}\cos^2\theta\,(\cosh\phi_1+\sinh\phi_1)^2\,, \tag{B.105}$$

$$Y_2 = \frac{\left(8dflS^{\frac{3}{2}}\lambda\right)^2}{\hbar V\varepsilon_0\delta}\cos^2\theta\,(\cosh\phi_1-\sinh\phi_1)^2+\varepsilon_\infty\frac{\mu_0g\mu_{\rm B}^2S}{\hbar V\delta}\,(\cosh\phi_1-\sinh\phi_1)^2\,. \tag{B.106}$$

The magnetic field dependence at ω_1 is plotted in Fig. B.4(a). Here the value of δ was estimated as $\delta = 1.4$ GHz by the comparison of measured and calculated absorption spectra.

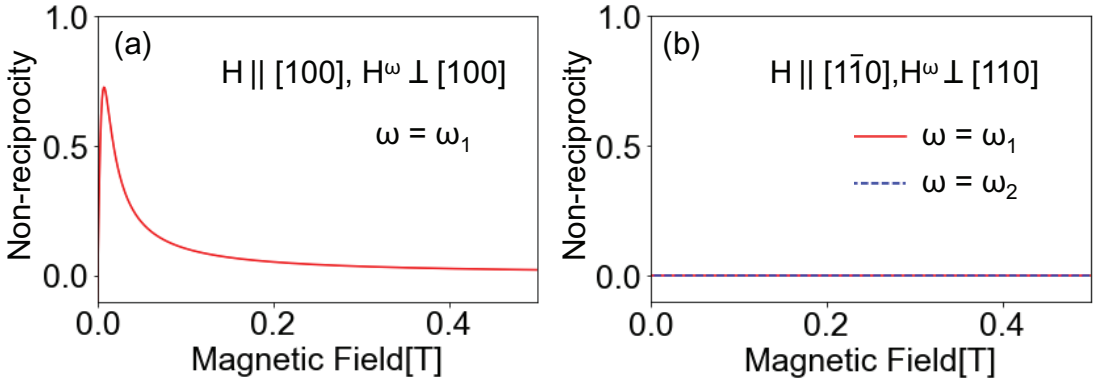

Figure B.4: (a),(b) Relative microwave non-reciprocity $\Delta\alpha/2\bar{\alpha} = (\Delta S_{12} - \Delta S_{21}) / (\Delta S_{12} + \Delta S_{21})$ (a) at $\omega = \omega_1$ for $\mathbf{H} \parallel [100]$, $\mathbf{H}^{\omega} \perp [100]$ and (b) for $\mathbf{H} \parallel [1\bar{1}0]$, $\mathbf{H}^{\omega} \perp [110]$ at $\omega = \omega_1$ (solid line) and $\omega = \omega_2$ (dashed line).

B.4.4 Microwave non-reciprocity for $\mathbf{H} \parallel [1\bar{1}0]$, $\mathbf{H}^{\omega} \perp [110]$

For $\mathbf{H} \parallel [1\bar{1}0]$ and $\mathbf{H}^{\omega} \perp [110]$, the matrix elements of $\Delta\mathbf{M}$ and $\Delta\mathbf{P}$ are

$$\langle 0 |\Delta M_{y'}| \alpha\rangle = \langle \alpha |\Delta M_{y'}| 0\rangle = 0, \tag{B.107}$$

$$\langle 0 |\Delta M_{y'}| \beta\rangle = -\langle \beta |\Delta M_{y'}| 0\rangle = i\frac{g\mu_{\mathrm{B}}}{V}\sqrt{\frac{S}{N}}\left(\cosh\phi_1 - \sinh\phi_1\right), \tag{B.108}$$

$$\langle 0 |\Delta M_{z'}| \alpha\rangle = \langle \alpha |\Delta M_{z'}| 0\rangle = \frac{g\mu_{\mathrm{B}}}{V}\sqrt{\frac{S}{N}}\sin\theta\left(\cosh\phi_2 - \sinh\phi_2\right), \tag{B.109}$$

$$\langle 0 |\Delta M_{z'}| \beta\rangle = \langle \beta |\Delta M_{z'}| 0\rangle = 0, \tag{B.110}$$

$$\langle 0 |\Delta P_{y'}| \alpha\rangle = \langle \alpha |\Delta P_{y'}| 0\rangle = \frac{16dflS\lambda}{V}\sqrt{\frac{S}{N}}\sin\theta\cos\theta\left(\cosh\phi_2 - \sinh\phi_2\right), \tag{B.111}$$

$$\langle 0 |\Delta P_{y'}| \beta\rangle = \langle \beta |\Delta P_{y'}| 0\rangle = 0, \tag{B.112}$$

$$\langle 0 |\Delta P_{z'}| \alpha\rangle = \langle \alpha |\Delta P_{z'}| 0\rangle = 0, \tag{B.113}$$

$$\langle 0 |\Delta P_{z'}| \beta\rangle = -\langle \beta |\Delta P_{z'}| 0\rangle = i\frac{8dflS\lambda}{V}\sqrt{\frac{S}{N}}\cos\theta\left(\cosh\phi_1 - \sinh\phi_1\right) \tag{B.114}$$

The relative microwave non-reciprocity at $\omega = \omega_1$ $(n = \beta)$ is

$$\begin{aligned}\frac{\Delta\alpha}{\bar{\alpha}} &= \frac{16dflS^2\lambda g\mu_{\rm B}}{V\hbar}\sqrt{\frac{\mu_0}{\varepsilon_0}}\cos\theta\left\{\frac{\delta}{(\omega_2-\omega_1)^2+\delta^2}\left(\cosh\phi_2-\sinh\phi_2\right)^2\right.\\ &\quad\left.+\frac{2\sin^2\theta}{\delta}\left(\cosh\phi_1-\sinh\phi_1\right)^2\right\}\\ &\times\ \sqrt{2}\left\{\frac{Y_1}{\sqrt{X_1+\sqrt{X_1^2+Y_1^2}}}+\frac{Y_2}{\sqrt{X_2+\sqrt{X_2^2+Y_2^2}}}\right\}^{-1}, \qquad \text{(B.115)}\end{aligned}$$

where

$$X_1 = \varepsilon_\infty - \frac{\mu_0}{\varepsilon_0}\left(\frac{8dflS^2\lambda g\mu_{\rm B}}{\hbar V}\right)^2\frac{1}{\delta^2}\cos^2\theta\left(\cosh\phi_1-\sinh\phi_1\right)^4, \qquad \text{(B.116)}$$

$$\begin{aligned}X_2 &= \varepsilon_\infty+\varepsilon_\infty\frac{\left(g\mu_{\rm B}\right)^2 S\mu_0}{\hbar V}\frac{\omega_2-\omega_1}{(\omega_2-\omega_1)^2+\delta^2}\sin^2\theta\left(\cosh\phi_2-\sinh\phi_2\right)^2\\ &\quad+\frac{\left(16dfl\lambda\right)^2 S^3}{\hbar V\varepsilon_0}\frac{\omega_1-\omega_2}{(\omega_1-\omega_2)^2+\delta^2}\cos^2\theta\left(\cosh\phi_2-\sinh\phi_2\right)^2\\ &\quad-\frac{\mu_0}{\varepsilon_0}\left(\frac{16dflS^2\lambda g\mu_{\rm B}}{\hbar V}\right)^2\left(\frac{\delta}{(\omega_1-\omega_2)^2+\delta^2}\right)^2\sin^4\theta\cos^2\theta\left(\cosh\phi_2-\sinh\phi_2\right)^4, \qquad \text{(B.117)}\end{aligned}$$

$$\begin{aligned}Y_1 &= \frac{\left(8dfl\lambda\right)^2 S^3}{\hbar V\varepsilon_0}\frac{\cos^2\theta}{\delta}\left(\cosh\phi_1-\sinh\phi_1\right)^2\\ &\quad+\varepsilon_\infty\frac{\mu_0 g^2\mu_{\rm B}^2 S}{\hbar V}\frac{1}{\delta}\left(\cosh\phi_1-\sinh\phi_1\right)^2, \qquad \text{(B.118)}\end{aligned}$$

$$\begin{aligned}Y_2 &= \varepsilon_\infty\frac{(g\mu_{\rm B})^2\mu_0 S}{\hbar V}\frac{\delta\sin^2\theta}{(\omega_1-\omega_2)^2+\delta^2}\left(\cosh\phi_2-\sinh\phi_2\right)^2\\ &\quad+\frac{S^3(16dfl\lambda)^2}{\hbar V\varepsilon_0\delta}\frac{\delta\sin^2\theta\cos^2\theta}{(\omega_1-\omega_2)^2+\delta^2}\left(\cosh\phi_2-\sinh\phi_2\right)^2\\ &\quad+2\frac{\mu_0}{\varepsilon_0}\left(\frac{g\mu_{\rm B}8dflS^2\lambda}{\hbar V}\right)^2\cos^2\theta\frac{\delta(\omega_1-\omega_2)}{(\omega_1-\omega_2)^2+\delta^2}\left(\cosh\phi_1-\sinh\phi_1\right)^4. \qquad \text{(B.119)}\end{aligned}$$

The relative microwave non-reciprocity at $\omega = \omega_2$ $(n = \alpha)$ is

$$\begin{aligned}\frac{\Delta\alpha}{\bar{\alpha}} &= \frac{16dflS^2\lambda g\mu_{\rm B}}{V\hbar}\sqrt{\frac{\mu_0}{\varepsilon_0}}\cos\theta\left\{\frac{2\sin^2\theta}{\delta}\left(\cosh\phi_2-\sinh\phi_2\right)^2\right.\\ &\quad\left.+\frac{\delta}{(\omega_2-\omega_1)^2+\delta^2}\left(\cosh\phi_1-\sinh\phi_1\right)^2\right\}\\ &\times\ \sqrt{2}\left\{\frac{Y_1}{\sqrt{X_1+\sqrt{X_1^2+Y_1^2}}}+\frac{Y_2}{\sqrt{X_2+\sqrt{X_2^2+Y_2^2}}}\right\}^{-1}, \qquad \text{(B.120)}\end{aligned}$$

where

$$
\begin{aligned}
X_1 &= \varepsilon_\infty + \varepsilon_\infty \frac{(g\mu_{\rm B})^2 S\mu_0}{\hbar V} \frac{\omega_2-\omega_1}{(\omega_2-\omega_1)^2+\delta^2} \sin^2\theta \left(\cosh\phi_2 - \sinh\phi_2\right)^2 \\
&\quad + \frac{(8dfl\lambda)^2 S^3}{\hbar V \varepsilon_0} \frac{\omega_2-\omega_1}{(\omega_2-\omega_1)^2+\delta^2} \cos^2\theta \left(\cosh\phi_1 - \sinh\phi_1\right)^2 \\
&\quad - \frac{\mu_0}{\varepsilon_0} \left(\frac{8dflS^2\lambda g\mu_{\rm B}}{\hbar V}\right)^2 \left(\frac{\delta}{(\omega_2-\omega_1)^2+\delta^2}\right)^2 \cos^2\theta \left(\cosh\phi_1 - \sinh\phi_1\right)^4 ,
\end{aligned}
\tag{B.121}
$$

$$
X_2 = \varepsilon_\infty - \frac{\mu_0}{\varepsilon_0} \left(\frac{16dflS^2\lambda g\mu_{\rm B}}{\hbar V}\right)^2 \frac{\sin^4\theta\cos^2\theta}{\delta^2} \left(\cosh\phi_2 - \sinh\phi_2\right)^4 ,
\tag{B.122}
$$

$$
\begin{aligned}
Y_1 &= \frac{(8dfl\lambda)^2 S^3}{\hbar V \varepsilon_0} \frac{\delta}{(\omega_2-\omega_1)^2+\delta^2} \cos^2\theta \left(\cosh\phi_1 - \sinh\phi_1\right)^2 \\
&\quad + \varepsilon_\infty \frac{\mu_0 g^2 \mu_{\rm B}^2 S}{\hbar V} \frac{\delta}{(\omega_2-\omega_1)^2+\delta^2} \left(\cosh\phi_1 - \sinh\phi_1\right)^2 \\
&\quad + 2\frac{\mu_0}{\varepsilon_0} \left(\frac{g\mu_{\rm B} 8dflS^2\lambda}{\hbar V}\right)^2 \cos^2\theta \frac{\delta(\omega_2-\omega_1)}{(\omega_2-\omega_1)^2+\delta^2} \left(\cosh\phi_1 - \sinh\phi_1\right)^4 ,
\end{aligned}
\tag{B.123}
$$

$$
\begin{aligned}
Y_2 &= \varepsilon_\infty \frac{(g\mu_{\rm B})^2 \mu_0 S}{\hbar V \delta} \sin^2\theta \left(\cosh\phi_2 - \sinh\phi_2\right)^2 \\
&\quad + \frac{S^3 (16dfl\lambda)^2}{\hbar V \varepsilon_0 \delta} \sin^2\theta\cos^2\theta \left(\cosh\phi_2 - \sinh\phi_2\right)^2 .
\end{aligned}
\tag{B.124}
$$

$\Delta\alpha/2\bar{\alpha}$ at ω_1 and ω_2 are plotted in Fig. B.4(b). These are quite small compared with the case of $\mathbf{H} \parallel [100], \mathbf{H}^\omega \perp [100]$.

List of Publications

Publications related to the current thesis:

- Y. Iguchi, S. Uemura, K. Ueno, and Y. Onose
  Nonreciprocal magnon propagation in a noncentrosymmetric ferromagnet $LiFe_5O_8$
  Phys. Rev. B **92**, 184419 (2015).
  This study is mainly mentioned in Chapter 3.

- Y. Iguchi, Y. Nii and Y. Onose
  Magnetoelectrical control of nonreciprocal microwave response in a multiferroic helimagnet
  Nat. Commun. **8**, 15252 (2017).
  I explained about this paper in Chapter 4.

- Y. Iguchi, Y. Nii, M. Kawano, H. Murakawa, N. Hanasaki, and Y. Onose
  Microwave non-reciprocity of magnon excitations in a non-centrosymmetric antiferromagnet $Ba_2MnGe_2O_7$
  Phys. Rev. B submitted.
  This work is mainly commented in Chapter 5.

Other publications:

- T. Nakajima, Y. Iguchi, H. Tamatsukuri, S. Mitsuda, Y. Yamasaki, H. Nakao, and N. Terada
  Uniaxial-Pressure Effects on Spin-Driven Lattice Distortions in Geometrically Frustrated Magnets $CuFe_{1-x}Ga_xO_2$ *(x=0, 0.035)*
  J. Phys. Soc. Jpn. **82**, 114711 (2013).

- Y. Kinoshita, N. Kida, M. Sotome, T. Miyamoto, Y. Iguchi, Y. Onose, and H. Okamoto

Terahertz Radiation by Subpicosecond Magnetization Modulation in the Ferrimagnet $LiFe_5O_8$
ACS photonics **3**, 1170-1175 (2016).

- R. Sasaki, Y. Nii, Y. Iguchi, and Y. Onose
Nonreciprocal propagation of surface acoustic wave in $Ni/LiNbO_3$
Phys. Rev. B **95**, 020407(R) (2017).

- Y. Nii, R. Sasaki, Y. Iguchi, and Y. Onose
Microwave Magneto-Chiral Effect in a Noncentro-symmetric Magnet CuB_2O_4
J. Phys. Soc. Jpn. **86**, 024707 (2017). [Editors' choice]

References

[1] T. Kimura, T. Goto, H. Shintani, K. Ishizaka, T. Arima and Y. Tokura, *Magnetic control of ferroelectric polarization*, Nature **426**, 55 (2003).

[2] D. Khomskii, *Classifying multiferroics: Mechanisms and effects*, Physics **2**, 20 (2009).

[3] T. H. O'DELL, *The Electrodynamics of Magneto-Electric Media* (Amsterdam: North-Holland, 1970).

[4] E. I. Rashba, *Properties of semiconductors with an extremum loop. 1. Cyclotron and combinational resonance in a magnetic field perpendicular to the plane of the loop*, Sov. Phys. Solid State **2** 1109 (1960).

[5] G. Dresselhaus, *Spin-orbit coupling effect in zinic blende structures*, Phys. Rev.**100**, 580 (1955).

[6] G. L. J. A. Rikken, J. Fölling, and P. Wyder, *Electricalmagnetochiral anisotropy*, Phys. Rev. Lett. **87**, 236602 (2001).

[7] G. L. J. A. Rikken and P. Wyder, *Magnetoelectric anisotropy in diffusive transport* Phys. Rev. Lett. **94**, 016601 (2005).

[8] X.-L. Qi and S.-C. Zhang, *Topological insulators and superconductors*, Rev. Mod. Phys. **83**, 1057-1110 (2011).

[9] J. D. Arago, *Mémoires de la classe des sciences mathématiques et physiques de l'Institut Impérial de France*, 1st part 93134 (1811).

[10] M. Faraday, *Experimental Researches in Electricity. -Ninteenth series*, Phil. Trans. R. Soc. Lond. **136**, 1-20 (1846).

[11] L. Pasteur, *Annales de chimie et de physique, 3rd series*, **28**, 5699 (1850).

[12] C. P. Wen, *Coplanar waveguide: A surface strip transmission line suitable for nonreciprocal gyromagnetic device applications*, IEEE Trans. Microwave Theory Tech. **MTT-17**, 1087-1090 (1969).

[13] E. B. Graham and R. E. Raab, *A theory for evaluating multipole moments induced by time derivative fields*, Molec. Phys. **52**, 185-194 (1984).

[14] G. Wagnière and A. Meire, *The influence of a static magnetic field on the absorption coefficient of a chiral molecule*, Chem. Phys. Lett. **93**, 78-81 (1982).

[15] G. Wagnière, *Magnetochiral dichroism in emission. Photoselection and the polarization of transitions*, Chem. Phys. Lett. **110**, 546-551 (1984).

[16] L. D. Barron and J. Vrbancich, *Magneto-chiral birefringence and dichroism*, Molec. Phys. **51**, 715-730 (1984).

[17] N. B. Baranova, Y. V. Bogdanov and B. Y. Zel'dovich, *New electro-optical and magneto-optical effects in liquids*, Sov. Phys. Usp. **20**, 870 (1977).

[18] G. L. J. A. Rikken and E. Raupach, *Observation of magneto-chiral dichroism*, Nature **390**, 493-494 (1997).

[19] G. L. J. A. Rikken, C. Strohm, and P. Wyder, *Observation of Magnetoelectric Directional Anisotropy*, Phys. Rev. Lett. **89**, 133005 (2002).

[20] M. Ceolín, S. G.-Ferrón, G.-Mascarós, and J. Ramón, *Strong Hard X-ray Magnetochiral Dichroism in Paramagnetic Enantiopure Molecules* Adv. Mater. **24**, 3120-3123 (2012).

[21] R. Sessoli, M.-E. Boulon, A. Caneschi, M. Mannini, L. Poggini, F. Wilhelm, and A. Rogalev, *Strong magneto-chiral dichroism in a paramagnetic molecular helix observed by hard X-rays*, Nat. Phys. **11**, 69-74 (2015).

[22] Y. Kitagawa, H. Segawa and K. Ishii, *Magneto-Chiral Dichroism of Organic Compounds*, Angew. Chem. **123**, 9299-9302 (2011).

[23] C. Train, R. Gheorghe, V. Krstic, L.-M. Chamoreau, N. S. Ovanesyan, G. L. J. A. Rikken, M. Gruselle, and M. Verdaguer, *Strong magneto-chiral dichroism in enantiopure chiral ferromagnets* Nat. Mater. **7**, 729-734 (2008).

[24] M. Saito, K. Ishikawa, K. Taniguchi, and T. Arima, *Magnetic Control of Crystal Chirality and the Existence of a Large Magneto-Optical Dichroism Effect in* CuB_2O_4, Phys. Rev. Lett. **101**, 117402 (2008).

[25] S. Bordács, I. Kézsmárki, D. Szaller, L. Demkó, N. Kida, H. Murakawa, Y. Onose, R. Shimano, T. Rõõm, U. Nagel, S. Miyahara, N. Furukawa, and Y. Tokura, *Chirality of matter shows up via spin excitations*, Nat. Phys. **8**, 734-738 (2012).

[26] I. Kézsmárki, D. Szaller, S. Bordács, V. Kocsis, Y. Tokunaga, Y. Taguchi, H. Murakawa, Y. Tokura, H. Engelkamp,T.Rõõm, and U. Nagel, *One-way transparency of four-coloured spin-wave excitations in multiferroic materials*, Nat. Commun. **5**, 3203 (2014).

[27] S. Kibayashi, Y. Takahashi, S. Seki, and Y. Tokura, *Magnetochiral dichroism resonant with electromagnons in a helimagnet*, Nat. Commun. **5** 4583 (2014).

[28] S. Tomita, K. Sawada, A. Porokhnyuk, and T. Ueda, *Direct Observation of Magnetochiral Effects through a Single Metamolecule in Microwave Regions*, Phys. Rev. Lett. **113**, 235501 (2014).

[29] Y. Okamura, F. Kagawa, S. Seki, M. Kubota, M. Kawasaki, and Y. Tokura, *Microwave Magnetochiral Dichroism in the Chiral-Lattice Magnet* Cu_2OSeO_3, Phys. Rev. Lett. **114**, 197202 (2015).

[30] Y. Nii, R. Sasaki, Y. Iguchi, and Y. Onose, *Microwave Magnetochiral Effect in the Non-centrosymmetric Magnet* CuB_2O_4, J. Phys. Soc. Jpn. **86**, 024707 (2017).

[31] M. Kubota, T. Arima, Y. Kaneko, J. P. He, X. Z. Yu, and Y. Tokura, *X-Ray Directional Dichroism of a Polar Ferrimagnet*, Phys. Rev. Lett. **92**, 137401 (2004).

[32] J.H. Jung, M. Matsubara, T. Arima, J. P. He, Y. Kaneko, and Y. Tokura, *Optical Magnetoelectric Effect in the Polar $GaFeO_3$ Ferrimagnet*, Phys. Rev. Lett. **93** 037403 (2004).

[33] M. Saito, K. Taniguchi and T. Arima, *Gigantic Optical Magnetoelectric Effect in CuB_2O_4*, J. Phys. Soc. Jpn. **77**, 013705 (2008).

[34] S. Toyoda, N. Abe, S. Kimura, Y. H. Matsuda, T. Nomura, A. Ikeda, S. Takeyama, and T. Arima, *One-Way Transparency of Light in Multiferroic CuB_2O_4*, Phys. Rev. Lett. **115**, 267207 (2015).

[35] N. Kida, H. Yamada, H. Sato, T. Arima, M. Kawasaki, H. Akoh, and Y. Tokura, *Optical Magnetoelectric Effect of Patterned Oxide Superlattices with Ferromagnetic Interfaces*, Phys. Rev. Lett. **99**, 197404 (2007).

[36] B. Pelle, H. Bitard, G. Bailly, and C. Robilliard, *Magnetoelectric Directional Nonreciprocity in Gas-Phase Molecular Nitrogen*, Phys. Rev. Lett. **106**, 1930030 (2011).

[37] I. Kézsmárki, N. Kida, H. Murakawa, S. Bordács, Y. Onose, and Y. Tokura, *Enhanced directional dichroism of terahertz light in resonance with magnetic excitations of the multiferroic $Ba_2CoGe_2O_7$ oxide compound*, Phys. Rev. Lett. **106**, 057403 (2011).

[38] I. Kézsmárki, U. Nagel, S. Bordács, R. S. Fishman, J. H. Lee, H. T. Yi, S.-W. Cheong, and T. Rõõm, *Optical Diode Effect at Spin-Wave Excitations of the Room-Temperature Multiferroic $BiFeO_3$*, Phys. Rev. Lett. **115**, 127203 (2015).

[39] Y. Takahashi, R. Shimano, Y. Kaneko, H. Murakawa, and Y. Tokura, *Magnetoelectric resonance with electromagnons in a perovskite helimagnet*, Nat. Phys. **8**, 121-125 (2011).

[40] Y. Takahashi, Y. Yamasaki and Y. Tokura, *Terahertz Magnetoelectric Resonance Enhanced by Mutual Coupling of Electromagnons*, Phys. Rev. Lett. **111**, 037204 (2013).

[41] Y. Takahashi, S. Kibayashi, Y. Kaneko, and Y. Tokura, *Versatile optical magnetoelectric effects by electromagnons in $MnWO_4$ with canted spin-spiral plane*, Phys. Rev. B **93**, 180404(R) (2016).

[42] Y. Okamura, F. Kagawa, M. Mochizuki, M. Kubota, S. Seki, S. Ishiwata, M. Kawasaki, Y. Onose, and Y. Tokura, *Microwave magnetoelectric effect via skyrmion resonance modes in a helimagnetic multiferroic*, Nat. Commun. **4**, 2391 (2013).

[43] A. Pimenov, A. A. Mukhin, V. Y. Ivanov, V. D. Travkin, A. M. Balbashov, and A. Loidl, *Possible evidence for electromagnons in multiferroic manganites*, Nat. Phys. **2**, 97-100 (2006).

[44] H. Katsura, A. V. Balatsky and N. Nagaosa, *Dynamical Magnetoelectric Coupling in Helical Magnets*, Phys. Rev. Lett. **98**, 027203 (2007).

[45] S. Miyahara and N. Furukawa, *Nonreciprocal Directional Dichroism and Toroidalmagnons in Helical Magnets*, J. Phys. Soc. Jpn. **81**, 023712 (2012).

[46] S. Miyahara and N. Furukawa, *Theory of magneto-optical effects in helical multiferroic materials via toroidal magnon excitation*, Phys. Rev. B **89**, 195145 (2014).

[47] T. Arima, *Ferroelectricity Induced by Proper-Screw Type Magnetic Order*, J. Phys. Soc. Jpn. **76**, 073702 (2007).

[48] S. Miyahara and N. Furukawa, *Theory of Magnetoelectric Resonance in Two-Dimensional S = 3/2 Antiferromagnet $Ba_2CoGe_2O_7$ via Spin-Dependent Metal-Ligand Hybridization Mechanism*, J. Phys. Soc. Jpn. **80**, 073708 (2011).

[49] H. Katsura, N. Nagaosa and A. V. Balatsky, *Spin Current and Magnetoelectric Effect in Noncollinear Magnets*, Phys. Rev. Lett. **95**, 057205 (2005).

[50] M. Mochizuki, *Microwave Magnetochiral Effect in Cu_2OSeO_3*, Phys. Rev. Lett. **114**, 197203(2015).

[51] L. Landau and E. Lifshitz, *On the theory of the dispersion of magnetic permeability in ferromagnetic bodies*, Phys. Zeitsch. der Sow. **8**, 153-169 (1935).

[52] T. L. Gilbert, *A Lagrangian formulation of the gyromagnetic equation of the magnetic field*, Phys. Rev. **100**, 1243 (1955).

[53] R. Damon and J. Eshbach, *Magnetostatic modes of a ferromagnet slab*, J. Phys. Chem. Solids. **19**, 308 (1961).

[54] R. Melcher, *Linear Contribution to Spatial Dispersion in the Spin-Wave Spectrum of Ferromagnets* Phys. Rev. Lett. **30**, 125 (1973).

[55] M. Kataoka, *Spin Waves in Systems with Long Period Helical Spin Density Waves Due to the Antisymmetric and Symmetric Exchange Interactions*, J. Phys. Soc. Jpn. **56**, 3635 (1987).

[56] I. Dzyaloshinsky, *A THERMODYNAMIC THEORY OF "WEAK" OF ANTIFERROMAGNETICS* J. Phys. Chem. Solids **4**, 241 (1958).

[57] T. Moriya, *Anisotropic superexchange interaction and weak ferromagnetism*, Phys. Rev. **249**, 1949 (1960).

[58] K. Zakeri, Y. Zhang, J. Prokop, T.-H. Chuang, N. Sakr, W. X. Tang, and J. Kirschner, *Asymmetric Spin-Wave Dispersion on Fe(110): Direct Evidence of the Dzyaloshinskii-Moriya Interaction* Phys. Rev. Lett. **104**, 137203 (2010).

[59] K. Zakeri, Y. Zhang, T.-H. Chuang, J. Kirschner, *Magnon Lifetimes on the Fe(110) Surface: The Role of Spin-Orbit Coupling* Phys. Rev. Lett. **108**, 197205 (2012).

[60] K. Di, V. L. Zhang, H. S. Lim, S. C. Ng, M. H. Kuok, J. Yu, J. Yoon, X. Qiu, and H. Yang, Hyunsoo, *Direct Observation of the Dzyaloshinskii-Moriya Interaction in a Pt/Co/Ni Film* Phys. Rev. Lett. **114**, 047201 (2015).

[61] H. T. Nembach, J. M. Shaw, M. Weiler, E. Jué, and T. J. Silva, *Linear relation between Heisenberg exchange and interfacial DzyaloshinskiiMoriya interaction in metal films* Nat. Phys. **11**, 825-829 (2015).

[62] A. A. Stashkevich, M. Belmeguenai, Y. Roussigné, S. M. Cherif, M. Kostylev, M. Gabor, D. Lacour, C. Tiusan, and M. Hehn, *Experimental study of spin-wave dispersion in Py/Pt film structures in the presence of an interface Dzyaloshinskii-Moriya interaction*, Phys. Rev. B **91**, 214409 (2015).

[63] X. Zhang, T. Liu, M. E. Flatté, and H. X. Tang, *Electric-Field Coupling to Spin Waves in a Centrosymmetric Ferrite*, Phys. Rev. Lett. **113**, 037202 (2014).

[64] V. Vlaminck and M. Bailleul, *Spin-wave transduction at the submicrometer scale: Experiment and modeling*, Phys. Rev. B **81**, 014425 (2010).

[65] Y. Iguchi, S. Uemura, K. Ueno, and Y. Onose, *Nonreciprocal magnon propagation in a noncentrosymmetric ferromagnet* $LiFe_5O_8$, Phys. Rev. B **92**, 184419 (2015).

[66] E. Beregi, E. Sterk, E. Pál, and M. Farkas-Jahnke, *Crystal defects in flux grown lithium ferrite,* $LiFe_5O_8$ *single crystals*, Acta Phys. Hung. **47**, 263 (1979).

[67] S. Ishiwata, Y. Taguchi, H. Murakawa, Y. Onose, and Y. Tokura, *Low-magnetic-field control of electric polarization vector in a helimagnet*, Science **319**, 1643 (2008).

[68] H. Murakawa, Y. Onose, S. Miyahara, N. Furukawa, and Y. Tokura, *Comprehensive study of the ferroelectricity induced by the spin-dependent d - p hybridization mechanism in* $Ba_2XGe_2O_7$ *(X = Mn, Co, and Cu)*, Phys. Rev. B **85**, 174106 (2012).

[69] P. B. Braun, *A Superstructure in Spinels*, Nature **170**, 1123 (1952).

[70] V. J. Folen, *Li ferrite*, Landolt-Börnstein Group III Condensed Matter **4b**, 325 (1970).

[71] Y. Ishikawa, K. Tajima, D. Bloch, and M. Roth, *Helical spin structure in manganese silicide MnSi*, Solid State Commun. **19**, 525 (1976).

[72] Y. Onose,Y. Okamura, S. Seki, S. Ishiwata, and Y. Tokura, *Observation of Magnetic Excitations of Skyrmion Crystal in a Helimagnetic Insulator* Cu_2OSeO_3, Phys. Rev. Lett. **109**, 037603 (2012).

[73] T. An, V. I. Vasyuchka, K. Uchida, A. V. Chumak, K. Yamaguchi, K. Harii, J. Ohe, M. B. Jungfleisch, Y. Kajiwara, H. Adachi, B. Hillebrands, S. Maekawa,

and E. Saitoh, *Unidirectional spin-wave heat conveyer*, Nat. Mater. **12**, 549 (2013).

[74] G. Dionne, *Magnetic-Anisotropy and Magnetostriction Constants of Substituted Lithium Ferrites at 300°K*, J. Appl. Phys. **40**, 4486 (1969).

[75] D. D. Stancil, *Theory of Magnetostatic Waves* (Springer, New York, 1993).

[76] G. Dionne, *Effect of external stress on remanence ratios and anisotropy fields of magnetic materials*, IEEE. Trans. Mag. **5**, 596 (1969).

[77] E. H. Turner, *Interaction of Phonons and Spin Waves in Yttrium Iron Garnet*, Phys. Rev. Lett. **5**, 100 (1960).

[78] D. Cortés-Ortuño and P. Landeros, *Influence of the Dzyaloshinskii-Moriya interaction on the spin-wave spectra of thin films*, J. Phys. Condens. Mat. **25**, 156001 (2013).

[79] S. Seki, Y. Okamura, K. Kondou, K. Shibata, M. Kubota, R. Takagi, F. Kagawa, M. Kawasaki, G. Tatara, Y. Otani, and Y. Tokura, *Magnetochiral nonreciprocity of volume spin wave propagation in chiral-lattice ferromagnets*, Phys. Rev. B **93**, 235131 (2016).

[80] R. Takagi, D. Morikawa, K. Karube, N. Kanazawa, K. Shibata, G. Tatara, Y. Tokunaga, T. Arima, Y. Taguchi, Y. Tokura, S. Seki, *Spin-wave spectroscopy of the Dzyaloshinskii-Moriya interaction in room-temperature chiral magnets hosting skyrmions*, Phys. Rev. B **95**, 220406(R) (2017).

[81] T. J. Sato, D. Okuyama, T. Hong, A. Kikkawa, Y. Taguchi, T. Arima, and Y. Tokura, *Magnon dispersion shift in the induced ferromagnetic phase of noncentrosymmetric MnSi*, Phys. Rev. B **94**, 144420 (2016).

[82] J. M. Lee, C. Jang, B.-C. Min, S.-W. Lee, K.-J. Lee, and J. Chang, *All-electrical measurement of interfacial Dzyaloshinskii-Moriya interaction using collective spin-wave dynamics*, Nano Lett. **16**, 62 (2015).

[83] O. Gladii, M. Haidar, Y. Henry, M. Kostylev, and M. Bailleul, *Frequency nonreciprocity of surface spin wave in permalloy thin films*, Phys. Rev. B **93**, 054430 (2016).

[84] Y.Iguchi, Y. Nii and Y. Onose, *Magnetoelectrical control of nonreciprocal microwave response in a multiferroic helimagnet*, Nat. Commun. **8**, 15252 (2017).

[85] T. Kimura, *Magnetoelectric Hexaferrites*, Annu. Rev. Condens. Matter Phys. **3**, 93-110 (2012).

[86] N. Momozawa, Y. Yamaguchi and M. Mita, *Magnetic structure change in* $Ba_2Mg_2Fe_{12}O_{22}$, J. Phys. Soc. Jpn **55**, 13501358 (1986).

[87] S. Ishiwata, D. Okuyama, K. Kakurai, M. Nishi, Y. Taguchi, and Y. Tokura, *Neutron diffraction studies on the multiferroic conical magnet* $Ba_2Mg_2Fe_{12}O_{22}$, Phys. Rev. B **81**, 174418 (2010).

[88] M. Kenzelmann, A. B. Harris, S. Jonas, C. Broholm, J. Schefer, S. B. Kim, C. L. Zhang, S.-W. Cheong, O. P. Vajk, and J.W. Lynn, *Magnetic inversion symmetry breaking and ferroelectricity in* $TbMnO_3$, Phys. Rev. Lett. **95**, 087206 (2005).

[89] J.-L. Jin, X.-Q. Zhang, G.-K. Li, and Z.-H. Cheng, *Giant anisotropy of magnetocaloric effect in* $TbMnO_3$ *single crystals*, Phys. Rev. B **83**, 184431 (2011).

[90] N. Momozawa, Y. Nagao, S. Utsumi, M. Abe, and Y. Yamaguchi, *Cation distribution and helimagnetic structure of the* $Ba_2(Zn_{1-x}Mg_x)_2Fe_{12}O_{22}$ *system as revealed by magnetization measurements and neutron diffraction*, J. Phys. Soc. Jpn **70**, 27242732 (2001).

[91] J. Smit, and H. P. J. Wijn, *Ferrites* (Philips Technical Library, 1959).

[92] S. Foner, *in MagnetismI* (eds Rado, G. T. and Suhl, H.) 383 (Academic Press, 1963).

[93] G. Srinivasan, *Magnetoelectric Composites*, Annu. Rev. Mater. Res. **40**, 153178 (2010).

[94] A. Zheludev, T. Sato, T. Masuda, K. Uchinokura, G. Shirane, and B. Roessli, *Spin waves and the origin of commensurate magnetism in* $Ba_2CoGe_2O_7$, Phys. Rev. B **68**, 024428 (2003).

[95] T. Masuda, S. Kitaoka, S. Takamizawa, N. Metoki, K. Kaneko, K. C. Rule, K. Kiefer, H. Manaka, and H. Nojiri, *Instability of magnons in two-dimensional antiferromagnets at high magnetic fields*, Phys. Rev. B **81**, 100402(R) (2010).

[96] K. Penc, J. Romhańyi, T. Rõõm, U. Nagel, Á. Antal, T. Fehér, A. Jánossy, H. Engelkamp, H. Murakawa, Y. Tokura, D. Szaller, S. Bordács, and I. Kézsmárki, *Spin-Stretching Modes in Anisotropic Magnets: Spin-Wave Excitations in the Multiferroic* $Ba_2CoGe_2O_7$, Phys. Rev. Lett. **108**, 257203 (2012).

[97] A. G. Gurevich and G. A. Melkov, *Magnetization Oscillations and Waves*, (CRC Press, 1996).

[98] F. Bloch, *Zur Theorie des Ferromagnetismus*, Zeitschrift für Phys. **61**, 206 (1930).

[99] M. Fallot, *Ferromagnetism of some alloys of iron*, Ann. Phys. **6**, 305 (1936).

[100] G. Heller and H. A. Kramers, *Classical model of ferromagneticum and its additional quantisation in the low temperature*, Proc. K. Akad. VAN Wet. TE AMSTERDAM **37**, 378 (1934).

[101] C. Herring and C. Kittel, *On the Theory of Spin waves in Ferromagnetic Media*, Phys. Rev. **81**, 869 (1951).

[102] T. Holstein and H. Primakoff, *Field dependence of the intrinsic domain magnetization of a ferromagnet*, Phys. Rev. **58**, 1098 (1940).

[103] C. Kittel, *On the theory of ferromagnetic resonance absorption*, Phys. Rev. **73**, 155 (1948).

[104] J. Barnas, *Dipolar waves in ferromagnetic systems with linear magnetoelectric properties*, J. Phys. C: Solid State Phys. **19**, 7035 (1986).

[105] C. Sandweg, Y. Kajiwara, A. V. Chumak, A. A. Serga, V. I. Vasyuchka, M. B. Jungfleisch, E. Saitoh, and B. Hillebrands, *Spin Pumping by Parametrically Excited Exchange Magnons*, Phys. Rev. Lett. **106**, 216601 (2011).

[106] Y. Nambu and G. Jona-Lasinio, *Dynamical Model of Elementary Particles Based on an Analogy with Superconductivity. I*, Phys. Rev. **122**, 345-358 (1961).

[107] J. Goldstone, *Field theories with ≪ Superconductor ≫ solutions*, IL Nuo. Cim. **19**, 154-164 (1961).

[108] J. Goldstone, A. Salam and S. Weinberg, *Broken Symmetries*, Phys. Rev. **127**, 965-970 (1962).

[109] D. Polder, *ON THE THEORY OF FERROMAGNETIC RESONANCE*, Philos. Mag. **40**, 99-115 (1949).

[110] J. H. E. Griffiths, *Anomalous high-frequency resistance of ferromagnetic metals*, Nature **158**, 670 (1946).

[111] L. Walker, *Magnetostatic Modes in Ferromagnetic Resonance*, Phys. Rev. **105**, 390 (1957).

[112] R. White and I. Solt, *Multiple Ferromagnetic Resonance in Ferrite Spheres*, Phys. Rev. **104**, 56 (1956).

[113] B. A. Kalinikos, *Excitation of propagating spin waves in ferromagnetic films*, IEE Proc. H-Microw. Opt. Antennas **127**, 4 (1980).

[114] R.R. Birss, *Symmetry and Magnetism*, in Selected Topics in Solid State Physics, edited by E.P. Wohlfarth (North- Holland, Amsterdam, 1966), Vol. III.

[115] E.B. Graham & R.E. Raab, *Magnetic effects in antiferromagnetic crystals in the electric quadrupole-magnetic dipole approximation*, Phil. Mag. B, **66**, 269-284(1992).

[116] J. Su, Y. Guo, J. Zhang, H. Sun, J. He, X. Lu, C. Lu, and J. Zhu, *Study on optical, dielectric, and magnetic properties of $Ba_2MnGe_2O_7$ ceramics*, Proceedings of ISAF-ECAPD-PFM 2012 (DOI:10.1109/ISAF.2012.6297818).